On the Morphology and Dynamics of Purple Membranes at the Solid-Liquid Junction

kumulative Dissertation

zur Erlangung des Doktorgrades der Naturwissenschaften

(Dr. rer. nat.)

dem

Fachbereich Chemie

der Philipps-Universität Marburg

vorgelegt von

Roelf-Peter Baumann

aus

Lübeck

Marburg an der Lahn, 2011

Abgabedatum: 03.08.2011
Erstgutachter: Prof. Dr. Norbert Hampp
Zweitgutachter: Prof. Dr. Gregor Witte

Wo rohe Kräfte sinnlos walten,
da kann sich kein Gebild gestalten.

FRIEDRICH VON SCHILLER (1759-1805),
Lied von der Glocke

Contents

1 Introduction

On one side there is the ongoing trend to reduce the dimensionality of materials in the context of nanotechnology, driven by the keen aspiration to gain access to novel and unique properties as well as advanced performance characteristics that emerge in the transition to the nanoworld. The key aspect of nanotechnology is, that upon a decrease in size to the nanoscale, certain properties of matter become size-dependent which results in materials that exhibit quantum effects and are qualitatively different from their bulk counterparts. Size-dependent properties include but are not limited to: optical and magnetic properties, capillary forces, melting points, conductivity, ionization potential and electron affinity, reactivity, surface and interfacial energy etc. On the other side is the thriving pursuit to understand biological processes and systems, living organisms and derivatives thereof, in order to utilize them for technological applications in the applied part of biology commonly referred to as biotechnology. At the interface resides nanobiotechnology, one, if not the main emerging field of research in science and engineering of this century. Merging the fields of nano- and biotechnology, nanobiotechnology deals with the investigation and utilization of the newly conceived nanobiomaterials, as well as the construction of novel functionalized nano-bio-hybrid-systems. Among many others, essential parts of nanobiotechnology employ solid-supported architectures such as membrane assemblies. Taking the multidisciplinary nature of nanobiotechnology into account, the study of such nanobiointerfaces is more than just a study of how nanomaterials interact with biological systems, but on an advanced level, it also elucidates the interfacial interactions between life sciences and nanoelectronics. By combining biomaterials like DNA, proteins, biomembranes or entire cells with electronic systems new exciting devices, sensors, and systems may be formed.[1–4] The nanobio interface characterized by its morphology and dynamics and governed by both extrinsic and intrinsic factors comprises the dynamic interactions between nanomaterial surfaces, such as carbon nanotubes, graphene, nanoparticles and biological components like DNA, proteins, biomembranes and even cells. This interplay at the solid-liquid junction between morphology and dynamics, both extrinsically and intrinsically influenced as illus-

trated based on figure 1.1 is to be studied by the paradigm of membrane proteins and biomembranes namely bacteriorhodopsin (BR) and purple membrane (PM).

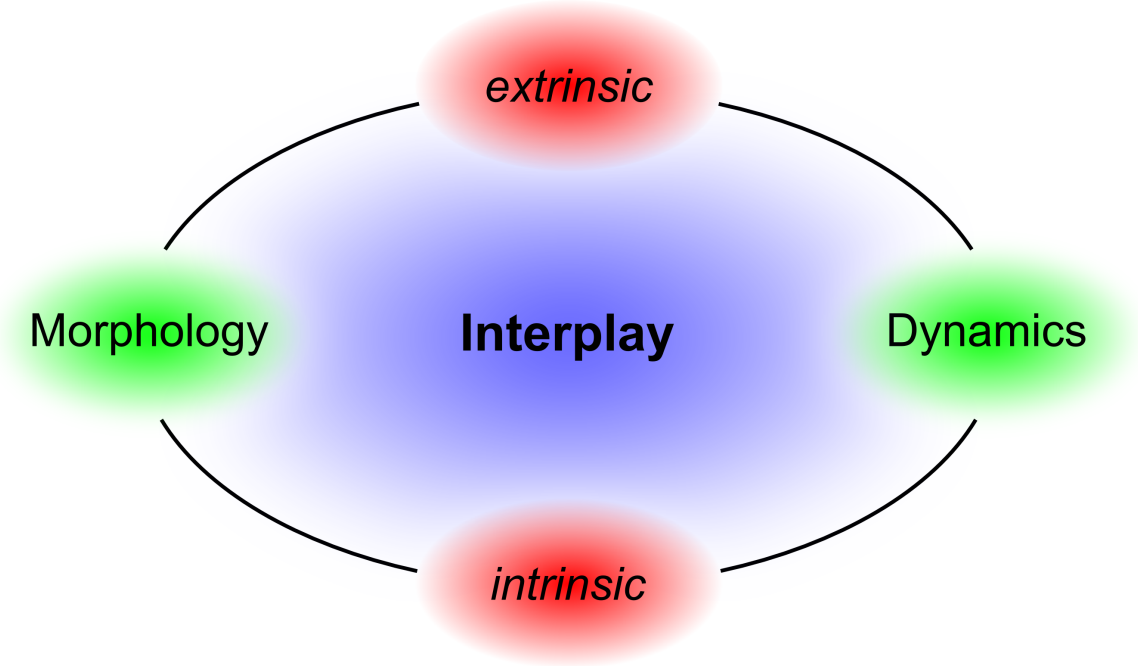

Figure 1.1: Interplay characterizing biomembrane systems at the solid-liquid junction

Key questions of this investigation are:

- Immobilization of membrane proteins on surfaces remains a challenge in nanobiotechnology because proper form and function is only retained in a near-native lipid environment. What does the nanobio interface in terms of morphology and dynamics of the extremely robust purple membrane under the extrinsic constraints of the solid-liquid junction look like?

- Beyond their importance for many physiological processes, dynamical transitions in biological membranes also bare implications for nanobiotechnology applications. Do solid-supported purple membranes exhibit such dynamics? What extrinsic and intrinsic factors constitute possible dynamic interactions and or changes?

- In their native host both sides of purple membranes are in touch with an aqueous environment. Embedded bacteriorhodopsins therein are thus able to perform large-scale conformational changes over the course of the photocycle with-

out restriction by a solid support. In contrast to the native cell a solid-support represents a breaking of symmetry in terms of bending and is thus expected to have a profound influence on purple membrane form and function. To what extend is transient or permanent bending of purple membrane influenced by the extrinsic constraints imposed by a solid-support and what implications arise from this confinement for technical applications? On a more fundamental level the question arises if membrane curvature is coupled intrinsically to bacteriorhodopsin or governed extrinsically by the geometric constraints of the *Halobacterium salinarum* cell or in this case the substrate surface?

2 Purple Membrane from *Halobacterium Salinarum*

Purple membrane from the halophilic organism *Halobacterium salinarum* featuring the light-driven proton pump bacteriorhodopsin and lipids only is expressed by the archaeon under anaerobic conditions to provide energy harvesting capabilities via photosynthesis.[5–8] Structurally, purple membrane belongs to the rare group of naturally occurring 2D crystalline membrane proteins featuring a very high protein to lipid mass ratio of 3 to 1 (molecule ratio 1 to 10). Within its native host the retinal protein BR, which not only shares deep homologies with other retinal proteins but also with G-protein coupled receptors (GPCRs), is arranged in trimers, which form the crystalline lattice of p3 symmetry within the lipid bilayer. BR itself is one of the few membrane proteins which have been analyzed both spectroscopically and structurally in their native environment and represents a prototype of seven transmembrane α-helical proteins. The helical domains which are interlinked by loop segments protruding out of the membrane surface on both sides enclose a pocket where the retinylidene chromophor is located. These loops are rather short and only in the B-C loop on the extracellular side an antiparallel β-sheet maintained by cation binding is found. To complete the molecular picture of the protein's secondary structure retinal is bound to lysine 216 via a Schiff-base linkage. Figure 2.1 presents a graphical summary.

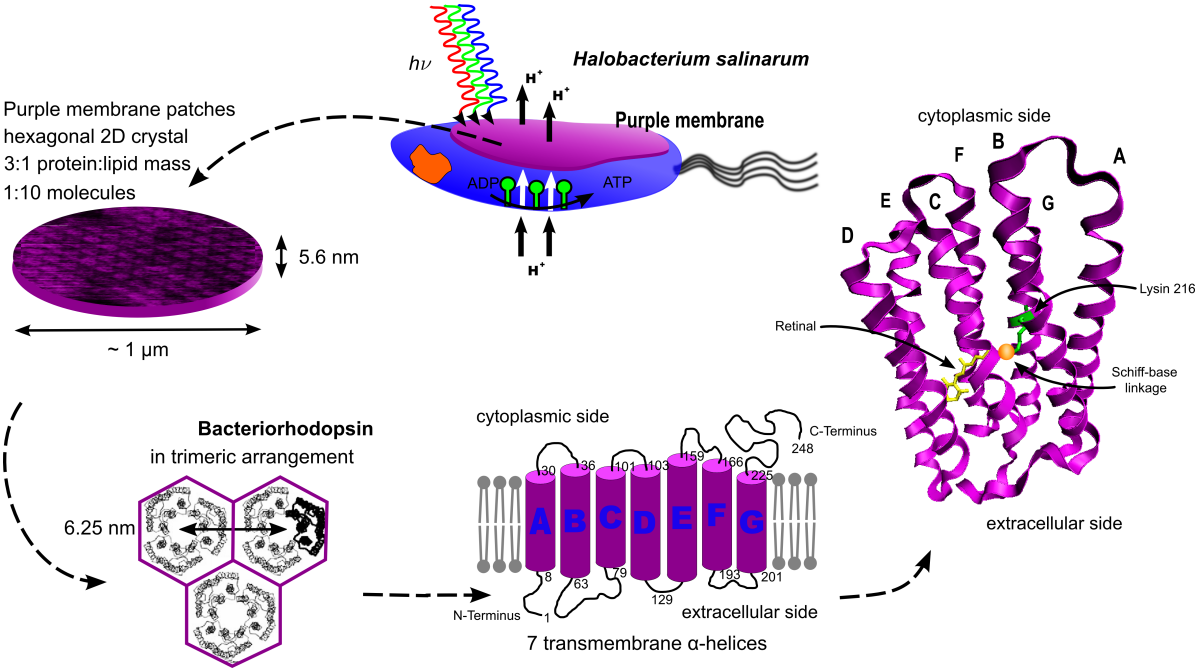

Figure 2.1: *Halobacterium salinarum* featuring Purple Membrane and Bacteriorhodopsin

Purple membrane patches feature unique properties as well as functional diversity and apart from possible technical applications[9] PMs provide an interesting model system to study the aforementioned interplay as they combine and unite both bulk and surface characteristics of membrane assemblies in one species. Within the crystal lattice of purple membrane, BR exhibits an extreme stability,[10,11] impervious to most chemical and physical influences, surpassing all other membrane assemblies thus far. The intactness of the distinctive hexagonal crystal lattice thus plays a unique role as simple indicator for the functional integrity of BR and PM in view of the interplay between morphology and dynamics by extrinsic and intrinsic factors. Due to its robustness a wide variety of extrinsic factors may be analyzed. Further, a vast library of variants and intrinsic point mutations provides a diverse platform with ample possibilities to study BR and PM behavior at the solid-liquid junction.

3 Atomic Force Microscopy

3.1 Introduction

Since its invention in 1986 by BINNIG *et al.*[12] atomic force microscopy (AFM) has played a crucial role in nano-scale science and technology.[13] Its great applicability especially in the fields of material and biosciences stems from its versatility, which is based on the vast number of contrastive material properties – mechanical, electromagnetic and chemical – that can be analyzed and imaged by AFM. AFM is a microscopic technique utilizing attractive and repulsive interaction forces at the atomic level to image samples *in-situ* with sub-nanometer resolution both lateral and vertical. For this a sharp nanostylus attached to the end of a flexible micro-cantilever is scanned across the sample surface in a rastering fashion. To ensure three-dimensional positioning with high accuracy, a piezoelectric scanner is used. Intermolecular forces govern the properties of gases, the behavior of colloidal solutions, crystal growth and biomolecular interactions. The cantilever probe functions as a force sensor and force actuator for these intermolecular interactions capable of spatially resolving them on the molecular level with piconewton (pN) sensitivity. Various methods which include tunneling current measurement,[12] optical deflection technique,[14] fiber interferometry[15] and piezoresistive methods[16] exist to measure resulting cantilever deflections at a resolution of a few angstroms, which are used to determine the surface contour or various other sample properties. A sensitive feedback mechanism is exploited to minimize forces applied to both sample and stylus.

Due to their amphiphilic nature and because they usually only develop their full activity in native environment the number of suitable methods for the biophysical characterization of membrane proteins and their assemblies is quite limited. The power of the AFM technique with respect to nanobiotechnology in general and this work in particular relies on the possibility to operate not just in air but in aqueous liquids or physiological buffers.[17] A wide variety of biological samples, ranging from single molecules such as nucleic acids and proteins to macromolecular assemblies

and whole cells may thus be analyzed statically and at work in their native environment with the AFM today.[18–28]
AFM is predestined for the observation of purple membrane and variants thereof on various substrates and under almost any desired conditions both in air and liquid to study its surface structure with sub-nanometer resolution.[29,30] This offers not only the possibility of side-differentiation and study of morphology but also of tracking dynamical changes of and within PM. AFM and its related techniques briefly explained in the following sections fully cover the scope of the investigation illustrated in figure 1.1.

3.2 Tapping Mode

Life is stressful, in a mechanical sense. Force plays a fundamental role in biological processes and its importance transcends into the nanobiotechnological world. Biomolecular forces lie between a few piconewtons as generated by myosins in eukaryotic motility processes and about 300 pN, the force required to unfold a protein molecule.[31–33] In order to prevent sample distortion deterioration or even destruction imaging forces between the nanostylus and the sample must not exceed similar magnitudes. In early contact mode AFM (CM-AFM) this was usually very difficult to ensure and only the most robust biological samples among them purple membrane could be investigated.[29] Only the introduction of a new vibrating mode, first in air by ZHONG *et al.*[34] in 1993, then in liquid with the so-called tapping mode (TM-AFM) a year later[35,36] allowed to observe a variety of macromolecules, that can not be imaged with CM-AFM. Sample damage is minimized in this vibrating mode, as contact time and lateral forces between the tip and sample are dramatically reduced. As the oscillating tip is scanned over the sample surface the amplitude and phase near its resonance frequency are monitored. Changes in either parameter arising from tip-sample interactions can be used to deduce sample topography or various other material properties. Appropriate adjustment of the driving frequency slightly above or below the resonance frequency of the cantilever allows one to specifically tune tip-sample interactions and thus measure from net attractive to net repulsive.[37] TM-AFM transformed the use of AFM in biology as it allows experiments to be performed not just under physiological conditions but even *in vivo* and on the most delicate samples such as lipid bilayers and entire cells.[38–40] To-date, high-resolution imaging of mammalian,[41] fungal[42–44] and bacterial[42,45] cells has been accomplished by the use of

tapping mode atomic force microscopy. First TM-AFM images of purple membrane were obtained in 1999 featuring similar resolution as CT-AFM.[46] Superior sensitivity combined with the high-resolution make TM-AFM ideally suited for the investigation of solid supported membrane assemblies, as it provides a tool to simultaneously study morphology and dynamics of biological membranes at the nanoscale.

3.3 Single Molecule Force Spectroscopy

Biological motion and the inhibition thereof, both essential for all life, are governed by forces arising from interactions on the molecular level. Single molecule force spectroscopy (SMFS)[47,48] allows for force and displacement generated by single molecules to be measured. From cells to proteins, a wide range of samples may be analyzed to gain insights into the machinery of life. AFM can be much more than just a microscope or an analyzing technique, it is also a nanotool capable of interacting with single molecules, measuring forces between them locally[49] or addressing and manipulating them with molecular precision.[31,50] SMFS is thus a direct derivative of AFM. Single-molecule experiments performed via the AFM directly measure individual molecular properties in contrast to averages obtained in bulk experiments. Consequently transient intermediates in biochemical processes can be captured and observed, which otherwise may only be accomplished by synchronizing the actions of large ensembles of molecules. Interestingly, a sufficiently long time-average or large number of observations from a single molecule is equivalent to a standard population-averaged snapshot of the molecular ensemble suggesting that a single-molecule experiment contains all information thereof. However contradicting this might seem, it is common in biological systems.
In SMFS force is measured as a function of displacement. In a so-called force cycle the nanostylus acting again as a force sensor or actuator is extended and retracted in the vertical direction at a given location on the sample, pushing down on and pulling back from the specimen of interest. As AFM is a rastering technique force cycles may be acquired during regular scanning in Force-Volume (FV) mode. Over the course of the force cycle, force is provided as cantilever deflection, while displacement is given by the separation between the AFM tip and the sample surface. Virtually any inter- as well as intramolecular interactions may be studied this way, keeping in mind that chemical modification[51] of tip and sample or the clamping[52] of the later between stylus and substrate via physisorption or covalent bonding might be necessary in

order to obtain the desired data. It is also noteworthy that SMFS usually operates under non-equilibrium conditions which implies that forces measured are a function of pulling velocity, that is speed and direction.[53] On the contrary this also means that SMFS may be used to study dynamics, such as bond dissociation dynamics.[54] SMFS has been utilized to gain insights into molecular interactions such as DNA-peptide or ligand-receptor binding,[49,55] enzyme catalysis, the physiological function of cell adhesion proteins,[56] structure and mechanics of membrane proteins, mapping of the dynamical energy landscape of proteins[57,58] and protein folding, protein structure-function relationship,[59] antigen-antibody interactions,[51] chemical bonds,[60] drug discovery, chirality[61] and many more.
Pulling a single BR molecule out of purple membrane results in a characteristic force-distance curve which reveals certain potential barriers within BR and consequently PM providing insight into both structure and mechanical stability. These may be analyzed by applying the worm-like-chain (WLC)[62] model to correlate them with the proteins amino acid sequence and secondary structural elements. Subjecting PMs to single molecule force spectroscopy thus allows for inter- and intramolecular interactions of BR and PM to be probed under various extrinsic and intrinsic influences to provide information on their respective morphology and dynamics, especially when coupled with the imaging capabilities of AFM.[63,64]

3.4 Electrostatic Force Microscopy

The high sensitivity and versatility of the AFM can be exploited in yet another way. In Electrostatic Force Microscopy (EFM) the imaging of surface dielectric properties is possible through the detection of electrostatic forces by the AFM tip. Initially designed for potentiometry and capacitance measurements in air[65] EFM soon evolved to probe a wide variety of nano-structures,[66–68,Publication E] surface charges in solution,[69] map charges in biological systems[70] such as DNA[71] and viruses[72] and even image the surface potential of active biomolecules.[73,74] EFM is a two-pass interleaved procedure, where sample topography is scanned via regular TM-AFM in the first pass, while the surface's potential is obtained in the second. Prior to the second pass of every scan-line, where the topography recorded in the first pass is retraced, the AFM tip is raised to a predefined lift-height. Wherever the potential of tip and surface differ, the cantilever experiences a net force, which is nullified to create a 3-dimensional potential image when plotted versus the in-plane coordinates. With

respect to purple membranes EFM may be used to differentiate between both sides of PM, that is the extracellular and the cytoplasmic, but also to discriminate between different variants of PM provided they feature a distinct surface charge such as the Arg7 variant.
Table 3.1 links the presented and used AFM techniques to distinct issues associated with the interplay to be studied.

	TM-AFM	SMFS	EFM
Topography (molecular resolution)	+(+[a])	–(–)	+(–)
Orientation	+[a]	+	+
Dynamics	+	+[b]	+

[a] flat membranes only
[b] on molecular level only

Table 3.1: Summary of measurement main purpose of atomic force microscopy techniques in the study of PM at the solid-liquid junction. A '+' denotes the technique is applicable, while a '–' denotes that it is not.

4 Cumulative Part Of Dissertation

Despite being quite indifferent in solution and thin films, BR and PM exhibit a delicate and interesting interplay of dynamical transitions and morphological changes at the solid-liquid junction upon extrinsic as well as intrinsic stimuli.

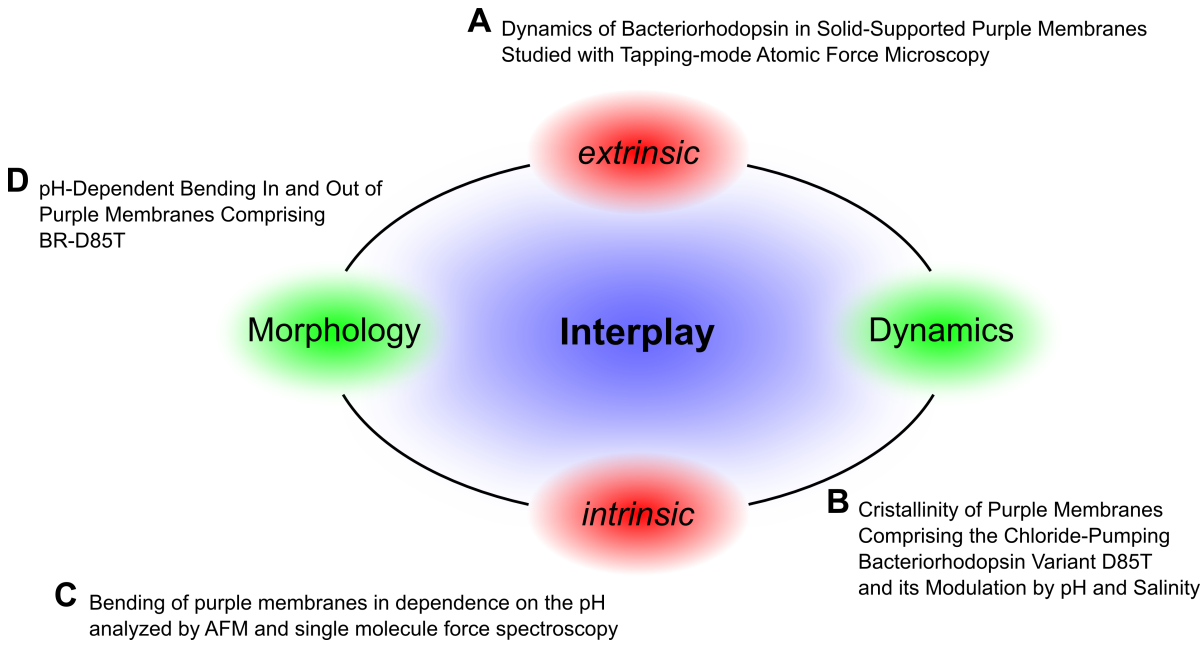

4.1 Dynamics of Bacteriorhodopsin [A]

When interfacing nanotechnology with biological systems in nanobiotechnology retention of function is generally desired. Form and function are closely related in that they are mutually dependent. Changes with respect to form or structure provide function and function necessitates structural dynamics. The immobilization of membrane proteins and membrane assemblies on solid surfaces within the context of nanobiotechnology remains a challenge. Interfacial destabilization is known for proteins as well as for lipid bilayers.[75,76] Proteins for example retain more structure on electrostatically neutral hydrophilic surfaces than on charged or hydrophobic surfaces but are still thought to denature at the solid-liquid as well as the vapor-liquid interface. Lipid bilayers may also undergo morphological changes at various interfaces. They tend to spread on surfaces with sufficiently high surface free energy or fall victim to delaminatation at the liquid-vapor junction. Delamination occurs because it is energetically unfavorable to remove the hydrophilic head groups from the solvation buffer. Consequently the membrane must reorganize to expose some of its lipid chains to the nascent air-water interface, while the rest of the lipids become part of newly formed vesicles in the receding aqueous solution. Proteins and lipid bilayers compared to PM however feature only weak internal interactions ranging from van-der-Waals forces to hydrogen bonding and are thus more susceptible to morphological and dynamical changes. Lipid bilayers and on the same token proteins may be stabilized by incorporating one into the other in order to overcome current membrane pitfalls by mimicking real cell membranes more closely. One of natures best paradigms being purple membrane which combines lipids and proteins in a 2D-crystalline matrix of tremendous stability.[10,11] Still, time-dependent TM-AFM analysis of solid-supported purple membranes reveals that redistribution processes take place between a crystalline core region, and a highly mobile rim region further characterized by a height of 5.2 nm and 4 nm respectively. Further, smaller patches in the mobile state change shape, move across the sample surface or fuse with other structures over time, underlining their mobility. These observations of dynamical transitions are astonishing as purple membrane is stabilized by some 6-7 kcal/mol association energy between a trimer and the surrounding hexagonal crystal lattice and should not undergo phase changes up to 70 °C at least in aqueous solution[77] making it an interesting and promising material for nanobiotechnology. Still even minute forces can have a profound impact on structure and stability if applied just right.[53] Substrate surface interactions must destabilize the crystal lattice and cause dynami-

cal changes of BR with morphological consequences for the entire PM. The interplay between the acting forces can be expressed by the following equations, which signify a stability criterion derived for purple membrane and its variants on an arbitrary substrate.

$$E_{PM} = E_{bR-bR} + E_{lipid-lipid} + E_{bR-lipid} \tag{4.1}$$

$$E_S = E_{bR-substrate} + E_{lipid-substrate} \tag{4.2}$$

As soon as the energy of PM-surface interactions exceeds the binding energy of the crystal lattice, that is $E_S > E_{PM}$, BR and lipids occupy the more mobile state. Drying of solid-supported purple membranes results in partial delamination along the outermost edge of the patches which features the mobile state. Between the unaltered crystalline core region and the delaminated edge a strongly fissured 4 nm domain prevails. Delamination and fissures indicate that the mobile state of PM is not stabilized by any kind of two-dimensional order or strong stabilizing interactions. This is further highlighted by the fact that no hexagonal crystal lattice is observed for the mobile state. Additionally, the local electric field above the membrane stepwise but continuously decreases according to EFM measurements from crystalline core towards delaminated rim owing to the different structure and composition of both PM states. Accompanied by these changes is of course a change in E_{PM}. Since E_{PM} apparently decreases with increasing distance from the core region of PM it may be further followed, that no crystalline domain can exist on any given substrate, once PM size falls below a substrate characteristic critical size. Figure 4.1, a series of time-dependent TM-AFM images, illustrates the disassembly of a small purple membrane fragment manually released from the larger PM with the AFM nanostylus. The two-dimensional crystal lattice is well-resolved for both large and small PM patches. Since the small patch was rotated slightly against the larger one upon detachment two lattices of different angular orientation contribute to the Fourier transform (Figure 4.1,b). While the displaced PM fragment starts to disassemble because of its unfavorable perimeter-to-area ratio and vanishes completely over the course of about 35 min, the large PM undergoes a rearrangement of unit cells ubiquitous along the edge of the crystalline region partially reincorporating BRs from the disassembling patch. This is a perfect example of a two-dimensional variant of the well-known Ostwald ripening.

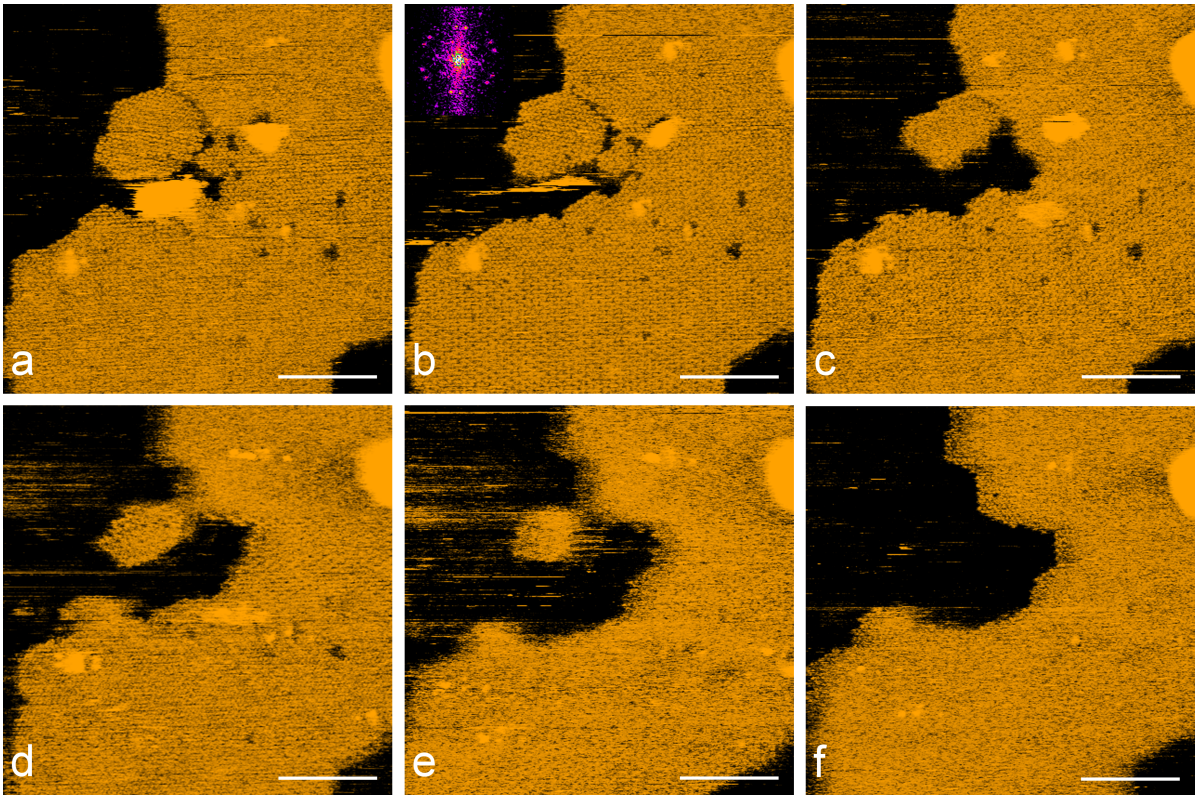

Figure 4.1: Time-dependent TM-AFM images showing morphological changes of purple membrane as a direct result of substrate induced BR dynamics. Image series shows PM redistribution processes at approximately 5 min time intervals. Scale bars are 100 nm.

The aforementioned dynamics that PM exhibits can be attributed to a reversible material exchange between both PM states and signify an equilibrium, which interestingly is dependent on the substrate PM is adsorbed to. On muscovite (mica) for example the more mobile state of PM is clearly favored over time. This of course has extensive implications not only because mica is a standard substrate for biomaterial immobilization in microscopy but also for nanobiotechnology and the interfacing of the physical and biological world in general as this usually takes place at a junction very similar to the one under investigation here. Especially if long-term stability is highly desired e.g. in thin-film devices utmost care must be taken when choosing a suitable substrate. Possible PM surface interactions E_S can be probed specifically by varying substrate properties such as hydrophobicity, charge, surface free energy and roughness in order to reveal key interactions and extrinsic factors to understand and eventually control the present intertwined interplay. Analyzing the dynamics of bacteriorhodopsin in solid-supported purple membranes on a plethora of substrates ranging from polypeptide or lipid coated mica over HOPG[1], to different metals in-

[1] **h**ighly **o**riented **p**yrolytic **g**raphite

cluding template stripped ones, all representing a broad range of surface free energies and varying ratio of dispersive and polar character, provided some clues but not yet exhaustive answers. Depending on the substrate the interplay of dynamical transitions and morphological changes of purple membrane is predominantly governed by either protein or lipid dynamics and interactions with the substrate, the result in either case however is virtually the same: dramatic morphological changes of PM. Only alleviating extrinsic stress discourages lipids from spreading and BR from changing conformation which in turn helps purple membrane morphology to prevail. Purple membrane shows the greatest stability, that is no dynamics even over prolonged periods of time (days), on substrates with a well-balanced set of possible interaction forces. In congruence with the proverb "less is more" minimizing interactions i.e. interfacing PM with less charged and less hydrophilic or hydrophobic substrates with less surface free energy such as gold for example, reduces or even prohibits dynamics. Maximizing E_S logically facilitates dynamics and thus morphological changes. Surface roughness, however, must also be considered as it has a known critical and profound influence on lipid mobility. Indeed on freshly oxidized Si-wafers, which are structurally and energetically similar to cleaved mica PM does not show any dynamics either. Freshly cleaved mica is atomically flat over micrometers by virtue of default providing a maximum of E_S. The Si-wafers display a much greater mean roughness ($R_{a,Si}$ = 0.295 nm vs. $R_{a,mica}$ = 0.021 nm) and since surface roughness governs the number of possible contact points between purple membrane and a substrate for van der Waals interactions etc. the respective E_S for Si-wafers is reduced.

Another noteworthy extrinsic factor is temperature. The rate constant of a reaction generally increases with temperature, hence it is not surprising that an increase in temperature significantly increases the speed of the redistribution process and the observed dynamics. Apart from this however there are further implications for morphology. The compactness of the protein-lipid packing within the crystalline lattice of purple membrane is dependent upon temperature. At about 60 °C mobility of the peptide groups of BR and their exposure to the external medium is at a maximum.[78] The exposure of buried BR residues involves molecular rearrangements within the membrane which leads to a more dynamic arrangement and a less densely packed crystal lattice concurrently increasing E_S and decreasing E_{PM}. Temperature in a sense acts like a catalyst. Also, the effects of temperature highlight the intricacy of the interplay between dynamics and morphology upon extrinsic influences and bridges over to intrinsic factors and the crystallinity of purple membranes in terms of the structural and conformational constitution of BR.

4.2 Crystallinity of Purple Membranes [B]

Self-assembly and structural stability of membrane proteins inside the cell membrane critically depends on specific protein-protein and protein-lipid interactions. BR conformational dynamics are expected to have a profound impact on these interactions and the morphology of purple membrane. Various molecular determinants of PM stability and crystalline assembly have been identified such as several key amino acid residues and retinal covalently bound to lysine 216.[7,79] Mutations in the core of BR may also affect lattice assembly.[80] These studies suggest, that PM morphology and dynamics at the solid-liquid junction are also influenced and possibly tunable by such intrinsic factors perhaps allowing for a reversal of the dynamical transitions described in the last section from a non-crystalline mobile back to a crystalline membrane assembly. Further, immanent factors of a more general nature that might be of interest and need to be considered are of course pH and ion concentration as they sometimes stabilize certain protein conformations. And indeed a single-point mutation in the core of BR results in purple membranes, which undergo structural changes from a non-crystalline state to a 2D-crystalline state, depending on the physicochemical conditions, that are pH and salinity. In the variant D85T the primary proton acceptor aspartic acid 85 is replaced by threonine, the equivalent residue in halorhodopsin, converting BR-D85T into a chloride pump.[81,82] Replacement of D85 not just by threonine but any neutral residue X also changes the pK_A values of virtually all amino acid residues responsible for proton translocation, which has considerable effect on the structural integrity of BR as it provides for greater structural flexibility, probably similar to BR-WT in the observed mobile state. Structural intermediates of the BR photocycle, that are formed in a light-dependent manner in the wild-type, are now accessible by tuning the pH of the PM-D85T suspension (see Table 4.1, page 19). Especially acidic conditions are of interest as they favor chloride binding within the membrane.[82] At pH values below six BR-D85T assumes an O-like structural intermediate which is characterized by an open extracellular half-channel. The opening is facilitated by helices A,B,D and E tilting outward from the center of the ion channel. This increased structural flexibility exhibited by BR-D85T is very likely to have a negative effect on the crystallization tendency since PM lattice assembly critically depends on proper interactions between specific residues.[7] However this structural flexibility also provides for the creation of an anion binding site at acidic pH with a high affinity for chloride ions in the immediate vicinity of the retinal binding pocket according to spectroscopy and transport measurements[82] as well as X-ray crystallo-

graphy.[83] Extrinsic and intrinsic influences on membrane morphology and dynamics are thus intertwined. Anion binding at this specific site is accompanied by helical rearrangements, which lead to closure of the extracellular channel, concurrently re-creating a wild-type-like configuration of BR-D85T within the purple membrane. The structural changes within PM-D85T are interrelated with spectroscopic changes, as PM-D85T has a purple appearance at pH < 6 in the presence of chloride.[82] An intrinsically forced reduction in structural flexibility or dynamics leading to structural stabilization of BR-D85T's tertiary structure thus recovers the ability of PM-D85T to from proper crystal contacts and subsequently restores a wild-type-like morphology by reformation of a hexagonal crystal lattice. This phenomenon is further indicative of the fact that purple membrane structure is apparently highly preserved in nature. To emphasize this point, a study of purple membrane variant PM-Tri (PM-D96G/F171C/F219L), which comprises permanently, not transiently wedge-shaped BRs shows that the lipid content of PM-Tri is specifically altered during membrane assembly to allow for a hexagonal crystalline PM-Tri lattice of flat topography[84] to be formed. The recrystallization process of PM-D85T was observed *in situ* for the first time by TM-AFM (Figure 4.2).

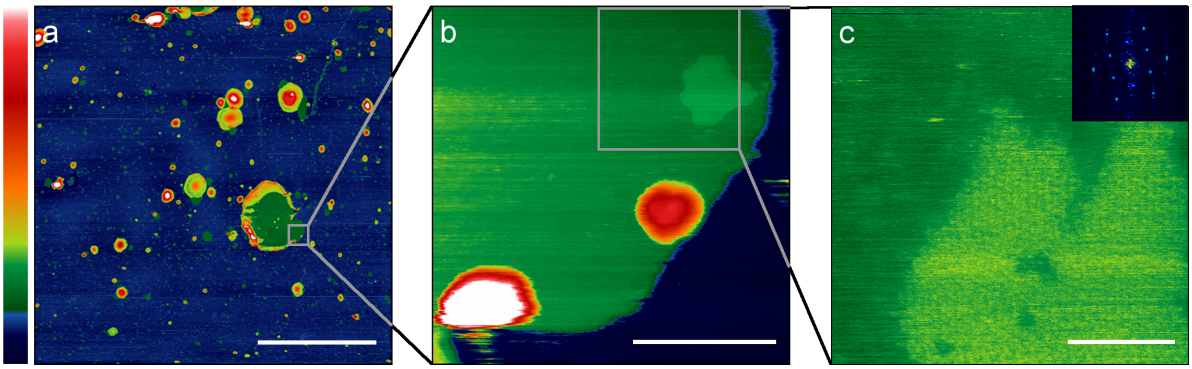

Figure 4.2: TM-AFM analysis of PM-D85T crystallization at pH = 3.4 in 300 mM KCl on a silicon wafer. Scale bars and color scales for a) through c) are 5 µm and 50 nm, 200 nm and 30 nm and 50 nm and 10 nm respectively.

Figure 4.2, a) shows several bent PM-D85T patches adsorbed to a silicon wafer under acidic and saline conditions. Taking a closer look (4.2, b)) reveals a small crystalline domain forming near the rim of a convexly bent membrane with a height of 5 nm compared to the non-crystalline surrounding area (4 nm) and a well resolved hexagonal crystal structure in the Fourier transform. Notably, the closely related halorhodopsin in contrast forms orthogonal crystal patches of $p42_12$ symmetry in the membrane of an overproducing *Halobacterium salinarum* strain.[85–87] The formation of crystalline domains within the purple membrane upon substrate binding nicely

ties in other recent topics in nanobiotechnology such as stimuli-dependent formation of membrane microdomains, which plays a major role in signal transduction.[88] Similar to PM-WT the detected crystalline domains exhibit certain structural dynamics and morph over time with respect to their shape and size (Figure 4.2, b), c)). Although generally increasing in size domains with an edge length larger than about 200 nm could hardly be detected. Apparently, the crystal lattice of PM-D85T forms less easily than the regular lattice of PM-WT and is therefore more prone to disruption by strong extrinsic sample-surface interactions, even on rough substrates like silicon, where E_S is reduced. This again is an example of the interplay between morphology and dynamics of BR and PM governed by extrinsic and intrinsic factors alike at the solid-liquid junction. Due to the geometric constraints of the cell, PM patches are all bent within *Halobacterium salinarum*. When freely suspended in solution and subsequently adsorbed to a solid-support however they prefer a rather flat topology. Notably, PM-D85T patches in Figure 4.2 are all bent either convex or concave revealing that intrinsic factors not only influence dynamics but may also affect morphology.

4.3 Bending of Purple Membranes [C,D]

The analysis of membrane curvature and its mechanical coupling to specialized membrane proteins that induce membrane bending due to their shape is a recent topic in cell biology. Cell organelles like endoplasmatic reticulum, the Golgi apparatus, caveoli, and inner mitochondria membranes for example exhibit a strongly bent membrane topography. In order to maintain membrane curvature particular proteins which provide a scaffold for membrane bending are deployed. But how is membrane bending perpetuated within commonly flat purple membranes at the solid-liquid junction? Bacteriorhodopsin provides for a light-driven, vectorial proton translocation (transfer) via a sequence of isomerization states on the part of retinal (isomerization) intertwined with a well-studied series of protonation changes of key amino acids within both half channels and the Schiff-base linkage alike.[89–91] These coincide with certain transient conformational changes within the structure of BR concomitantly switching the Schiff-base accessibility (switch) to either the cytoplasmic or extracellular half-channel.[6,90,92,93] Table 4.1 briefly summarizes this relationship to provide a concise overview of the so-called BR photocycle.

state	D96	SB	D85	PRC	CP	SB conformation	EC
B	+	+	−	+	Closed	all-*trans*	Closed[a]
J	+	+	−	+	Closed	13-*cis*-14-s-*cis*-15-*anti* twisted	Closed[a]
K	+	+	−	+	Closed	13-*cis*-14-s-*cis*-15-*anti* less twisted	Closed[a]
L	+	+	−	+	Closed	13-*cis*-14-s-*cis*-15-*anti*	Closed[a]
M_1	+	−	+	+	Closed	13-*cis*-14-s-*cis*-15-*anti*	Closed[a]
M_2	+	−	+	+	Open	13-*cis*-14-s-*trans*-15-*anti*	Closed[a]
N	−	+	+	−	Open	13-*cis*-14-s-*trans*-15-*anti*	Closed
O	+	+	+	−	Closed	all-*trans*	Open

[a] not explicitly referenced in literature

Table 4.1: Relationship between the protonation state of key amino acids in bacteriorhodopsin and associated shape changes of the molecule over the course of the photocycle. Moieties considered are aspartic acid 96 (D96), the Schiff-base linkage (SB), aspartic acid 85 (D85) and the proton release complex (PRC) from the cytoplasmic (CP) to the extracellular (EC) side. Protonation and deprotonation states are denoted by '+' and '-' respectively. SB accessibility from the CP or EC side is illustrated by the blue and green background color of the SB conformation column featuring the conformation of the retinylidene residue.

This isomerization/switch/transfer model provides a mean to describe the general concept of ion translocation by halobacterial retinal proteins.[89] Bacteriorhodopsin variant D85T is no exception, and quite the contrary very interesting in this regard, as it provides access to various structural intermediates of the BR photocycle simply by tuning the pH of the PM-D85T suspension. Consequently PM-D85T allows for intrinsic changes on the single BR level and their effect on morphology to be studied in thermal equilibrium. X-ray analysis shows large-scale conformational changes mainly attributed to helices F and G during the opening of the cytoplasmic and extracellular half channels in the M and O intermediates of the BR photocycle respectively,[90,94–96] which result in a geometrical anisotropy and transiently wedge-shaped BR molecules. Because of the strong coupling between BR trimers within the two-dimensional crystalline lattice of PM, a sufficient supernumerary count of wedge-shaped proteins as obtainable by titrating PM-D85T leads to a macroscopic bending in solution shown by cryo-SEM.[97] Such a microscopic mechanical change of membranes in response to shape changes of molecules embedded therein is a perfect example of how intrinsic factors may govern the morphology and dynamics of membrane assemblies. AFM, EFM and single molecule force spectroscopy were employed to gain insights into the bacteriorhodopsin photocycle represented by variant D85T at different pH values *in situ* at the solid-liquid junction in order to elucidate the re-

lationship between intrinsic changes of purple membrane on the BR level and the consequent effects on morphology. Depending on the pH, BR-D85X variants exist in an equilibrium of three spectroscopically distinguishable species.[98] A predominantly blue state at acidic pH, a preponderantly purple state at around neutral pH and a predominantly yellow state at higher pH values. These three states of accumulation in which BR-D85T may be trapped in are analogous to three distinct intermediates of the BR-WT photocycle, namely the O, N and M_2-intermediate, respectively.[96,98] Figure 4.3 shows the first AFM images of the aforementioned photocycle intermediates, including the first AFM images of strongly bent purple membranes.

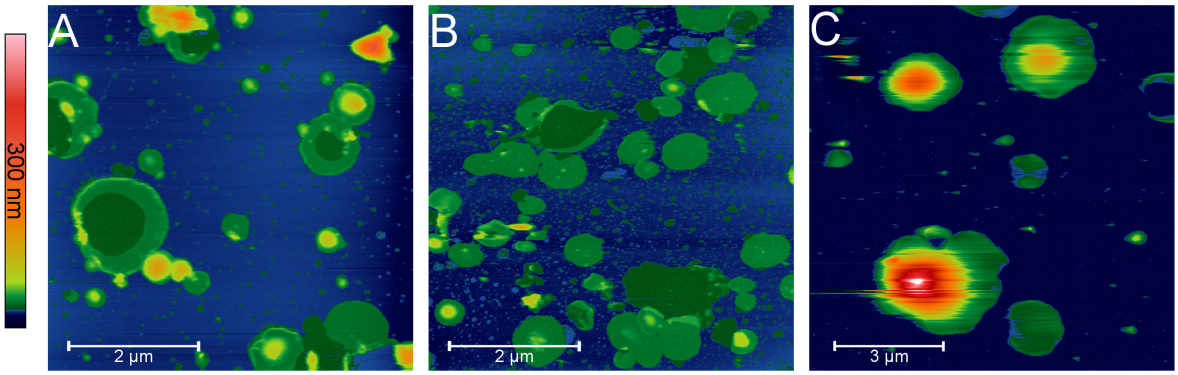

Figure 4.3: pH-dependent bending of PM-D85T observed on mica via TM-AFM in liquid under acidic, neutral and basic conditions (left to right). Due to the strong coupling between BR trimers an intrinsically changed morphology on the single BR level results in macroscopic bending of the entire PM under both acidic and basic conditions. In the N intermediate at neutral pH, where BR is not wedge-shaped, PMs assume a flat topography.

Purple membranes feature a cytoplasmic and an extracellular side, naturally two different ways of membrane adsorption to solid supports exist. One should result in convex, the other in concave structures. Interestingly only one strongly bent species was observed on the substrate surface in form of dome-like structures irrespective of acidic or alkaline conditions. Upon adsorption to a solid support a competing interplay between intrinsic and extrinsic effects for membrane morphology emerges. This interplay and the subsequent formation of collapsed and dome-like structures is illustrated based on Figure 4.4. If the bent membranes approach the substrate with their convex side attractive surface interactions arise, which antagonize the bending and pull the membrane from the point of first contact i.e. the middle outwards onto the substrate surface flattening it in the process. A small but elevated rim is all that remains of these collapsed PMs to hint at their bent nature. On the contrary, if PM-D85T are bent towards the surface not the middle but the rim approaches the surface first. Once again attractive interactions arise, but this time the water between PM

and the support is trapped preventing a further approach and collapse giving rise to dome-like structures featuring a flat rim area.

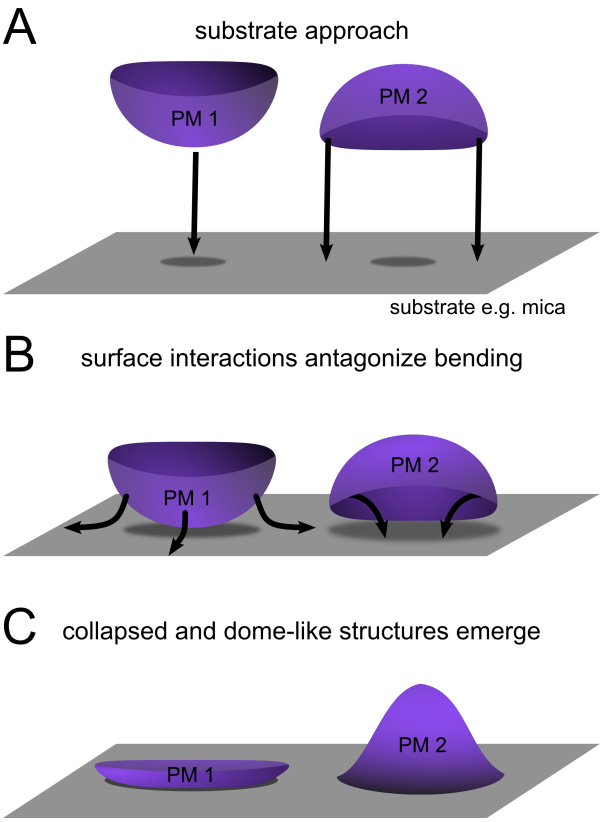

Figure 4.4: Schematic illustration of the formation of collapsed and dome-like purple membrane structures. A) Strongly bent PM-D85T in acidic and alkaline environment may approach the substrate surface either apex or rim first, that is with their convex (PM 1) or concave side respectively (PM 2). B) Surface interactions arising in both cases antagonize the bending and pull the membranes onto the substrate surface (arrows). C) Membranes of type PM 1 are pulled onto the substrate surface from the apex outward resulting in flat and collapsed structures, while in the case of PM 2 the rim flatly adsorbs to the substrate, but water trapped inside prevents further collapse giving rise to dome-like structures.

Dome-like PM structures are surrounded by buffer solution on both sides while arching over the substrate surface and are thus effectively 'freely suspended' resembling their truly native occurrence, the *Halobacterium salinarum* cell. Attempts to reach molecular resolution, a standard technique to reliably differentiate both sides of purple membrane[99] and possibly determine the direction of bending, were rendered futile due to highly-curved topology and even more so due to the great flexibility of the effectively free spanning membranes. Single molecule force spectroscopy at the apex of these structures, however, was successfully employed to experimentally discriminate between both sides of strongly bent purple membranes in both acidic and alkaline environment for the first time. According to these first force spectra obtained PM-D85T *in situ* is bent cytoplasmic side out at high pH values representing the M_2-intermediate, where an outward tilt of helix F is linked to the opening of the cytoplasmic half-channel. Under acidic conditions bending is reversed in the later O-intermediate of the BR-WT photocycle and PM-D85T is bent extracellular side out. The observed potential barriers combined with the knowledge of the tertiary structure of BR and consequent morphology of PM further illustrate the connection between mechanical stability and the characteristic features of a protein sequence as well as their implication on function in general.

Based on the distinct surface charge of each membrane side, electrostatic force microscopy also allows for side discrimination. While being more facile to perform and providing results more readily than SMFS, it must be kept in mind, that EFM is limited to the gaseous environment. Both purple membrane sides feature a negative but distinct surface charge, which differs by about 20 mV.[73] Contrary to the liquid environment, purple membranes in air posses a less negatively charged cytoplasmic side, while the extracellular side features a more negative electrostatic field distribution. EFM measurements successfully and concordantly complemented SMFS investigations. Interestingly EFM also revealed, that during the drying process purple membrane surface interactions are weakened and internal membrane tension responsible for the strong bending prevails. This holds for PMs incubated in both acidic and alkaline environment. In both cases small membrane patches of the flat and collapsed type partially detach from the surface and roll up inwards forming inverted dome-like structures during the drying process. These structures feature an elevated rim exhibiting a different surface charge than the still flatly adsorbed center, the difference being 20 mV. Concave membranes may thus feature both EC and CP side in EFM measurements owing to their strongly bent nature.

A superposition of surface tension induced by the shape of individual BR molecules and substrate interactions is responsible for the transformation of spherical PM patches in solution into dome-like structures upon substrate adsorption. Surface interaction forces scale dramatically with distance. Membrane topography at the apex of very large purple membranes should thus primarily be governed by the characteristic shape of individual BR molecules as the substrate surface and consequent interactions become irrelevant at this point. Smaller membranes on the contrary should be influenced more and more by substrate interactions down to a certain membrane size, below which membrane topography is primarily governed and strongly affected by the substrate. A detailed analysis of the curvature at the apex of bent purple membranes discloses not only this cut-off size for both acidic (1.73 µm) and alkaline (1 µm) conditions but also reveals a characteristic curvature, which is dependent on the physicochemical conditions of the environment PM-D85T is present in. Under alkaline conditions in the M_2-photocycle intermediate PM-D85T has a characteristic curvature of 1.17 μm^{-1}. In acidic media in the corresponding O-photocycle intermediate PM-D85T is bent in the opposite direction featuring a characteristic curvature of -0.25 μm^{-1}. This implies that conformational changes associated with the opening of the cytoplasmic half-channel in the M_2-state are more extensive than changes involved in the opening of the extracellular half-channel, providing further insights into the structure function relationship of the bacteriorhodopsin proton pump.

	acidic	neutral	alkaline
photocycle intermediate	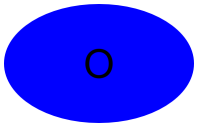	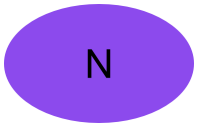	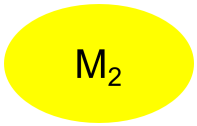
bR morphology	bent 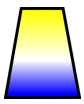	flat 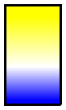	bent 
cytoplasmic side 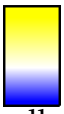 extracellular	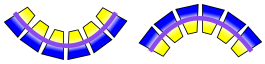	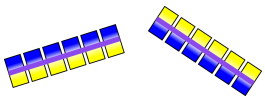	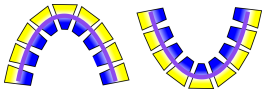
appearance on substrate	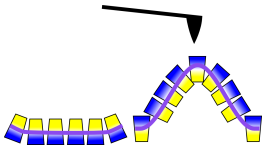		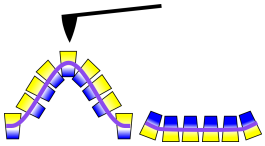
characteristic curvature	-0.25 µm^{-1}	–	1.17 µm^{-1}
cut-off-size	1.73 µm	–	1 µm

Table 4.2: Comparison and contrast of the O, N and M_2 photointermediate as represented by D85X according to TM-AFM and SMFS.

Table 4.2 briefly summarizes the results obtained from TM-AFM and single molecule force spectroscopy and compares and contrast the O, N and M intermediate as represented by D85X. Even more importantly though, because they lead to considerably different membrane curvature, the two distinct bending modes of the M_2 and the O state demonstrate that solely the intrinsic shape changes of the embedded proteins are responsible for the macroscopically bent nature of the membranes. Extrinsic effects play only a secondary role in this case. Small intrinsic influences or changes can have a profound influence on structure, form and also function of membrane assemblies at the solid-liquid junction. This must not be detrimental in nanobiotechnology as precise point-mutations might also be advantageously exploited in enhancing and fine-tuning structure and function.

5 Conclusion And Outlook

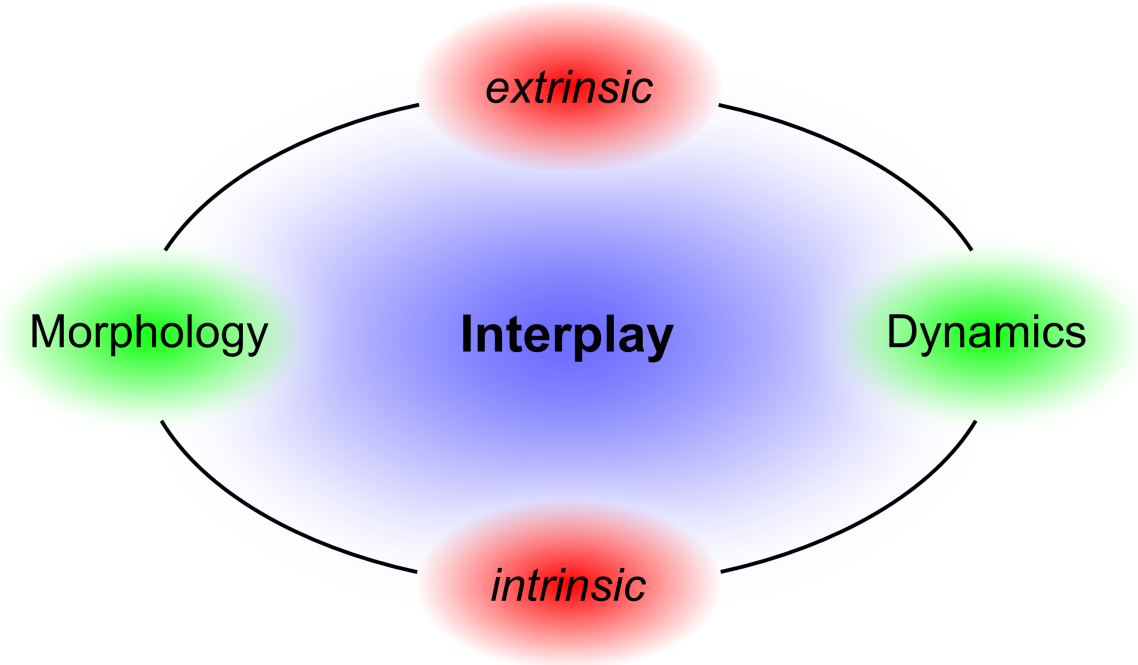

In dependence on the substrate bacteriorhodopsin within purple membrane at the solid-liquid junction is prone to dynamical transitions which were observed for the first time and found to be responsible for, in part, large scale morphological changes of the adsorbed purple membrane patches. Extrinsic and intrinsic factors could be identified to govern the interplay of morphology and dynamics, which lead to the deduction of a general, substrate independent stability criterion applicable to purple membranes comprising BR-wild-type and variants alike. Surface free energy and substrate roughness are key extrinsic parameters in this context that enable or slow down dynamical transitions within solid-supported PMs. Conversion of BR into a chloride pump by a single-point mutation seriously affects its crystallization tendency and reveals how intrinsic factors figure into the observed interplay. Interestingly, upon stabilization of the tertiary structure of BR-D85T, intrinsically mediated by chloride binding in the retinal binding pocket, the ability of PM-D85T to form coherent crystalline domains can be restored. PM-D85T also allowed for purple mem-

brane bending of various photocycle intermediates to be studied in thermal equilibrium at the solid-liquid junction. Side discrimination via SMFS and EFM showed that PM-D85T is bent cytoplasmic side out in the M_2 photointermediate and passes through a flat topology in the N intermediate in order to bend extracellular side out in the final O photointermediate. The different bending modes observed illustrate a reoccurring motif in nature of how the form of BR follows its function which is that of a vectorial proton pump transfering protons from the cytoplasmic to the extracellular medium. Membrane curvature was further analyzed to reveal that smaller membranes are strongly influenced by extrinsic constraints imposed by the substrate surface. Larger membranes on the contrary retain a characteristic curvature which is dependent on the physicochemical conditions and the corresponding shape of BR, thereby demonstrating that solely the intrinsic shape changes of the embedded proteins are responsible for the macroscopically bent nature of the membranes.
From a nanobiotechnology perspective, PM represents a supramolecular actuator set in motion by intrinsic and extrinsic influences, which opens a wide field of possible applications. One example would be as chemomechanical transducer, which upon a pH-shift changes shape and thereby interacts with its environment. These interaction capabilities place purple membrane in the context of other molecular machines and supramolecular switches. The observed and tentatively tunable dynamical transitions and the ability to reversibly control PM crystallinity might allow for the preparation of larger artificial membranes, which might be used for data storage or photovoltaic applications or serve as template in the construction of novel nanobiomaterials such as photonic crystals.

6 Zusammenfassung

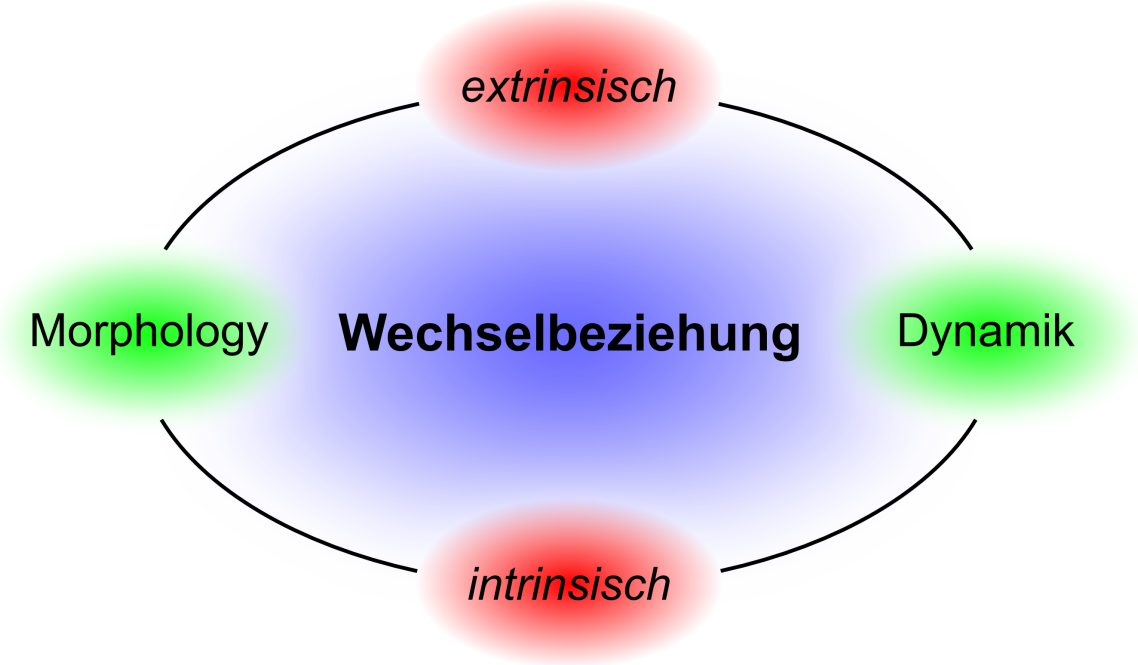

Im Rahmen dieser Arbeit konnte gezeigt werden, dass das an der fest-flüssig Grenzfläche adsorbierte und in der Purpurmembran eingebettete Bacteriorhodopsin in Abhängigkeit von der Substratoberfläche zu einer mehr oder weniger stark ausgeprägten Dynamik neigt. Dieser dynamische Wandel von BR wurde zum ersten Mal beobachtet, zeitaufgelöst untersucht und konnte schließlich für die teils gravierenden morphologischen Veränderungen der an der Oberfläche adsorbierten Purpurmembranen verantwortlich gemacht werden. Diverse extrinsische sowie intrinsische Faktoren, die die Wechselbeziehung aus Dynamik und Morphologie bestimmen, konnten identifiziert werden. Anhand dieser Erkenntnisse konnte ein allgemeines, vom Substrat unabhängiges Stabilitätskriterium abgeleitet werden, welches sowohl für BR-Wildtyp enthaltende als auch für die diversen Mutanten enthaltende Purpurmembranen Gültigkeit besitzt. Die freie Oberflächenenergie, sowie die Sustratrauheit stellen in diesem Zusammenhang extrinsische Schlüsselparameter dar, welche die Dynamik gar erst erlauben oder diese innerhalb der substratgebundenen Purpurmembranen

unterbinden. Eine gezielte Punktmutation (D85T) verwandelt BR nicht nur in eine Chloridpumpe, sondern beeinflußt ebenfalls dramatisch das Kristallisationsverhalten, was wiederum zeigt welchen Einfluß und was für eine Rolle intrinsische Faktoren im Rahmen der beobachteten Wechselbeziehung innehaben. Interessanterweise konnte gezeigt werden, dass eine Stabilisierung der tertiären Struktur von BR-D85T, die intrinsisch durch die Bindung von Chlorid innerhalb der Retinalbindungstasche vermittelt wurde, die Fähigkeit von PM-D85T zur Ausbildung eines zusammenhängenden Kristallgitters wiederherstellt. PM-D85T ermöglichte außerdem die Krümmung von Purpurmembranen in den unterschiedlichen Intermediaten des Photozyklus im thermischen Gleichgewicht an der fest-flüssig Grenzfläche zu untersuchen. Die Seitendifferenzierung via SMFS und EFM zeigte, dass PM-D85T im M_2-Photointermediat mit der zytoplasmatischen Seite nach außen gekrümmt ist. Im Gegensatz dazu ist sie, nachdem sie den durch eine flache Topographie gekennzeichneten N-Zustand durchlaufen hat, im finalen O-Photointermediat mit der extrazellulären Seite nach außen gekrümmt. Die unterschiedlichen beobachteten Krümmungsmodi verdeutlichen ein sich in der Natur wiederhohlendes Konzept der Kopplung von Form und Funktion, indem die Konformation von BR mit der Funktion als vektorieller Protonenpumpe zum Transport von Protonen von der zytoplasmatischen zur extrazellulären Seite eng verknüpft ist. Eine genauere Untersuchung der Krümmung ergab, dass kleinere Membranen sehr stark von den extrinsischen Einschränkungen, hervorgerufen durch die Wechselwirkung mit der Substratoberfläche, beeinflußt werden. Größere Membranen hingegen bewahren eine charakteristische Krümmung, die von den physikochemischen Bedingungen und der damit Verknüpften Form von BR abhängen. Dies zeigt, dass einzig und allein die intrinsischen Formänderungen des eingebetteten Proteins für die makroskopisch gekrümmte Natur der Membranen verantwortlich ist.

Von einem nanobiotechnologischen Standpunkt aus betrachtet stellen Purpurmembranen einen supramolekularen Aktuator dar, der von sowohl intrinsischen, als auch extrinsischen Einflüssen verändert und in Gang gebracht werden kann. Diese Tatsache eröffnet ein weites Feld für mögliche Anwendungen, z.B. als chemomechanischer Wandler, der pH-Wert bedingt seine Form verändert und auf diese Weise mit seiner direkten Umgebung interagieren kann. Diese Interaktionsmöglichkeit rückt die Purpurmembranen in den Kontext anderer molekularer Maschinen und supramolekularer Schalter. Die beobachteten und tendenziel steuerbaren dynamischen Eigenschaften von BR und PM an der fest-flüssig Grenzfläche kombiniert mit der reversiblen Kontrolle über das PM Kristallisationsverhalten könnten die Erzeugung von großflächigen, künstlichen Membranen ermöglichen. Diese sind von großem

Interesse für die optische Datenspeicherung, Anwendungen im Bereich der Photovoltaik oder als Templat für die Darstellung neuartiger Nanobiomaterialien wie Photonischekristalle.

7 Acknowledgements

I would like to extend a special thank-you to my parents and siblings who inexhaustibly support me on all my steps of life.

This dissertation could not have been written without Prof. Dr. Norbert Hampp who not only served as my supervisor but also supported, encouraged and challenged me throughout my academic program never accepting less than my best efforts. I thank him for giving me the opportunity to work in his research group and draw up my dissertation in the interesting field of nanobiotechnology. The interdiciplinary topic combined with the diversity of scientific questions allowed me to broaden my intellectual horizon and extend my fundamental knowledge in chemistry, physics and associated fields of nanobiotechnology. In the course of my doctoral thesis I was also able to take part in the International PhD School of Nanobiotechnology for which I am grateful for.

I thank Prof. Dr. Gregor Witte for the assumption of the second opinion.

My extraordinary colleagues, in particular those from room 2401, their support and the serious, fruitful, interesting, buoyant, and not exclusively academic discussions and distractions all will be missed. I thank them all. In particular Nina Schromczyk shall be thanked for the never ending supply of BR and its variants.

My deepest and sincere thanks go to my girlfriend for all her love, patience and simply being there when I needed her most.

---

8 Bibliography

1. Astier, Y.; Bayley, H.; Howorka, S. *Curr. Opin. Chem. Biol.* **2005**, *9*, 576–584.
2. Fromherz, P. *Annals of the New York Academy of Sciences* **2006**, *1093*, 143.
3. Willner, I.; Basnar, B.; Willner, B. *FEBS Journal* **2007**, *274*, 302–309.
4. Willner, I.; Shlyahovsky, B.; Zayats, M.; Willner, B. *Chem. Soc. Rev.* **2008**, *37*, 1153–1165.
5. Oesterhelt, D.; Stoeckenius, W. *Nat. New Biol.* **1971**, *233*, 149.
6. Haupts, U.; Tittor, J.; Oesterhelt, D. *Annu. Rev. Biophys. Biomol. Struct.* **1999**, *28*, 367.
7. Krebs, M. P.; Isenbarger, T. A. *Biochimica et Biophysica Acta* **2000**, *1460*, 15.
8. Renner, C.; Kessler, B.; Oesterhelt, D. *Journal of Lipid Research* **2005**, *46*, 1755.
9. Hampp, N. *Chem. Rev.* **2000**, *100*, 1755.
10. Brouillette, C. G.; Muccio, D. D.; Finney, T. K. *Biochemistry* **1987**, *26*, 7431.
11. Shen, Y.; Safinya, C. R.; Liang, K. S.; Ruppert, A. F.; Rothschild, K. J. *Nature* **1993**, *366*, 48.
12. Binnig, G.; Quate, C. F.; Gerber, C. *Phys. Rev. Lett.* **1986**, *56*, 930.
13. Müller, D. J.; Dufrêne, Y. F. *Nature Nanotechnology* **2008**, *3*, 261–269.
14. Meyer, G.; Amer, N. M. *Appl. Phys. Lett.* **1990**, *57*, 2089–2091.
15. Rugar, D.; Mamin, H. J.; Guethner, P. *Appl. Phys. Lett.* **1989**, *55*, 2588.
16. Tortonese, M.; Barrett, R. C.; Quate, C. F. *Appl. Phys. Lett.* **1993**, *62*, 834–836.
17. Marti, O.; Drake, B.; Hansma, P. *Appl. Phys. Lett.* **1987**, *51*, 484.
18. Drake, B.; Prater, C. B.; Weisenhorn, A. L.; Gould, S. A.; Albrecht, T. R.; Quate, C. F.; Cannell, D. S.; Hansma, H. G.; Hansma, P. K. *Science* **1989**, *243*, 1586–1589.
19. Radmacher, M.; Tillmann, R.; Fritz, M.; Gaub, H. *Science* **1992**, *257*, 1900–1905.
20. Engel, A.; Gaub, H. E.; Mueller, D. J. *Curr. Biol.* **1999**, *9*, R133.
21. Clausen-Schaumann, H.; Seitz, M.; Krautbauer, R.; Gaub, H. *Curr. Opin. Chem.*

Biol. **2000**, *4*, 524–530.
22. Fisher, T.; Carrion-Vazquez, M.; Oberhauser, A.; Li, H.; Marszalek, P.; Fernandez, J. *Neuron* **2000**, *27*, 435–446.
23. Hinterdorfer, P.; Dufrêne, Y. F. *Nat. Methods* **2006**, *3*, 347.
24. Kienberger, F.; Ebner, A.; Gruber, H.; Hinterdorfer, P. *Acc. Chem. Res.* **2006**, *39*, 29.
25. Li, G.; Xi, N.; Wang, D. *J. Cell. Biochem.* **2006**, *97*, 1191.
26. Oesterhelt, F.; Scheuring, S. *Curr. Nanosci.* **2006**, *2*, 329.
27. Sewald, N.; Wilking, S.; Eckel, R.; Albu, S.; Wollschlager, K.; Gaus, K.; Becker, A.; Bartels, F.; Ros, R.; Anselmetti, D. *J. Pept. Sci.* **2006**, *12*, 836.
28. Simon, A.; Durrieu, M. *Micron* **2006**, *37*, 1.
29. Butt, H.-J.; Downing, K. H.; Hansma, P. K. *Biophysical Journal* **1990**, *58*, 1473–1480.
30. Müller, D. J.; Schabert, F. A.; Büldt, G.; Engel, A. *Biophysical Journal* **1995**, *68*, 1681.
31. Rief, M.; Gauntel, M.; Oesterhelt, F.; Fernandez, J.; Gaub, H. *Science* **1997**, *276*, 1109.
32. Fisher, T.; Oberhauser, A.; Carrion-Vazquez, M.; Marszalek, P.; Fernandez, J. *Trends Biochem. Sci.* **1999**, *24*, 379.
33. Oesterhelt, F. *Science* **2000**, *288*, 143.
34. Zhong, Q.; Inniss, D.; Kjoller, K.; Elings, V. *Surf. Sci. Lett.* **1993**, *290*, L688.
35. Hansma, P.; Cleveland, J. P.; Radmacher, M.; Walters, D. A.; Hilner, P. E.; Bezanilla, M.; Prater, C. B.; Massie, J.; Fukugona, L.; Gurley, J.; Elings, V. *Appl. Phys. Lett.* **1994**, *64*, 1738.
36. Putman, C. A. J.; d. Wetf, K. V.; Grooth, B. G. D.; Hulst, N. F. V.; Greve, J. *Appl. Phys. Lett.* **1994**, *64*, year.
37. Stark, R. W.; Schitter, G.; Stemmer, A. *Phys. Rev. B* **2003**, *8*, 085401.
38. Shao, Z.; Yang, J.; Somlyo, A. P. *Annu. Rev. Cell. Dev. Biol.* **1995**, *11*, 241.
39. Poggi, M. A.; Gadsby, E. D.; Bottomley, L. A.; King, W. P.; Oroudjev, E.; Hansma, H. *Anal. Chem.* **2004**, *76*, 3429.
40. Kirat, K. E.; Morandat, S.; Dufrêne, Y. F. *Biochimica et Biophysica Acta* **2010**, *1798*, 750–765.
41. Kumar, S.; Hohn, J. H. *Traffic* **2001**, *2*, 746.
42. Dufrêne, Y. F. *J. Bacteriol.* **2002**, *184*, 5205.
43. Touhami, A.; Jericho, M. H.; Beveridge, T. J. *J. Bacteriol.* **2004**, *186*, 3286.
44. Pelling, A. E.; Sehati, S.; Gralla, E. B.; Valentine, J. S.; Gimzewski, J. K. *Science* **2004**, *3005*, 1147.
45. Pelling, A. E.; Li, Y.; Shi, W.; Gimzewski, J. K. *Proc. Nat. Acad. Sci. USA* **2005**, *102*, 6484.
46. Möller, C.; Allen, M.; Elings, V.; Engel, A.; Müller, D. J. *Biophysical Journal* **1999**,

77, 1150.
47. Greenleaf, W. J.; Woodside, M. T.; Block, S. M. *Annu. Rev. Biophys. Biomol. Struct.* **2007**, *36*, 171–190.
48. Janshoff, A.; Neitzert, M.; Oberdörfer, Y.; Fuchs, H. *Angew. Chem.* **2000**, *112*, 3346.
49. Florin, E.-L.; Moy, V. T.; Gaub, H. E. *Science* **1994**, *264*, 415.
50. Rief, M.; Oesterhelt, F.; Heymann, B.; Gaub, H. *Science* **1997**, *275*, 1295.
51. Lee, G. U.; Kidwell, D. A.; Colton, R. J. *Langmuir* **1994**, *10*, 354.
52. Oberhauser, A. F.; Hansma, P. K.; Carrion-Vazquez, M.; Fernandez, J. M. *Proc. Nat. Acad. Sci. USA* **2001**, *98*, 468–472.
53. Carrion-Vazquez, M.; Li, H.; Marszalek, P. E.; Oberhauser, A. F.; Fernandez, J. M. *Nat. Struct. Biol.* **2003**, *10*, 738–741.
54. Evans, E. *Annu. Rev. Biophys. Biomol. Struct.* **2001**, *30*, 105–128.
55. Junker, J. P.; Ziegler, F.; Rief, M. *Science* **2009**, *323*, 633–637.
56. Evans, E. A.; Calderwood, D. A. *Science* **2007**, *316*, 1148–1153.
57. Barsegov, V.; Klimov, D. K.; Thirumalai, D. *Los Alamos National Laboratory, Preprint Archive, Condensed Matter* **2006**, *1-32*, 0601324.
58. Sapra, K. T.; Balasubramanian, G. P.; Labudde, D.; Bowie, J. U.; Müller, D. J. *J. Mol. Biol.* **2008**.
59. Li, H.; Linke, W. A.; Oberhauser, A. F.; Carrion-Vazquez, M.; Kerkvliet, J. G.; Lu, H.; Marszalek, P. E.; Fernandez, J. M. *Nature* **2002**, *418*, 998–1002.
60. Grandbois, M.; Beyer, M.; Rief, M.; Clausen-Schaumann, H.; Gaub, H. E. *Science* **1999**, *283*, 1727–1730.
61. McKendry, R.; Theoclitou, M. E.; Rayment, T.; Abell, C. *Nature* **1998**, *391*, 566.
62. Bustamante, C.; Marko, J. F.; Siggia, E. D.; Smith, S. *Science* **1994**, *265*, 1599.
63. Müller, D. J.; Heymann, J. B.; Oesterhelt, F.; Möller, C.; Gaub, H.; Büldt, G.; Engel, A. *Biochimica et Biophysica Acta* **2000**, *1460*, 27.
64. Kessler, M.; Glaub, E. H. *Structure* **2006**, *14*, 521.
65. Martin, Y.; Abraham, D. W.; Wickramasinghe, H. K. *Appl. Phys. Lett.* **1988**, *52*, 1103.
66. Zdrojek, M.; Melin, T.; Diesinger, H.; Stievenard, D.; Gebicki, W.; Adamowicz, L. *Journal of Applied Physics* **2006**, *100*, 114326.
67. Qiu, X.; Qi, G.; Yang, Y.; Wang, C. *Journal of Solid State Chemistry* **2008**, *181*, 1670.
68. Yamamoto, S.-I.; Kobayashi, K.; Yamada, H.; Yoshioka, H.; Uraoka, Y.; Fuyuki, T.; Okuda, M.; Yamashita, I. *Journal of Scanning Probe Microscopy* **2008**, *3*, 13.
69. Xu, S.; Arnsdorf, M. F. *PNAS* **1995**, *92*, 10384.
70. Johnson, A. S.; Nehl, C. L.; Mason, M. G.; Hafner, J. H. *Langmuir* **2003**, *19*, 10007.
71. Mikamo-Satoh, E.; Yamada, F.; Takagi, A.; Matsumoto, T.; Kawai, T. *Nanotechnol-*

ogy **2009**, *20*, 145102.
72. MacCuspie, R. I.; Nuraje, N.; Lee, S.-Y.; Runge, A.; Matsui, H. *JACS* **2008**, *130*, 887.
73. Knapp, H. F.; Mesquida, P.; Stemmer, A. *Surface and Interface Analysis* **2002**, *33*, 108.
74. Oh, Y. J.; Jo, W.; Yang, Y.; Park, S. *Appl. Phys. Lett.* **2007**, *90*, 143901/1–143901/3.
75. Cremer, P. S.; Boxer, S. G. *J. Phys. Chem. B* **1999**, *103*, 2554.
76. Coen, M. C.; Lehmann, R.; Gröning, P.; Bielmann, M.; Galli, C.; Schlapbach, L. *Journal of Colloid and Interface Science* **2001**, *233*, 180.
77. Jackson, M. B.; Sturtevant, J. M. *Biochemistry* **1978**, *17*, 911.
78. Shnyrov, V. L.; Sukhomudrenko, A. G. *Biophysical Chemistry* **1986**, *24*, 1.
79. Möller, C.; Büldt, G.; Dencher, N. A.; Engel, A.; Müller, D. J. *J. Mol. Biol.* **2000**, *301*, 869.
80. Lindahl, M.; Henderson, R. *Ultramicroscopy* **1997**, *70*, 95.
81. Sasaki, J.; Brown, L.; Chon, Y.-S.; Kandori, H.; Maede, A.; Needleman, R.; Lanyi, J. *Science* **1995**, *269*, 73.
82. Tittor, J.; Haupts, U.; Haupts, C.; Oesterhelt, D.; Becker, A.; Bamberg, E. *J. Mol. Biol.* **1997**, *271*, 405.
83. Facciotti, M. T.; Cheung, V. S.; Nguyen, D.; Rouhani, S.; Glaeser, R. M. *Biophys. J.* **2003**, *85*, 451.
84. Rhinow, D.; Hampp, N. *J. Phys. Chem.* **2010**, *114*, 549.
85. Heymann, J. A. W.; Havelka, W. A.; Oesterhelt, D. *Mol. Microbiol.* **1993**, *7*, 623.
86. Havelka, W. A.; Henderson, R.; Heymann, J. A. W.; Oesterhelt, D. *J. Mol. Biol.* **1993**, *234*, 837.
87. Persike, N.; Pfeiffer, M.; Radmacher, R. G. M.; Fritz, M. *J. Mol. Biol.* **2001**, *310*, 773.
88. Simons, K.; Toomre, D. *Nat. Rev. Mol. Cell. Biol.* **2000**, *1*, 31.
89. Haupts, U.; Tittor, J.; Bamberg, E.; Oesterhelt, D. *Biochemistry* **1997**, *36*, 2.
90. Subramaniam, S.; Henderson, R. *Nature* **2000**, *406*, 653.
91. Lanyi, J. K. *Annu. Rev. Physiol.* **2004**, *66*, 665.
92. Subramaniam, S.; Henderson, R. *Biochimica et Biophysica Acta* **2000**, *1460*, 157.
93. Porschke, D. *J. Mol. Biol.* **2003**, *331*, 667.
94. Subramaniam, S.; Gerstein, M.; Oesterhelt, D.; Henderson, R. *EMBO J.* **1993**, *12*, 1–8.
95. Sass, H. J.; Schachowa, I. W.; Rapp, G.; Koch, M. H. J.; Oesterhelt, D.; Dencher, N. A.; Büldt, G. *EMBO J.* **1997**, *16*, 1484–1491.
96. Rouhani, S.; Cartailler, J.-P.; Facciotti, M. T.; Walian, P.; Needleman, R.; Lanyi, J. K.; Glaeser, R. M.; Luecke, H. *J. Mol. Biol.* **2001**, *313*, 615.
97. Rhinow, D.; Hampp, N. A. *J. Phys. Chem. B.* **2008**, *112*, 13116.

98. Turner, G. J.; Miercke, L. J. W.; Thorgeirsson, T. E.; Kliger, D. S.; Betlach, M. C.; Stroud, R. M. *Biochemistry* **1993**, *32*, 1332.
99. Müller, D. J.; Schoenenberger, C.-A.; Büldt, G.; Engel, A. *Biophysical Journal* **1996**, *70*, 1796.

9 Publications

Cumulative part of dissertation

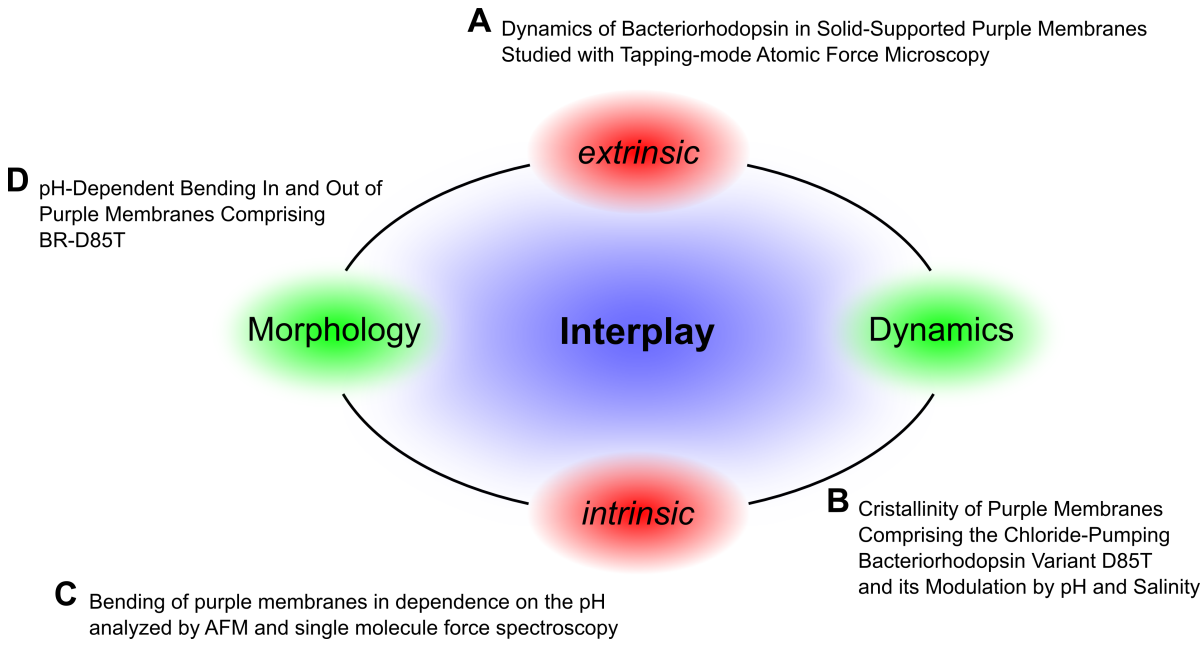

Addendum

E PHOTOCHEMISTRY OF COUMARIN-FUNCTIONALIZED SiO_2 NANOPARTICLES.
KEHRLOESSER, D.; BAUMANN, R.-P.; KIM, H.-C.; HAMPP, N.
Langmuir, **2011**, *27*, 4149-4155.

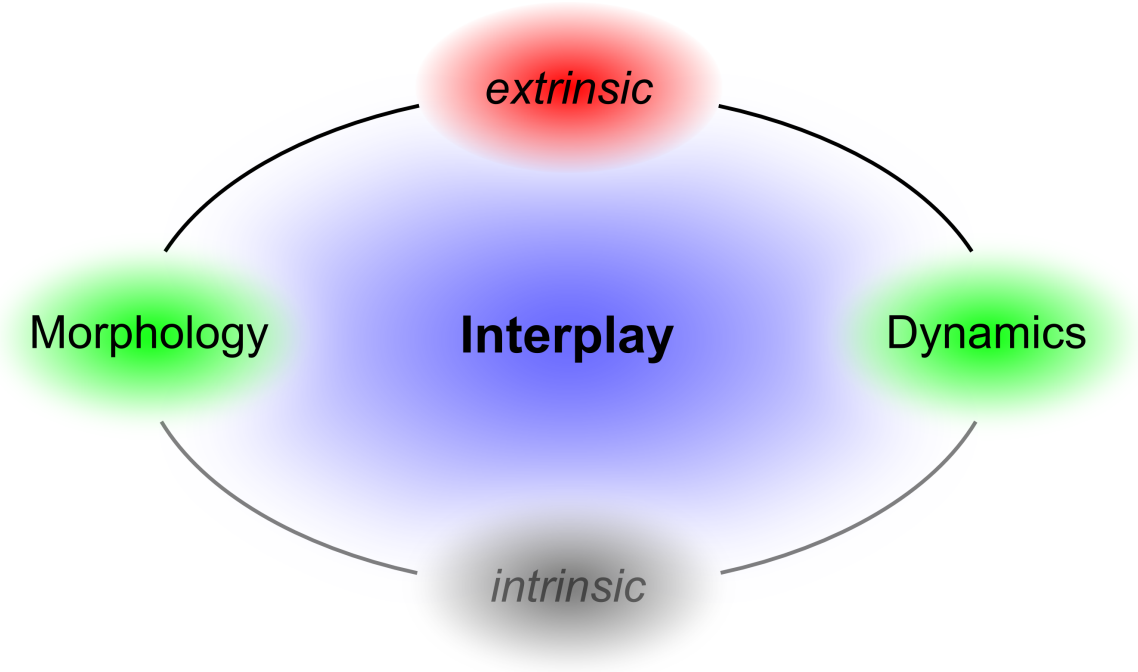

A **Dynamics of Bacteriorhodopsin in Solid-Supported Purple Membranes Studied with Tapping-Mode Atomic Force Microscopy.**
Schranz, M. and Baumann, R.-P.; Rhinow, D.; Hampp, N.
J. Phys. Chem. B, **2010**, *114*, 9047-9053.

B **Crystallinity of Purple Membranes Comprising the Chloride-Pumping Bacteriorhodopsin Variant D85T and its Modulation by pH and Salinity**
Rhinow, D.; Chizhik, I.; Baumann, R.-P.; Noll, F.; Hampp, N.
J. Phys. Chem. B, **2010**, *114*, 15424-15428.

C **Bending of purple membranes in dependence on the pH analyzed by AFM and single molecule force spectroscopy**
Baumann, R.-P.; Schranz, M.; Hampp, N.
PCCP, **2010**, *12*, 4329-4335.

D **pH-Dependent Bending In and Out of Purple Membranes Comprising BR-D85T**
Baumann, R.-P.; Eussner, J; Hampp, N.
submitted to PCCP

Dynamics of Bacteriorhodopsin in Solid-Supported Purple Membranes Studied with Tapping-Mode Atomic Force Microscopy

Michael Schranz,[⊥,†] Roelf-Peter Baumann,[⊥,†] Daniel Rhinow,[‡] and Norbert Hampp*[,†,§]

Department of Chemistry, Philipps-University of Marburg, Hans-Meerwein-Strasse Building H, D-35032 Marburg, Germany, Department of Structural Biology, Max-Planck-Institute of Biophysics, Max-von-Laue-Strasse 3, D-60438 Frankfurt, Germany, and Material Sciences Center, D-35032 Marburg, Germany

Received: March 16, 2010; Revised Manuscript Received: May 11, 2010

Purple membrane (PM) from *Halobacterium salinarum*, which comprises bacteriorhodopsin (BR) and lipids only, has been employed by many groups as a model system to study the structure and dynamics of membrane proteins. Although the conformational dynamics of BR within PM has been extensively analyzed with subnanometer resolution by means of diffraction experiments and spectroscopic methods, as well, structural studies of dynamical transitions within single PMs are rare. In this work, we show that tapping-mode atomic force microscopy (TM-AFM) is ideally suited to study dynamical transitions within solid-supported PMs at the nanoscale. Time-dependent AFM analysis of solid-supported PMs shows that redistribution processes take place between a crystalline core region, featuring a height of ∼5 nm, and a highly mobile rim region (∼4 nm in height). Furthermore, we discuss the influence of temperature and substrate on the equilibrium. The experiments are complemented by electrostatic force microscopy (EFM) of PM on mica. Beyond their importance for many physiological processes, dynamical transitions in biological membranes, as observed in this work, are of critical importance for all methods that make use of solid-supported membrane assemblies, either analytical tools or applications.

Introduction

Within their native hosts, biological membranes show a high degree of spatial and temporal organization.[1−3] To understand membrane-based processes such as endocytosis and signal transduction, it is necessary to study the dynamical behavior of the proteins and lipids that build up the corresponding membranes. Several methods have been developed to investigate the mobility of membrane components, among them fluorescence recovery after photobleaching[4] and single particle trapping microscopy.[5] Despite these efforts, it is still difficult to study both the structure and dynamics of biological membranes at the nanoscale. Beyond cell biological implications, the dynamic properties of biomolecular assemblies, confined to a two-dimensional environment, are of critical importance in methods that employ solid-supported biomolecules, ranging from analytical methods, such as atomic force microscopy (AFM)[6] and surface plasmon resonance[7] to applications such as functional thin film assemblies.[8] Maintaining functionality and structural integrity of solid-supported biomolecules is an indispensable prerequisite for the long-term stability of such systems as a whole.

Purple membranes (PM) from *Halobacterium salinarum* are naturally occurring two-dimensional crystals that comprise bacteriorhodopsin (BR) and lipids only.[9−11] Within its native lipid environment, BR is astonishingly stable and therefore serves as an ideal model system to study structure and dynamics of protein-rich biological membranes at the nanoscale.

In former studies, AFM has provided fundamental insights into the surface structure of solid-supported PMs at subnanometer resolution.[12−16]

Although it has been known for a long time that above ∼70 °C, the crystalline assembly of PM is transformed to a molten state,[17] in which individual BR trimers can diffuse freely, the dynamical behavior of BR in solid-supported PMs has only recently been addressed by means of structural analysis.[18]

In this work, we use tapping-mode atomic force microscopy (TM-AFM) as well as electrostatic force microscopy (EFM) to study the dynamical behavior of BR molecules in PMs immobilized on different substrates. We demonstrate that BR trimers located at the rim of PM undergo dynamic transitions that have not been observed in earlier studies but can be visualized by tapping-mode atomic force microscopy. Our experiments reveal that the dynamic properties of BR trimers critically depend on the substrate chosen for the immobilization of PMs. The measurements are complemented by EFM.

Materials and Methods

Materials. Purple membranes from *H. salinarum* containing bacteriorhodopsin wild-type were a gift from Dieter Oesterhelt's lab at the Max-Planck-Institute of Biochemistry, Martinsried, Germany. All PM preparations were freshly purified according to standard procedures.[19]

Mica was purchased from Plano GmbH, Wetzlar, Germany and freshly cleaved before sample preparation. Template-stripped gold (TSG) substrates were prepared via vapor deposition techniques.[20] Silicon wafers were a gift from Wacker Chemistry AG, Germany (Si 1-0-0 type N, P-doped, H-terminated, polished (625 ± 15 μm), resistivity 800−1600 Ω cm^{-1}) and were treated by sulfuric/peroxide (piranha) solution prior to usage.

* Corresponding author. Phone: +49 6421 2825775. Fax: +49 6421 2825798. E-mail: hampp@staff.uni-marburg.de.
† Philipps-University of Marburg.
‡ Max-Planck-Institute of Biophysics.
§ Material Sciences Center.
⊥ These authors contributed equally to this work.

10.1021/jp102377c
Published on Web 05/28/2010

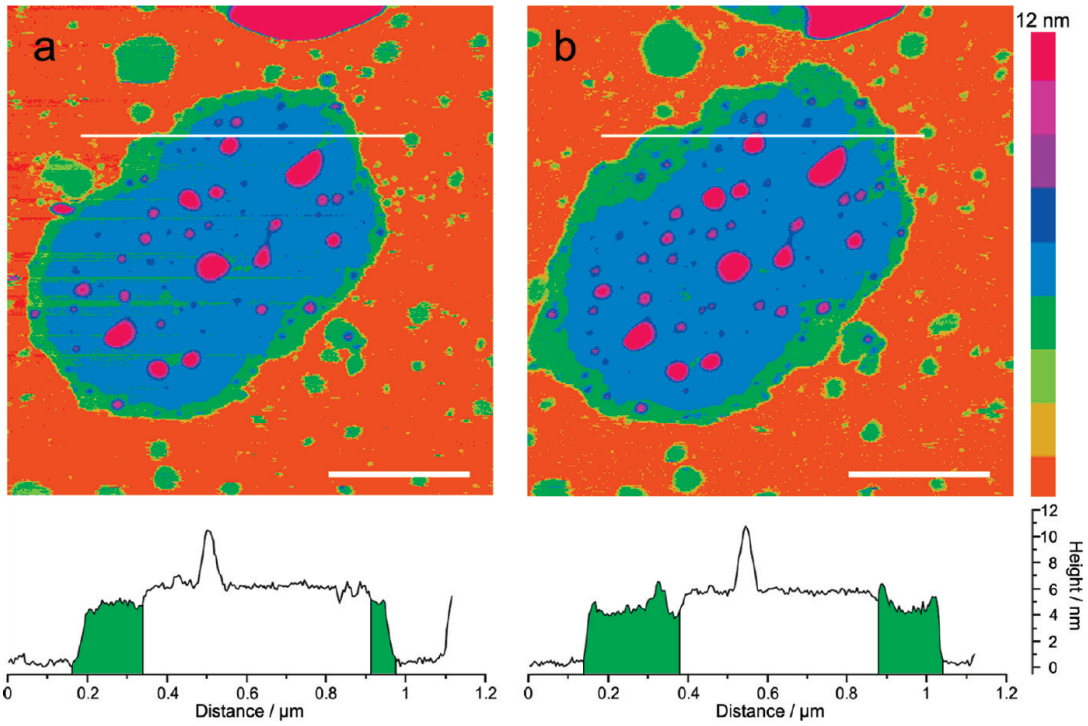

Figure 1. Time-dependent dynamical transitions in purple membrane comparing and contrasting (a) freshly prepared PM, and (b) the same PM after 100 min at room temperature. Dynamical transitions in the rim regions have occurred, and the membrane geometry has changed. Both TM-AFM height images are shown in false color representation, where the different membrane heights are given in different colors. Green areas are about 4 nm and blue areas about 6 nm in height. Red dots (about 11 nm) correspond to PM double layers. The white lines in the false color images indicate the sections of which the height profiles (shown below) were taken. Scale bars are 500 nm.

Sample Preparation. The purple membrane stock solutions were diluted in a suspension buffer (150 mM KCl, 10 mM Tris−HCl, pH 8.2) to a final absorbance (OD) between 0.2 and 0.3 at 570 nm. Five microliters of the PM suspension were pipetted together with 50 μL of imaging buffer (300 mM KCl, 10 mM Tris−HCl, pH 7.8) onto 1 cm $\times$1 cm substrate pieces of mica, TSG, or silicon wafer. After 30 min of incubation, excess material was removed by extensive rinsing with imaging buffer (10 $\times$ 20 μL). The samples were then mounted onto the sample stage and were allowed to reach thermal equilibrium (30 min) before analysis. For EFM measurements, samples were carefully dried in air after rinsing and were measured immediately once mounted onto the sample stage.

Temperature Jump Experiment. After measuring at room temperature, the imaging buffer was exchanged with imaging buffer preheated to a defined temperature. Once thermal equilibrium was re-established, further images of the same sample and area were taken.

Atomic Force Microscopy. AFM imaging was performed in liquid (imaging buffer) on a Nanoscope IV system (Veeco, Santa Barbara, CA). Pyramidal, oxide-sharpened Si_3N_4 tips (k = 0.08 N/m, f_0 = 24−44 kHz, which is reduced to ~9 kHz in liquid) attached to a V-shaped substrate (Olympus, Tokyo, Japan) were used for imaging. All images were measured using tapping-mode AFM with constant amplitude attenuation. The cantilever approach was performed with a drive amplitude of 250 mV. To achieve high-resolution images, the drive amplitude was lowered to about 50 mV, and the set point was adjusted to minimal forces.

EFM measurements were conducted in air using SCM-PIT tips (antimony (n) doped Si, k = 1−5 N/m, f_0 = 70−83 kHz, 0.01−0.025 Ω/cm, Veeco, Santa Barbara, CA) utilizing the Nanoscope's LiftMode feature. This mode of surface potential detection is a two-pass procedure in which the surface topography is obtained by standard tapping mode in the first pass, and the surface potential is measured on the second pass. Between the first and second passes, the tip is moved to a configurable lift height above the sample surface. On the second pass, the tip is moved at a constant height, tracing the topography that was recorded in the first pass. The two measurements are thus interleaved, that is, they are each measured one line at a time.

Results and Discussion

We observed that the rim region of PMs differs from the core region with respect to structure and dynamics. Figure 1a shows a height image of a single PM patch on mica as acquired by TM-AFM in liquid at room temperature (please refer to the Supporting Information for the respective AFM raw images without false coloring). In comparison with the central region, characterized by an average height of 5.2 nm, the PM is surrounded by a rim region featuring a height of only ~4 nm (Figure 1, bottom). Several smaller patches next to the large PM exhibit the same height of 4 nm as the rim. Most of these change their shape or seem to fuse with other structures over time, underlining their mobility.

Time-dependent TM-AFM analysis revealed the dynamic nature of the PM rim region. Within 100 min at room temperature, redistribution processes have taken place at the interface between the core region of PM and the rim region (Figure 1b), clearly discernible by the heights of 5.2 and 4 nm respectively (Figure 1, bottom). Although the relative amount of the two species changed in favor of the more dynamic 4 nm species over the indicated time frame, the absolute amount of PM remained virtually unchanged (Figure 1a,b). This indicates that the dynamics observed are due to a reversible material exchange between the two-dimensionally ordered core region of PM and a highly mobile rim region.

The speed of redistribution could be increased significantly when the temperature of the buffer was increased to 60 °C, which is still well below the reversible phase transition temperature of 70 °C for PM suspended in solution[17,21] but coincides with the temperature at which the mobility of the peptide groups of BR and their exposure to molecules of the external medium is at a maximum.[22] Figure 2b shows a TM-AFM image of an extended PM patch acquired after a temperature jump has been applied to the initial membrane (Figure 2a). As highlighted by the false coloring chosen, the geometry as well as the relative amount of PM regions with heights of 5.2 and 4 nm has completely and, in this case, irreversibly changed over the whole PM patch (Figure 2, bottom). According to Shnyrov et al.[21] the exposure of buried BR residues is associated with an irreversible molecular rearrangement of the membrane, leading to a less compact protein−lipid packing within the crystalline lattice of PM. Such a transition would alter the equilibrium between the 5.2 nm rigid core and 4 nm mobile rim regions in favor of the more dynamic 4 nm species due to decreased intramembrane forces, E_{PM}, which is illustrated by the dramatic changes observed during the temperature jump experiment.

The question arises, which interactions determine the stability of PM on surfaces? Forces between BR and lipids within the membrane stabilize the two-dimensional crystalline assembly, as shown by the aforementioned experimental results. However, both membrane components interact with the mica substrate, as well. The interplay between these forces can be expressed by the following equations, which signify a stability criterion for PM not just on mica, but on any given substrate:

$$E_{PM} = E_{BR\text{-}BR} + E_{lipid-lipid} + E_{BR\text{-}lipid} \quad (1)$$

$$E_s = E_{BR\text{-}substrate} + E_{lipid\text{-}substrate} \quad (2)$$

As soon as the energy of PM−surface interactions exceeds the binding energy of the crystal lattice, that is, $E_{PM} < E_S$, BR and lipids occupy a mobile state characterized by a reduced height of ~4 nm, as compared with the value of 5.2 nm for crystalline PM. Obviously, the crystal energy E_{PM} of BR molecules and lipids decreases with increasing distance from the core region of PM. From the stability criterion formulated above, it can be followed further that no crystalline PM can exist on a given surface once the PM size falls below a certain critical size. On mica substrates, this size is estimated to be <100 nm.

Figure 3 shows time-dependent TM-AFM images of PM on mica, which reveal the disassembly of a small PM fragment, manually released from the larger PM with the AFM tip. The two-dimensional crystalline lattice is well-resolved for both PMs (Figure. 3a, b). Two different lattices, which have slightly different angular orientations, contribute to the Fourier transform (Figure 3b, inset). The small PM patch is rotated a few degrees against the orientation of the large PM patch. Because of the unfavorable perimeter-to-area ratio, the displaced small PM fragment (diameter ~ 100 nm) starts to disassemble and vanishes completely within a time period of <40 min (Figure 3b−f), thus resembling a two-dimensional variant of the well-known Ostwald ripening. Furthermore, the TM-AFM images demonstrate that rearrangement of unit cells is ubiquitous along the edge of the large PM patch.

After ~30 min of incubation time, the rim shape of the large PM (Figure 3a) has completely changed (Figure 3f). Figure 4 summarizes the changes in area of both the small and large membranes shown in Figure 3. Over the course of observation, both PMs shrink continuously, while the area of the mobile rim increases in size. If the progression of the surfaces is plotted

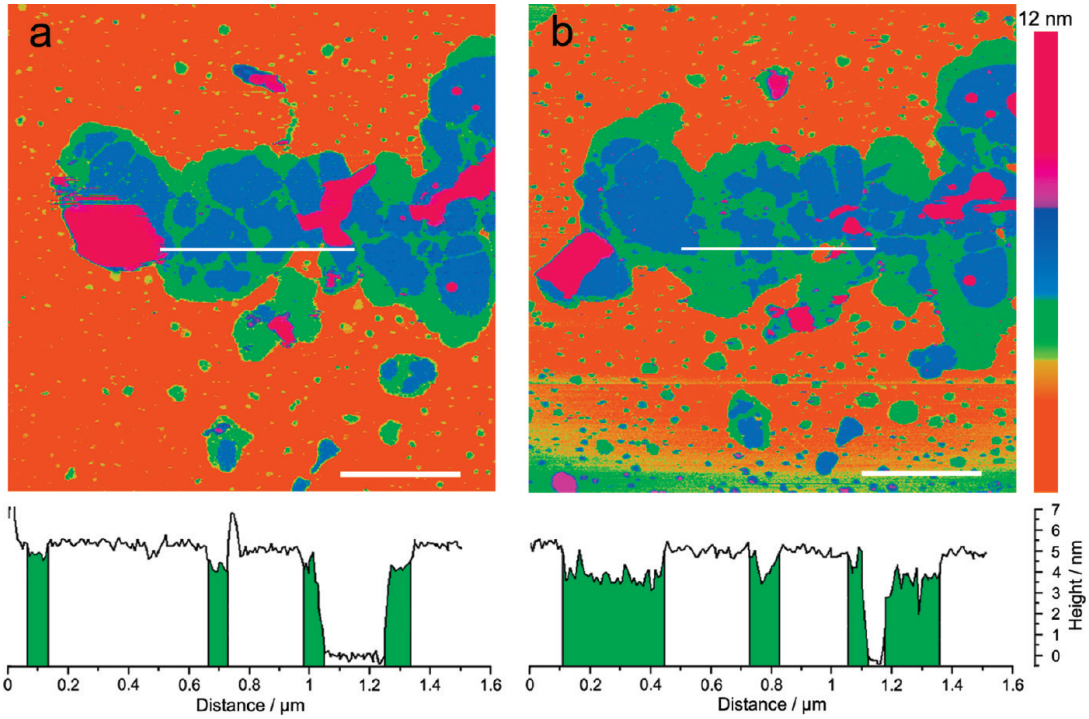

Figure 2. TM-AFM false color height images of (a) freshly prepared PMs and (b) 90 min after a pulse-type exposure to 60 °C imaging buffer. Dynamical transitions have led to a large redistribution of 4 nm areas (green) and 6 nm areas (blue). The volume increase of 4 nm areas (green) equals the volume loss of 6 and 11 nm areas (blue and red). Scale bars are 1 μm.

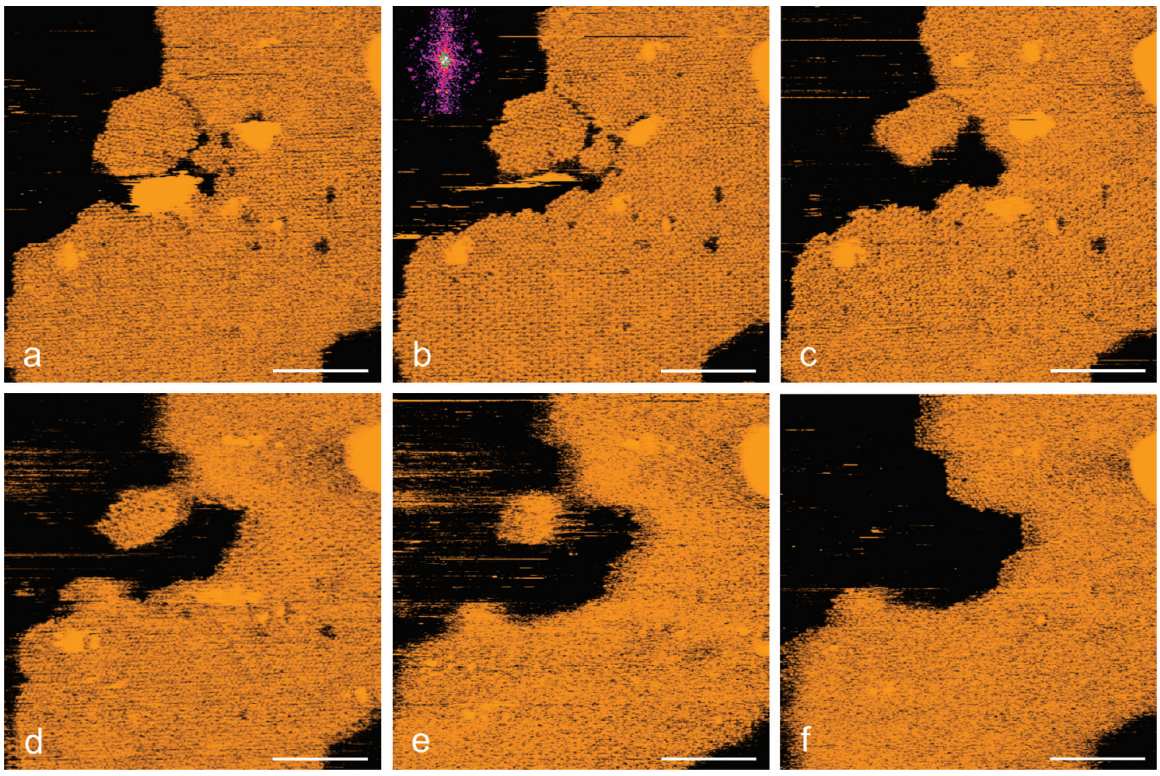

Figure 3. Time-dependent morphological changes of purple membrane on mica at room temperature. The changes are best observed by tracking the displaced PM fragment of about 50−100 nm in size located in the upper left corner of the imaged PM. (b) Both PM patches are crystalline, as may be seen from the Fourier transform (inset), but possess two different angular orientations. During the 33 min of observation (a, 0 min; b, 5:38 min; c, 11:15 min; d, 22:34 min; e, 28:18 min; and f, 33:48 min), the small displaced PM fragment completely disappears; only the much larger PM patch remains. Scale bars are 100 nm.

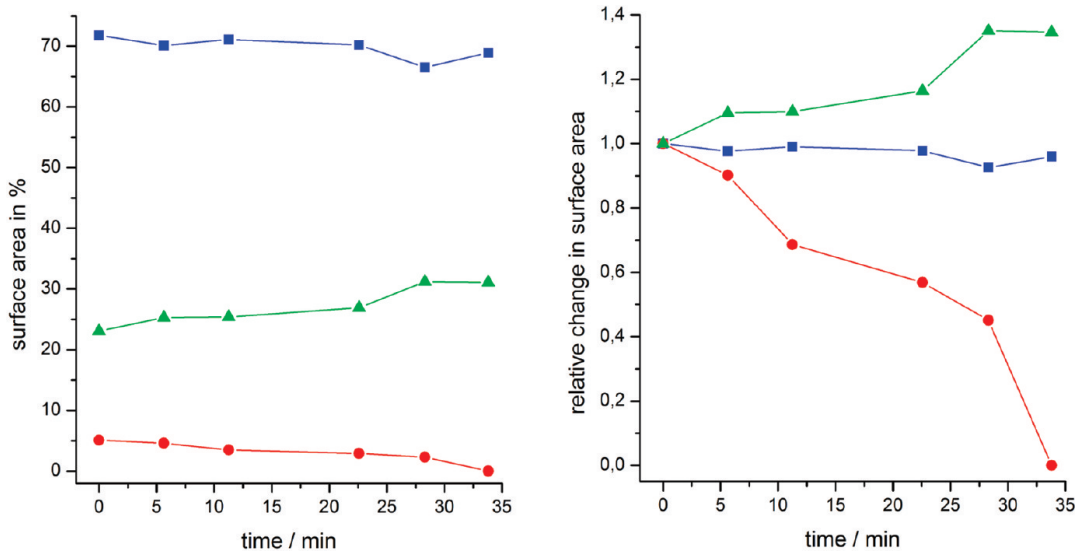

Figure 4. Area changes of the large (blue squares) and small (red circles) purple membrane as well as the surrounding mobile rim (green triangles) from Figure 3 (the data points correspond to Figure 3a−f; the lines are to guide the eye). Both membranes shrink continuously. Over the course of observation of ∼34 min, the small membrane completely vanishes. The right graph shows the change in area relative to the initial areas: the small membrane shrinks with an increasing speed. The increase in area in the last step of the large membrane could be interpreted as an incorporation of the small one.

relative to their initial size, the increasing speed of shrinkage of the smaller membrane in comparison with the large one is obvious (Figure 4, right). Between Figure 3e and f, the small membrane finally vanishes, which gives rise to a small increase in the large membranes size. A possible interpretation would be the incorporation of the small membrane into the edge of the large one. The dynamics of two-dimensional atomic islands on surfaces has been investigated by other groups that employed STM methods to analyze the mechanisms of Ostwald ripening in a quantitative manner.[23,24] Further investigations have to be done to analyze the dynamics of biological assemblies such as PM on surfaces in a similar way (e.g., time-dependent observation of PM dynamics at different temperatures).

Interestingly, dynamic processes within PM were not observed when the mica substrate was exchanged for silicon wafers or TSG. Figure 5a and b show PM patches immobilized on silicon and gold, respectively. In contrast to images acquired on mica, no differences are observed for the rim region and the

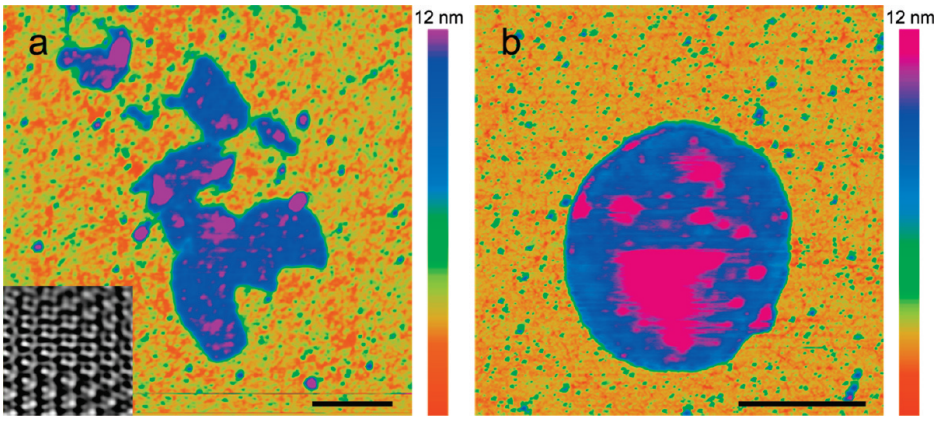

Figure 5. Purple membrane on silicon and template stripped gold. (a) PM on silicon. The height of the PM appears to be ~7.4 nm, which is a little bit higher than on mica due to the greater surface roughness of the silicon wafer; however, molecular resolution is still obtained using tapping mode AFM (inset). (b) PM on TSG. The height of the PM is ~6.5 nm. The mobile rim region is absent on both substrates. Scale bars are 1 μm in panel a and 500 nm in panel b.

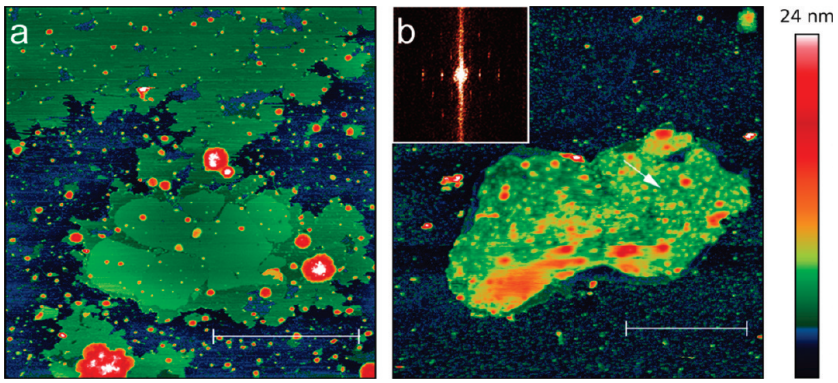

Figure 6. Long-term stability of solid-supported PMs. Shown are PM patches on mica (a) and a silicon wafer (b) after 4 days. Due to strong surface interactions on mica, all but a few PMs in the middle reside in a highly disordered, mobile state exhibiting a height of ~4 nm. The increased surface roughness of the silicon wafer, however, reduces possible membrane-substrate interactions. This effectively suppresses dynamic transitions of the immobilized PM, and only a very small mobile rim region has formed over the 4 day period. Despite its rough appearance, the imaged membrane is fully crystalline, as can be seen from the Fourier transform (inset) of the indicated (white arrow) part of the PM. Scale bars are 2 μm in panel a and 1 μm in panel b.

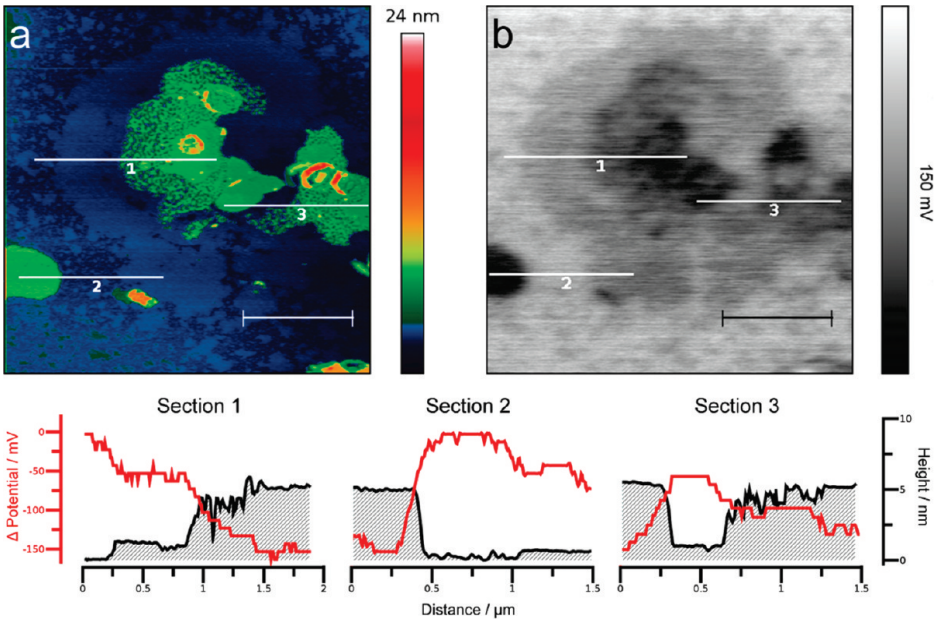

Figure 7. Electrostatic force microscopy of PM on mica showing (a) the topography and (b) the respective surface potential. Both core and mobile rim regions of PM in various states of delamination are distinguishable. Sections 1−3 compare and contrast the height and respective surface potential of these different regions marked by the white lines in both images. Scale bars are 1 μm.

core region of PM. We conclude that in the case of silicon and gold, the crystal binding energy exceeds the energy of PM-substrate interactions at all positions where PM is in contact with the substrate. This also holds true over prolonged periods of time.

On mica, the equilibrium of the reversible material exchange between the two-dimensionally ordered core region of PM and a highly mobile rim region is strongly shifted over time. Figure 6a shows that after 4 days, almost all PMs have changed their morphology in favor of the 4 nm, more mobile state.

On silicon wafers or TSG, the opposite is the case, as shown in Figure 6b. Substrate roughness is a key parameter that might be of critical importance in that case. Although freshly cleaved mica is atomically flat over micrometers by default (average roughness: $R_a = 0.021$ nm), the TSG substrates (average roughness: $R_a = 0.169$ nm) and silicon-wafers (average roughness: $R_a = 0.295$ nm) show height variations in the subnanometer range. These fluctuations decrease the number of contact points between PM and the substrate, thus lowering the van-der-Waals forces between sample and support and, thus, E_S.

The critical influence of substrate roughness on lipid mobility is known from other experiments.[25,26] We complemented our TM-AFM experiments by EFM of PM on mica. PM patches were analyzed in a two-pass interleaved procedure, where the surface topography was obtained by standard TM-AFM first and the surface potential of the sample was probed by EFM utilizing Veeco's LiftMode in the second pass.

Figure 7a center shows a TM-AFM image of a large PM on mica, acquired in air. The core region (height ~5 nm) is surrounded by an extended rim region of ~4 nm height, thus resembling the results obtained with TM-AFM in buffer. However, this 4 nm rim region features many fissures, and yet another region of ~2 nm height surrounding both core and 4 nm domains is clearly discernible. We believe that both the fissures and the 2 nm layer are a direct result of the drying process owing to the reduced E_{PM} of the mobile phase with respect to the core of PM. Unlike the core regions, which are not altered during the drying procedure, the 4 nm highly mobile rim region lacks any kind of two-dimensional order or strong, stabilizing internal interactions. As a result, this lipid bilayer will partially delaminate from the support once exposed to the air/water interface[27] leaving behind a fissured 4 nm bilayer as well as a 2 nm lipid monolayer. Delamination occurs because it is energetically unfavorable to remove the hydrophilic head groups from the solvation buffer. Consequently, the 4 nm bilayer reorganizes to expose some of its lipid chains to the nascent air/water interface, while others form new vesicles within the receding aqueous phase.

Congruously, the rim region is visible in the corresponding EFM image (Figure 7b) featuring two different potentials for the 2 and 4 nm domains. Although the 2 nm region bears almost no charge, which is indicative of a lipid monolayer, the local electric field above the 4 nm region is similar to but not the same as the crystalline core of PM. Although an absolute assessment of the electrostatic field distribution is not possible in the setup used due to the insulating nature of the mica substrate, relative estimations can still be performed with high accuracy.[28] This is underlined by the fact that even the two sides of PM may be differentiated within the EFM images shown. According to their surface charge, both sides of PM may be attributed to either the less negatively charged cytoplasmic (CP) or the more negatively charged extracellular side (EC).[28] On mica, the potential difference between both sides is ~20 mV,[28] which is in good agreement with our results. Membranes to the left and in the center of Figure 7 are thus oriented such that their EC side faces upward, and the PM on the far right features the CP side up.

Conclusions

By means of time- and temperature-dependent TM-AFM, we have found that solid-supported PMs are prone to dynamical redistribution processes that occur predominantly in the rim region of the membrane patches. Furthermore, we have demonstrated that EFM is a valuable tool to analyze the nanoscale organization of biological membranes, thus ideally complementing topographic analysis by AFM. The structural integrity of solid-supported PMs is maintained by a balance of forces that act between the membrane constituents and between PM and the substrate, as well. Our experiments reveal that substrate roughness is a key parameter that enables or slows down dynamical transitions within solid-supported PMs. We observed that on a time scale of several days, the crystalline assembly of PMs, immobilized on atomically smooth mica, is dissolved completely in favor of a highly disordered state. In contrast to this, dynamical transitions are not observed when PM is immobilized on much rougher substrates such as silicon wafers or gold. Beyond the biological aspect, our experiments are of critical interest for all researches in the field of nanobiotechnology in which long-term stability of thin-film devices is highly desired.

Supporting Information Available: AFM height images without false coloring of Figures 1 and 2. This information is available free of charge via the Internet at http://pubs.acs.org.

References and Notes

(1) Ikonen, E.; Simons, K. Functional Rafts in Cell Membranes. *Nature* **1997**, *387*, 569–772.

(2) Toomre, D.; Simons, K. Lipid Rafts and Signal Transduction. *Nat. Rev. Mol. Cell. Biol.* **2000**, *1*, 31–39.

(3) Anderson, R. G. W.; Jacobson, K. A Role for Lipid Shells in Targeting Proteins to Caveolae, Rafts and Other Lipid Domains. *Science* **2002**, *296*, 1821–1825.

(4) Jacobson, K.; Ishihara, A.; Inman, R. Lateral Diffusion of Proteins in Membranes. *Annu. Rev. Physiol.* **1987**, *49*, 163–175.

(5) Saxton, M. J.; Jacobson, K. Single-Particle Tracking: Applications to Membrane Dynamics. *Annu. Rev. Biophys. Biomol. Struct.* **1997**, *26*, 373–379.

(6) Engel, A.; Müller, D. J. Observing Single Biomolecules at Work with the Atomic Force Microscope. *Nat. Struct. Biol.* **2000**, *7*, 715–718.

(7) Homola, J. Surface Plasmon Resonance Sensors for Detection of Chemical and Biological Species. *Chem. Rev.* **2008**, *108*, 462–493.

(8) He, J.-A.; Samuelson, L.; Li, L.; Kumar, J.; Tripathy, S. K. Bacteriorhodopsin Thin Film Assemblies−Immobilization, Properties, and Applications. *Adv. Mater.* **1999**, *11*, 435–446.

(9) Haupts, U.; Tittor, J.; Oesterhelt, D. Closing In on Bacteriorhodopsin: Progress in Understanding the Molecule. *Annu. Rev. Biophys. Biomol. Struct.* **1999**, *28*, 367–399.

(10) Krebs, M. P.; Isenbarger, T. A. Structural Determinants of Purple Membrane Assembly. *Biochim. Biophys. Acta* **2000**, *1460*, 15–26.

(11) Renner, C.; Kessler, B.; Oesterhelt, D. Lipid Composition of Integral Purple Membrane by ^{1}H and ^{31}P NMR. *J. Lipid Res.* **2005**, *46*, 1755–1764.

(12) Müller, D. J.; Amrein, M.; Engel, A. Adsorption of Biological Molecules to a Solid Support for Scanning Probe Microscopy. *J. Struct. Biol.* **1997**, *119*, 172–188.

(13) Müller, D. J.; Heymann, J. B.; Oesterhelt, F.; Möller, C.; Gaub, H.; Büldt, G.; Engel. A. Atomic Force Microscopy of Native Purple Membranes. *Biochim. Biophys. Acta* **2000**, *1460*, 27–38.

(14) Müller, D. J.; Engel, A. The Height of Biomolecules Measured with the Atomic Force Microscope Depends on Electrostatic Interactions. *Biophys. J.* **1997**, *73*, 1633–1644.

(15) Müller, D. J.; Fotiadis, D.; Scheuring, S.; Müller, S. A.; Engel, A. Electrostatically Balanced Subnanometer Imaging of Biological Specimens by Atomic Force Microscope. *Biophys. J.* **1999**, *76*, 1101–1111.

(16) Butt, H.-J. Measuring Local Surface Charge Densities in Electrolyte Solutions with a Scanning Force Microscope. *Biophys. J.* **1992**, *63*, 578–582.

(17) Jackson, M. B.; Sturtevant, J. M. Phase Transitions of the Purple Membranes of *Halobacterium halobium*. *Biochemistry* **1978**, *17*, 911–915.

(18) Yamashita, H.; Voïtchovsky, K.; Uchihashi, T.; Contera, S. A.; Ryan, J. F.; Ando, T. Dynamics of Bacteriorhodopsin 2D Crystal Observed by High-Speed Atomic Force Microscopy. *J. Struct. Biol.* **2009**, *167*, 153–158.

(19) Oesterhelt, D.; Stoeckenius, W. Isolation of the Cell Membrane of *Halobacterium halobium* and Its Fractionation into Red and Purple Membrane. *Methods Enzymol.* **1974**, *31*, 667–678.

(20) Wagner, P.; Hegner, M.; Guentherodt, H.-J.; Semenza, G. Formation and In Situ Modification of Monolayers Chemisorbed on Ultraflat Template-Stripped Gold Surfaces. *Langmuir* **1995**, *11*, 3867–3875.

(21) Shnyrov, V. L.; Mateo, P. L. Thermal Transitions in the Purple Membrane from *Halobacterium halobium*. *FEBS Lett.* **1993**, *324*, 237–240.

(22) Shnyrov, V. L.; Sukhomudrenko, A. G. Dynamic Properties of Purple Membranes upon Heat Treatment. *Biophys. Chem.* **1986**, *24*, 1–4.

(23) Bott, M.; Hohage, M.; Morgenstern, M.; Michely, T.; Comsa, G. New Approach for Determination of Diffusion Parameters of Adatoms. *Phys. Rev. Lett.* **1996**, *76*, 1304–1307.

(24) Hannon, J. B.; Klünker, C.; Giesen, M.; Ibach, H.; Bartelt, N. C.; Hamilton, J. C. Surface Self-Diffusion by Vacancy Motion: Island Ripening on Cu(001). *Phys. Rev. Lett.* **1997**, *79*, 2506–2509.

(25) Rädler, J.; Strey, H.; Sackmann, E. On the Phenomenology and Kinetics of Lipid Bilayer Spreading on Hydrophilic Surfaces. *Langmuir* **1995**, *11*, 4539–4548.

(26) Cremer, P. S.; Boxer, S. G. Formation and Spreading of Lipid Bilayers on Planar Glass Supports. *J. Phys. Chem. B* **1999**, *103*, 2554–2559.

(27) Daniel, S.; Albertorio, F.; Cremer, P. S. Making Membranes Rough, Tough, and Ready to Hit the Road. *MRS Bull.* **2006**, *31*, 536–540.

(28) Knapp, H. F.; Mesquida, P.; Stemmer, A. Imaging the Surface Potential of Active Purple Membrane. *Surf. Interface Anal.* **2002**, *33*, 108–112.

JP102377C

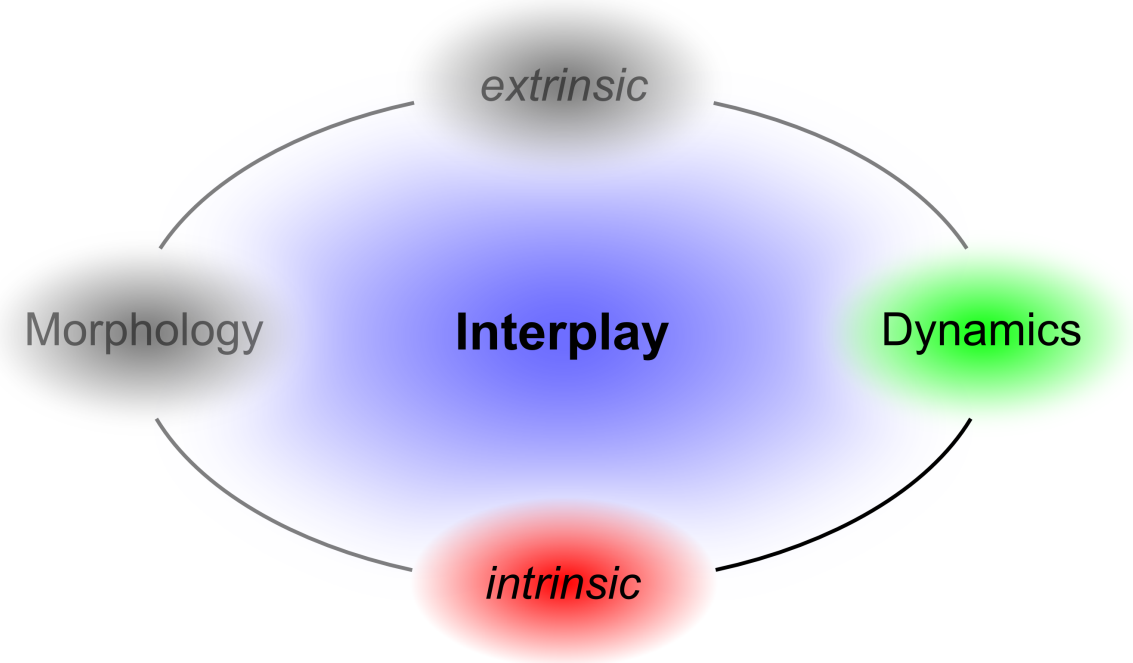

A DYNAMICS OF BACTERIORHODOPSIN IN SOLID-SUPPORTED PURPLE MEMBRANES STUDIED WITH TAPPING-MODE ATOMIC FORCE MICROSCOPY.
Schranz, M. and Baumann, R.-P.; Rhinow, D.; Hampp, N.
J. Phys. Chem. B, **2010**, *114*, 9047-9053.

B CRYSTALLINITY OF PURPLE MEMBRANES COMPRISING THE CHLORIDE-PUMPING BACTERIORHODOPSIN VARIANT D85T AND ITS MODULATION BY PH AND SALINITY
Rhinow, D.; Chizhik, I.; Baumann, R.-P.; Noll, F.; Hampp, N.
J. Phys. Chem. B, **2010**, *114*, 15424-15428.

C BENDING OF PURPLE MEMBRANES IN DEPENDENCE ON THE PH ANALYZED BY AFM AND SINGLE MOLECULE FORCE SPECTROSCOPY
Baumann, R.-P.; Schranz, M.; Hampp, N.
PCCP, **2010**, *12*, 4329-4335.

D PH-DEPENDENT BENDING IN AND OUT OF PURPLE MEMBRANES COMPRISING BR-D85T
Baumann, R.-P.; Eussner, J; Hampp, N.
submitted to PCCP

Crystallinity of Purple Membranes Comprising the Chloride-Pumping Bacteriorhodopsin Variant D85T and Its Modulation by pH and Salinity

Daniel Rhinow,[†] Ivan Chizhik,[‡] Roelf-Peter Baumann,[‡] Frank Noll,[‡] and Norbert Hampp*[,‡,§]

Max-Planck-Institute of Biophysics, Department of Structural Biology, Max-von-Laue-Str. 3, D-60438 Frankfurt, Germany, Philipps-University of Marburg, Department of Chemistry, Hans-Meerwein-Str. Bldg. H, D-35032 Marburg, Germany, and Material Sciences Center, D-35032 Marburg, Germany

Received: September 6, 2010

Self-assembly of membrane proteins inside the cell membrane critically depends on specific protein−protein and protein−lipid interactions. Purple membranes (PMs) from *Halobacterium salinarum* comprise wild-type bacteriorhodopsin (BR) and lipids only and form a 2-D crystalline lattice of P3 symmetry in the cell membrane. It is known that removal of the retinylidene residue as well as the exchange of selected amino acids lead to a loss of crystallinity. In PMs comprising the BR variant D85T, we have observed a tunable tendency to form crystalline domains, which depends on pH-value and chloride ion concentration. BR-D85T resembles the function of the chloride pump halorhodopsin. The protonation state of amino acid residues within the binding pocket and chloride binding in the vicinity of the protonated retinal Schiff base affect the overall shape of BR-D85T molecules in the membrane, thereby changing their interactions and subsequently their tendency to form crystalline areas. The combination of small-angle X-ray scattering, atomic force microscopy, and freeze-fracture electron microscopy enables us to analyze the transitions statistically as well as on the single membrane level. PM-D85T is a model system to study membrane protein association upon substrate binding in a native environment. Furthermore, the ability to reversibly modulate the crystallinity of PMs probably will be useful for the preparation of larger artificial crystalline arrays of BR and its variants.

Introduction

The light-driven proton pump bacteriorhodopsin (BR) is the key protein of halobacterial photosynthesis.[1−3] Within its native host, BR forms 2-D crystalline patches, the so-called purple membranes (PMs), from *Halobacterium salinarum*, which comprise BR trimers and lipids only.[2,4] BR is the prototype of seven transmembrane helix proteins and shares deep homologies with other microbial retinal proteins.[5−11] High-resolution structural analysis of BR has revealed a detailed molecular picture of light-dependent vectorial proton transport through the cell membrane.[12−17] Furthermore, PM is an excellent model system to study the principles that are responsible for the assembly of integral membrane protein complexes in their native environment.[4] A variety of studies have been performed to elucidate the molecular determinants of PM stability and crystalline assembly. For example, analysis of genetically modified BR variants has revealed several amino acid residues, which are critical for lattice assembly.[4,18] Furthermore, it has been shown that mutations in the core of BR can affect lattice assembly as well.[19] The importance of retinal, covalently bound to lysine 216, for structural integrity of BR and PM lattice assembly has been pointed out in another study.[20]

In this work, we demonstrate how a single-point mutation in the core of BR results in PMs, which undergo structural changes from a noncrystalline state to a 2D-crystalline state, depending on the physicochemical conditions. In BR variant D85T, the primary proton acceptor aspartic acid 85 is replaced by threonine, the equivalent residue in halorhodopsin, which converts BR into a chloride pump.[21,22] By means of small-angle X-ray scattering (SAXS), transmission electron microscopy (TEM), and atomic force microscopy (AFM), we demonstrate that PM-D85T, noncrystalline under most conditions, is converted to a highly ordered hexagonal 2-D crystalline state as soon as the physicochemical conditions favor chloride binding of BR-D85T, i.e., pH values below pH 6 and high salinity. A model is presented which explains the crystallization tendency of PM-D85T in terms of conformational changes on the level of single BR-D85T molecules.

Materials and Methods

Materials. PM wild-type (PM-WT), PM-D85T, PM-D96N, and PM-D96G/F171C/F219L (PM-Tri) were freshly purified according to standard procedures.[23]

Small-Angle X-Ray Scattering. Oriented PM multilayers were prepared from PM suspended in distilled water or 0.1 M NaCl. Depending on the conditions desired, the pH was adjusted by phosphate buffer as well as dilute HCl. PM suspensions were deposited on a thin plastic substrate and slowly dried overnight. PM multilayers were analyzed with a SAXS apparatus comprising a Phillips PW1830 X-ray generator and a KKK-type Kratky camera (Anton Paar, Graz, Austria) with a sample detector distance of 200 mm.

Electron Microscopy. PM-D85T suspensions were placed between two small copper disks and plunged into liquid ethane. Replicas were prepared in a Balzers BAF 400T freeze-fracture unit at 3×10^{-7} mbar keeping the specimen stage at −130 °C. Shadowing with Pt/C was performed at an angle of 45°, followed by evaporation of pure carbon at 90° reinforcing the heavy metal replica. Replicas were thawed, cleaned from organic

* Corresponding author. Phone: +49 6421 2825775. Fax: +49 6421 2825798. E-mail: hampp@staff.uni-marburg.de.
[†] Max-Planck-Institute of Biophysics.
[‡] Philipps-University of Marburg.
[§] Material Sciences Center.

10.1021/jp108502p
Published on Web 10/29/2010

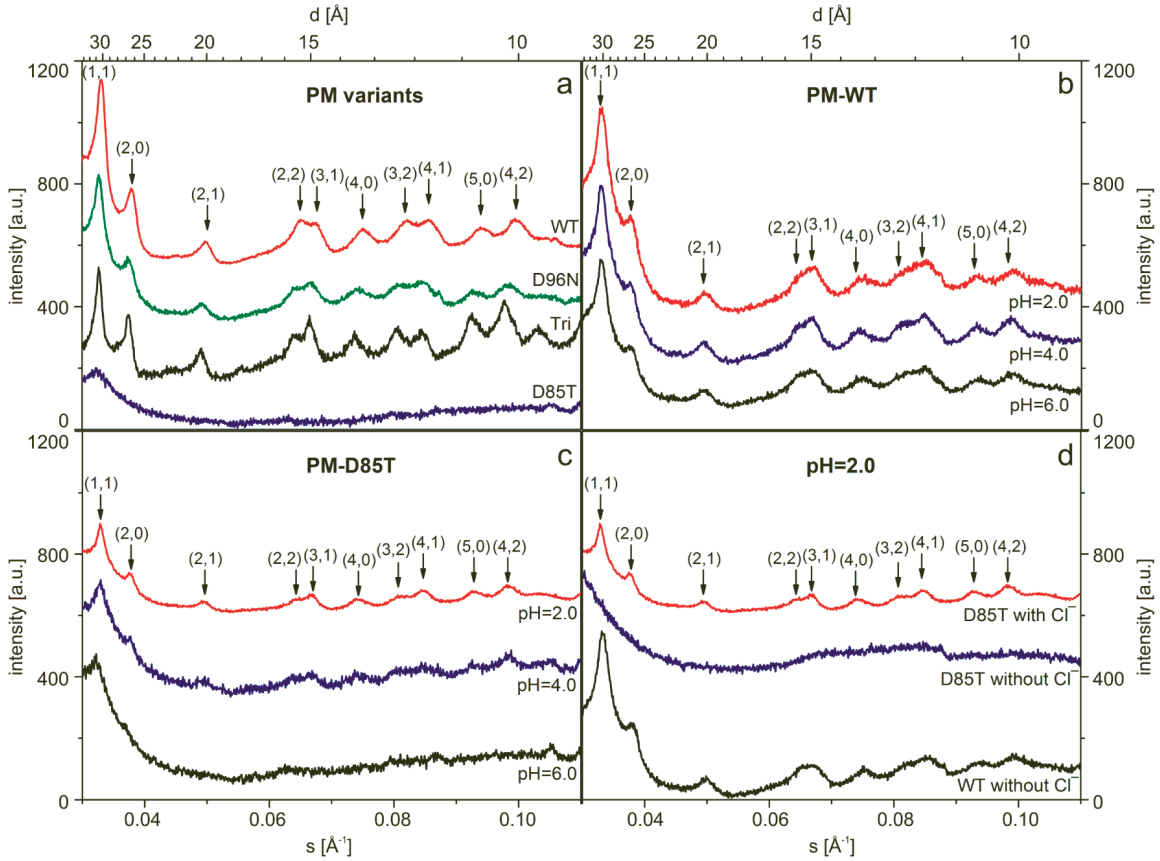

Figure 1. Analysis of PM lattice assembly on dependence of BR variant, pH, and chloride. (a) SAXS profiles of oriented PM multilayers. Films were obtained from PM variants suspended in distilled water. (b) Characteristic reflections due to regular crystalline lattice are visible in SAXS profiles of PM-WT at all pH-values. (c) PM-D85T is crystalline in the presence of chloride and pH < 6 having the same lattice type and cell dimensions as PM-WT. (d) Diffraction profiles of PM-D85T multilayers, obtained from suspensions of pH = 2 with and without chloride ions. In a chloride-free environment, PM-D85T is noncrystalline (blue graph). In the presence of chloride, PM-D85T forms a crystalline lattice (red graph), which resembles PM-WT (black graph).

material in chromosulfuric acid, and imaged with an EM208S electron microscope (FEI, Hillsboro, USA).

Atomic Force Microscopy. Silicon wafers were a gift from Wacker Chemistry AG, Germany (Si 1−0−0 type N, P doped, H terminated, polished (625 ± 15 μm), resistivity 800−1600 Ω cm) and were treated by sulfuric/peroxide (piranha) solution prior to usage. PM stock solutions were diluted in suspension buffer (150 mM KCl, pH = 3.4) to a final absorbance (OD) between 0.2 and 0.3 at 570 nm. An amount of 5 μL of the PM suspension was pipetted together with 50 μL of imaging buffer (300 mM KCl, pH = 3.4) onto 1 cm × 1 cm substrate pieces of mica or silicon wafer, respectively. After 30 min of incubation, excess material was removed by extensive rinsing with imaging buffer (10 times 20 μL). The samples were then mounted onto the sample stage and were allowed to reach thermal equilibrium (30 min) before analysis. AFM imaging was performed in liquid (imaging buffer) on a Nanoscope IV system (Veeco, Santa Barbara, CA, USA). Pyramidal, oxide-sharpened Si_3N_4 tips attached to a V-shaped substrate (Olympus, Tokyo, Japan) were used for imaging. All images were measured using tapping-mode AFM with constant amplitude attenuation. The cantilever approach was performed with a drive amplitude of 250 mV. To achieve high-resolution images, the drive amplitude was lowered to about 50 mV, while the set point was adjusted to minimal forces.

Molecular Modeling. Coordinates were obtained from pdb entries 1QHJ (BR-WT), 1JV7 (BR-D85S, anion-free), and 1MGY (BR-D85S, bromide-bound). All models were built using the program package Chimera.[24]

Results and Discussion

Structural Analysis of PM-D85T. We analyzed oriented PM-D85T multilayers at various pH values by SAXS in transmission geometry. In the absence of chloride ions PM-D85T did not diffract at pH values above 6. As an example, diffraction profiles of PM-D85T films, obtained from membranes suspended in distilled water of neutral pH, as well as PM-WT, PM-D96N, and PM-Tri as control samples, are shown in Figure 1a. In contrast to the control samples, e.g., PM-WT, which displayed characteristic reflections due to regular crystalline assembly, no reflections are visible in the case of PM-D85T (Figure 1a, blue graph). This means that the diameter of the coherent crystalline areas must be smaller than 5 unit cells, which would be sufficient to produce an X-ray diffraction pattern.[19] We conclude that in the absence of chloride and at about neutral pH value PM-D85T is in a noncrystalline state. The situation changes as soon as PM-D85T is analyzed at acidic pH values in the presence of NaCl. Figure 1c shows pH-dependent X-ray diffraction profiles of oriented PM-D85T films. Below pH = 6, diffraction spots characteristic for regular PM lattice assembly appear, which become sharper with decreasing pH value (Figure 1c). The PM-D85T reflections resemble the diffraction pattern of PM-WT, which has been analyzed under the same conditions (Figure 1b). The structural changes within PM-D85T are accompanied by spectroscopic changes. In the absence of NaCl and at pH > 6, PM-D85T has a bluish appearance. In the presence of chloride, PM-D85T has a purple appearance at pH < 6, which has been observed earlier.[22]

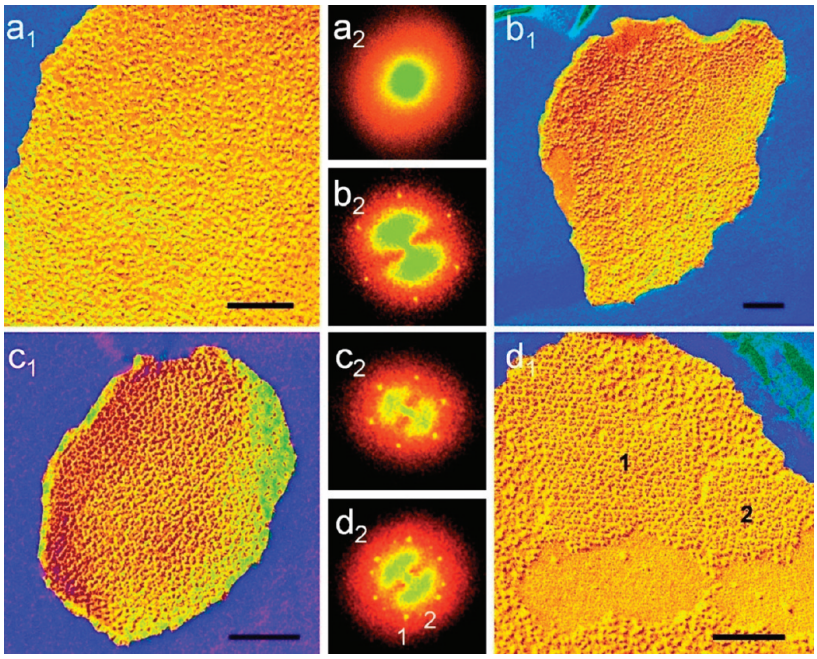

Figure 2. Freeze-fracture TEM of PM-D85T. (a_1) PM-D85T at pH = 8.3 in the absence of chloride. (a_2) Fourier transform of (a_1). (b_1) PM-D85T at pH = 4 in 1 M NaCl. A crystalline domain is visible in the top right part of the membrane. (b_2) Fourier transform of (b_1), which reveals spots due to a hexagonal lattice. (c_1) PM-D85T at pH = 4 in 1 M NaCl. A single-crystalline membrane comprising a continuous hexagonal lattice is shown. (c_2) Fourier transform of (c_1). (d_1) PM-D85T at pH = 4 in 1 M NaCl. A membrane patch is shown comprising two large crystalline domains (marked 1 and 2) with different angular orientation. (d_2) Fourier transform of (d_1), which reveals spots of two lattices with different angular orientations. Scale bars are 100 nm.

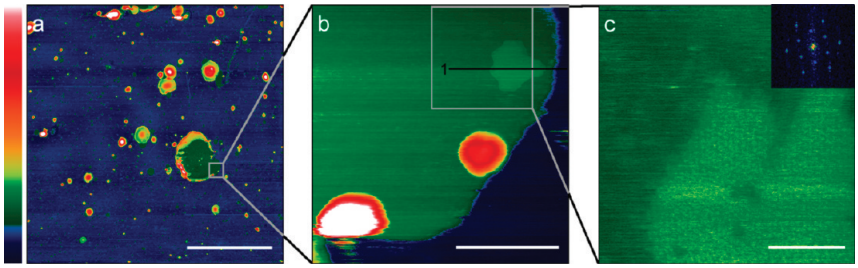

Figure 3. AFM analysis of PM-D85T at pH = 3.4 in 300 mM KCl. (a) Patches of PM-D85T on silicon. The scale bar is 5 μm, and the color scale is 50 nm. (b) Magnification of the boxed area in (a). The scale bar is 200 nm, and the color scale is 30 nm. A crystalline domain is visible. A section (1) through the crystalline domain as well as the noncrystalline area is indicated. (c) Magnified view of the crystalline domain boxed in (b). The scale bar is 50 nm, and the color scale is 10 nm.

We complemented SAXS analysis by freeze-fracture electron microscopy of PM-D85T. While SAXS analysis provides statistically substantiated diffraction data, transmission electron microscopy (TEM) provides insight into the assembly of individual patches of PM-D85T, which were analyzed in real space as well as in Fourier space. Figure $2a_1$ shows a freeze-fracture TEM image of PM-D85T, shock-frozen from slightly alkaline chloride-free suspension (pH = 8.1). No reflections are visible in the Fourier transform (Figure $2a_2$). PM-D85T comprised crystalline patches when suspended in 1 M NaCl at pH = 4. Figures $2b_1$, c_1, and d_1 show TEM images of freeze-fractured membranes, which clearly reveal a hexagonal crystal lattice in Fourier space (Figures $2b_2$, c_2, and d_2). Three different types of membranes were observed. In one case, PM-D85T comprised crystalline domains several 10 000 nm^2 in size, flanked by noncrystalline domains (Figure $2b_1$). Continuous single-crystalline membranes were observed as well (Figure $2c_1$). In other cases, membranes contained multiple crystalline domains with different angular orientation (Figure $2d_1$).

In addition, we studied PM-D85T by means of tapping-mode AFM in solution. We used silicon wafers as substrates for AFM imaging, which are rougher than atomically smooth mica, thus minimizing PM−substrate interactions.[25] Figure 3 shows AFM images of PM-D85T obtained in 300 mM KCl at pH = 3.4. A large membrane patch is visible, which includes a crystalline domain (Figure 3b,c). The Fourier transform reveals the structure factors of a hexagonal crystal lattice. A height difference of 1

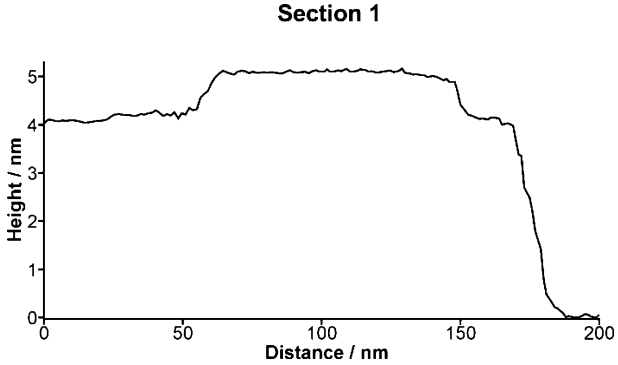

Figure 4. Cross section 1 marked in Figure 3b. Along this section, a height difference is observed between the crystalline domain (~5 nm) and the noncrystalline part of the membrane (~4 nm).

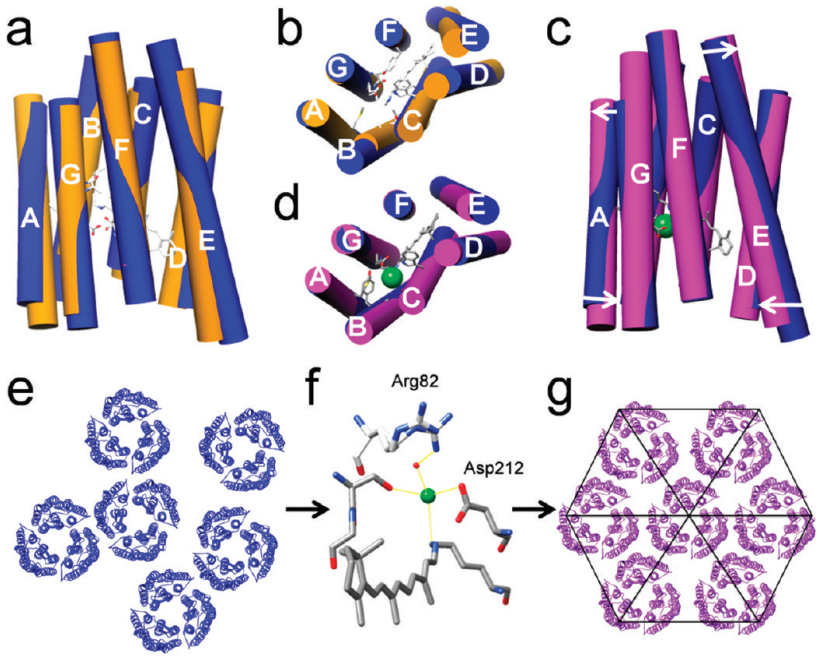

Figure 5. Model for chloride-mediated crystallization of PM-D85T. (a) Structural differences between PM-WT (yellow) and anion-free PM-D85S (blue). (b) Top view of (a), seen from the extracellular side. (c) Structural changes in BR-D85S (blue) upon anion binding (purple). Bromide is shown as a green sphere. Helical movements are indicated by white arrows. (d) Top view of (c), seen from the extracellular side. (e) Noncrystalline assembly of PM-D85T before anion binding. (f) Anion-binding site of BR-D85S as resolved in X-ray structure 1MGY. (g) Crystallization of PM-D85T upon chloride binding.

nm (Figure 4) is detectable between the crystalline domain (~5 nm) and the noncrystalline surrounding area (~4 nm), which was observed in an earlier study.[25] The detected crystalline domains exhibit certain structural dynamics and change in size over time (Figure 3b,c). Although generally increasing in size, we could hardly detect any domains with an edge length larger than ~200 nm. Apparently, the crystal lattice of PM-D85T forms less easily than the regular lattice of PM-WT and is therefore more prone to disruption by strong sample−surface interactions than PM-WT, even on rough substrates like silicon.

Model for Chloride-Mediated Crystallization of BR-D85T. Replacement of D85 in BR by threonine changes the pK_a values of virtually all amino acid residues responsible for proton translocation,[22,26−28] which has considerable effect on the structural integrity of BR. In BR-D85X (X = neutral amino acid), structural intermediates of the BR photocycle, which are formed in a light-dependent manner in PM-WT, are accessible by simply changing the pH of the suspension.[22,28,29] For example, BR-D85X mutants accumulate the M_2-state at alkaline pH comprising cytoplasmatically open BRs,[29] which affects membrane topology and lattice assembly due to wedge-shaped BRs.[30−32] A structural model of PM-D85S, a homologue of PM-D85T, has been obtained by X-ray crystallography,[33] which demonstrates that an O-like structural intermediate is formed at acidic pH values. Figure 5a highlights the differences between PM-D85S and PM-WT. The most extensive deviations occur on the extracellular side of BR. Helices A, B, D, and E tilt outward, which results in opening of the extracellular half-channel of BR-D85S (Figure 5a,b), thus leading to wedge-shaped BR molecules as well. It is very likely that the increased structural flexibility of BR-D85T negatively affects its crystallization tendency since PM lattice assembly depends critically on proper interactions between specific residues.[4] It has been shown by spectroscopy and transport measurements that an anion binding site is created in BR-D85T at pH < 7, which has a high affinity to chloride ions.[22] According to an X-ray structure of BR-D85S,[34] the anion is tightly bound in the retinal binding pocket as sketched in Figure 5f. It was demonstrated that anion binding by BR-D85S is accompanied by helical movements, which lead to closure of the extracellular channel, thus creating a wild-type-like structure.[34] Figures 5c and d illustrate the differences between anion-free and anion-bound BR-D85S. Anion binding at acidic pH values (Figure 5f) leads to wild-type-like BR molecules with reduced flexibility. Our experiments demonstrate that upon structural stabilization BR-D85T recovers its ability to form proper crystal contacts and subsequently forms a hexagonal lattice (Figure 5e,g).

Conclusions

By means of structural analysis via SAXS, TEM, and AFM, we have demonstrated that conversion of BR into a chloride pump by a single-point mutation seriously affects its crystallization tendency. PM-D85T forms coherent crystalline domains as soon as the tertiary structure of BR-D85T is stabilized by binding of chloride ions in the retinal binding pocket. In contrast to halorhodopsin, which has been shown to form orthogonal crystal patches with $p42_12$ symmetry in the membrane of an overproducing *Halobacterium salinarum* strain,[35−37] the chloride pump BR-D85T forms hexagonal crystals with wild-type-like p3 symmetry. The formation of crystalline membrane domains upon substrate binding, as observed in this work, is closely related to other recent topics of membrane biophysics, i.e., stimuli-dependent formation of membrane microdomains, which plays a major role in signal transduction.[38]

Acknowledgment. We thank Friederike Joos (MPI of Biophysics, Frankfurt) for skilled technical assistance with freeze-fracture electron microscopy. PM wild-type (PM-WT), PM-D85T, PM-D96N, and PM-D96G/F171C/F219L (PM-Tri) were a gift from Dieter Oesterhelt's lab at the Max-Planck-Institute of Biochemistry, Martinsried, Germany. We thank Werner Kühlbrandt (MPI of Biophysics, Frankfurt) for a critical reading of the manuscript.

References and Notes

(1) Oesterhelt, D.; Stoeckenius, W. Rhodopsin-like protein from the purple membrane of Halobacterium halobium. *Nat. New Biol.* **1971**, *233*, 149–152.

(2) Haupts, U.; Tittor, J.; Oesterhelt, D. Closing in on Bacteriorhodopsin: Progress in Understanding the Molecule. *Annu. Rev. Biophys. Biomol. Struct.* **1999**, *28*, 367–399.

(3) Lanyi, J. K. Bacteriorhodopsin. *Annu. Rev. Physiol.* **2004**, *66*, 665–688.

(4) Krebs, M. P.; Isenbarger, T. A. Structural Determinants of Purple Membrane Assembly. *Biochim. Biophys. Acta* **2000**, *1460*, 15–26.

(5) Kolbe, M.; Hüseyin, B.; Essen, L.-O.; Oesterhelt, D. Structure of the light-driven chloride pump halorhodopsin at 1.8 A. resolution. *Science* **2000**, *288*, 1390–1396.

(6) Luecke, H.; Schobert, B.; Lanyi, J. K.; Spudich, E. N.; Spudich, J. L. Crystal structure of sensory rhodopsin II at 2.4 angstroms: insights into color tuning and transducer interaction. *Science* **2001**, *293*, 1499–1503.

(7) Royant, A.; Nollert, P.; Edman, K.; Neutze, R.; Landau, E. M.; Pebay-Peyroula, E.; Navarro, J. X-ray structure of sensory rhodopsin II at 2.1 Å resolution. *Proc. Natl. Acad. Sci. U.S.A.* **2001**, *98*, 10131–10136.

(8) Gordeliy, V. I.; Labahn, J.; Moukhametzianov, R.; Efremov, R.; Granzin, J.; Schlesinger, Büldt, G.; Savopol, T.; Scheidig, A. J.; Klare, J. P.; Engelhard, M. Molecular basis of transmembrane signalling by sensory rhodopsin II-transducer complex. *Nature* **2002**, *419*, 484–487.

(9) Vogley, L.; Sineshekov, O. A.; Vishwa, D. T.; Sasaki, J.; Spudich, J.; Luecke, H. Anabaena sensory rhodopsin: a photochromic color sensor at 2.0 Å. *Science* **2004**, *306*, 1390–1393.

(10) Balashov, S. P.; Imasheva, E. S.; Boichenko, V. A.; Antón, J.; Wang, J. M.; Lanyi, J. K. Xanthorhodopsin: a proton pump with a light-harvesting carotenoid antenna. *Science* **2005**, *309*, 2061–2064.

(11) Spudich, J. L. The multitalented microbial sensory rhodopsins. *Trends Microbiol.* **2006**, *14*, 480–487.

(12) Grigorieff, N.; Ceska, T. A.; Downing, K. H.; Baldwin, J. M.; Henderson, R. Electron-crystallographic refinement of the structure of bacteriorhodopsin. *J. Mol. Biol.* **1996**, *259*, 393–421.

(13) Kimura, Y.; Vassylyev, D. G.; Miyazawa, A.; Kidera, A.; Matsushima, M.; Mitsuoka, K.; Murata, K.; Hirai, T.; Fujiyoshi, Y. Surface of bacteriorhodopsin revealed by high-resolution electron crystallography. *Nature* **1997**, *389*, 206–211.

(14) Essen, L.-O.; Siegert, R.; Lehmann, W. D.; Oesterhelt, D. Lipid patches in membrane protein oligomers: crystal structure of the bacteriorhodopsin-lipid complex. *Proc. Natl. Acad. Sci. U.S.A.* **1998**, *95*, 11673–11678.

(15) Luecke, H.; Schobert, B.; Richter, H.-T.; Cartailler, J.-P.; Lanyi, J. Structure of bacteriorhodopsin at 1.55 Å resolution. *J. Mol. Biol.* **1999**, *291*, 899–911.

(16) Sass, H. J.; Büldt, G.; Gessenich, R.; Hehn, D.; Neff, D.; Schlesinger, R.; Berendzen, J.; Ormos, P. Structural alterations for proton translocation in the M state of wild-type bacteriorhodopsin. *Nature* **2000**, *406*, 649–653.

(17) Subramaniam, S.; Henderson, R. Molecular mechanism of vectorial proton translocation by bacteriorhodopsin. *Nature* **2000**, *406*, 653–657.

(18) Sapra, K. T.; Hüseyin, B.; Oesterhelt, D.; Müller, D. J. Characterizing molecular interactions in different bacteriorhodopsin assemblies by single-molecule force spectroscopy. *J. Mol. Biol.* **2006**, *355*, 640–650.

(19) Lindahl, M.; Henderson, R. Structure of the bacteriorhodopsin D85N/D96N double mutant showing substantial structural changes and a highly twinned disordered lattice. *Ultramicroscopy* **1997**, *70*, 95–106.

(20) Möller, C.; Büldt, G.; Dencher, N. A.; Engel, A.; Müller, D. J. Reversible loss of crystallinity on photobleaching purple membrane in the presence of hydroxylamine. *J. Mol. Biol.* **2000**, *301*, 869–879.

(21) Sasaki, J.; Brown, L. S.; Chon, Y. S.; Kandori, H.; Maeda, A.; Needleman, R.; Lanyi, J. K. Conversion of bacteriorhodopsin into a chloride ion pump. *Science* **1995**, *269*, 73–75.

(22) Tittor, J.; Haupts, U.; Haupts, C.; Oesterhelt, D.; Becker, A.; Bamberg, E. Chloride and proton transport in bacteriorhodopsin mutant D85T: Different Modes of Ion Translocation in a Retinal Protein. *J. Mol. Biol.* **1997**, *271*, 405–416.

(23) Oesterhelt, D.; Stoeckenius, W. Isolation of the cell membrane of Halobacterium halobium and its fractionation into red and purple membrane. *Methods Enzymol.* **1974**, *31*, 667.

(24) Pettersen, E. F.; Goddard, T. D.; Huang, C. C.; Couch, G. S.; Greenblatt, D. M.; Meng, E. C.; Ferrin, T. E. UCSF Chimera—A visualization system for exploratory research and analysis. *J. Comput. Chem.* **2004**, *25*, 1605–1612.

(25) Schranz, M.; Baumann, R.-P.; Rhinow, D.; Hampp, N. Dynamics of Bacteriorhodopsin in Solid-Supported Purple Membranes Studied with Tapping-Mode Atomic Force Microscopy. *J. Phys. Chem. B* **2010**, *114*, 9047–9053.

(26) Tittor, J.; Schweiger, U.; Oesterhelt, D.; Bamberg, E. Inversion of proton translocation in bacteriorhodopsin mutants D85N, D85T, and D85,96N. *Biophys. J.* **1994**, *67*, 1682–1690.

(27) Tittor, J.; Oesterhelt, D.; Bamberg, E. Bacteriorhodopsin mutants D85N, D85T and D85,96N as proton pumps. *Biophys. Chem.* **1995**, *56*, 153–157.

(28) Turner, G. J.; Miercke, J. W.; Thorgeirsson, T. E.; Kliger, D. S.; Betlach, M. C.; Stroud, R. M. Bacteriorhodopsin D85N: Three spectroscopic species in equilibrium. *Biochemistry* **1993**, *32*, 1332–1337.

(29) Brown, L.; Kamikubo, H.; Zimányi, L.; Kataoka, M.; Tokunaga, F.; Verdegem, P.; Lugtenburg, J.; Lanyi, J. K. A local electrostatic change is the cause of the large-scale protein conformation shift in bacteriorhodopsin. *Proc. Natl. Acad. Sci. U.S.A.* **1997**, *94*, 5040–5044.

(30) Rhinow, D.; Hampp, N. A. Light- and pH-dependent conformational changes in protein structure induce strong bending of purple membranes - active membranes studied by cryo-SEM. *J. Phys. Chem. B* **2008**, *112*, 13116–13120.

(31) Baumann, R.-P.; Schranz, M.; Hampp, N. Bending of purple membranes in dependence on the pH analyzed by AFM and single molecule force spectroscopy. *Phys. Chem. Chem. Phys.* **2010**, *12*, 4329–4335.

(32) Rhinow, D.; Hampp, N. Curvature of Purple Membranes Comprising Permanently Wedge-Shaped Bacteriorhodopsin Molecules Is Regulated by Lipid Content. *J. Phys. Chem. B* **2010**, *114*, 549–556.

(33) Rouhani, S.; Cartailler, J. P.; Facciotti, M. T.; Walian, P.; Needleman, R.; Lanyi, J. K.; Glaeser, R. M.; Luecke, H. Crystal structure of the D85S mutant of bacteriorhodopsin: Model of an O-like photocycle intermediate. *J. Mol. Biol.* **2001**, *313*, 615.

(34) Facciotti, M. T.; Cheung, V. S.; Nguyen, D.; Rouhani, S.; Glaeser, R. M. Crystal structure of the bromide-bound D85S mutant of bacteriorhodopsin: Principles of ion pumping. *Biophys. J.* **2003**, *85*, 451–458.

(35) Heymann, J. A. W.; Havelka, W. A.; Oesterhelt, D. Homologous overexpression of a light-driven anion pump in an archaebacterium. *Mol. Microbiol.* **1993**, *7*, 623–630.

(36) Havelka, W. A.; Henderson, R.; Heymann, J. A. W.; Oesterhelt, D. Projection structure of halorhodopsin from *Halobacterium halobium* at 6 Å resolution obtained from electron cryo-microscopy. *J. Mol. Biol.* **1993**, *234*, 837–845.

(37) Persike, N.; Pfeiffer, M.; Guckenberger, R.; Radmacher, M.; Fritz, M. Direct observation of different surface structures on high-resolution images of native halorhodopsin. *J. Mol. Biol.* **2001**, *310*, 773–780.

(38) Simons, K.; Toomre, D. Lipid rafts and signal transduction. *Nat. Rev. Mol. Cell. Biol.* **2000**, *1*, 31–41.

JP108502P

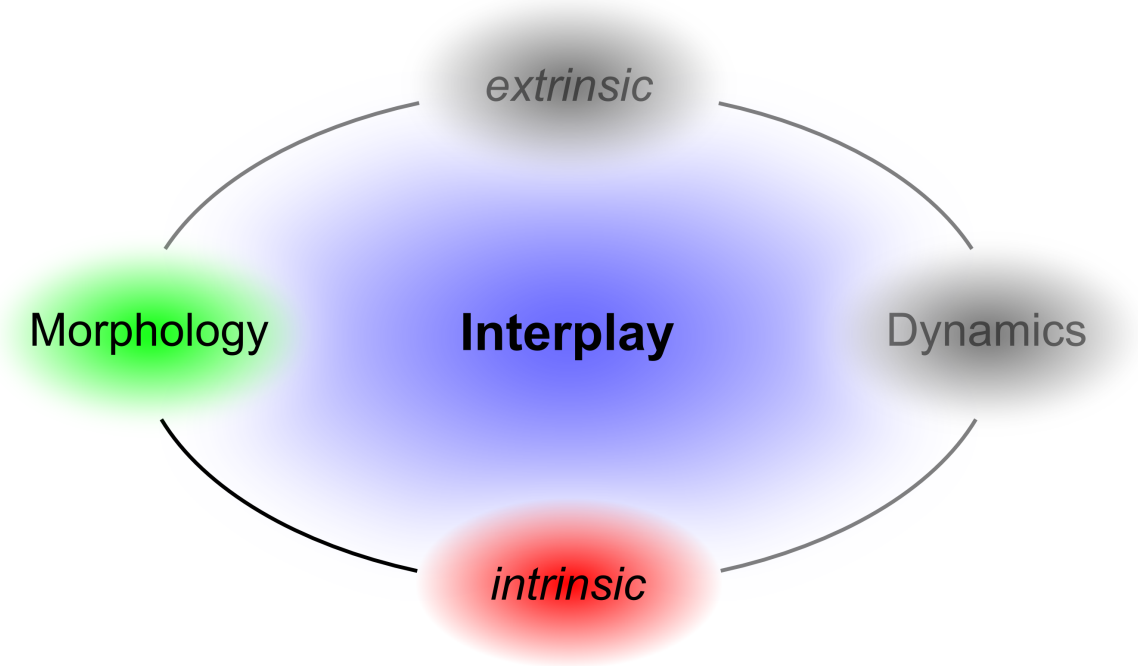

A DYNAMICS OF BACTERIORHODOPSIN IN SOLID-SUPPORTED PURPLE MEMBRANES STUDIED WITH TAPPING-MODE ATOMIC FORCE MICROSCOPY.
Schranz, M. and Baumann, R.-P.; Rhinow, D.; Hampp, N.
J. Phys. Chem. B, **2010**, *114*, 9047-9053.

B CRYSTALLINITY OF PURPLE MEMBRANES COMPRISING THE CHLORIDE-PUMPING BACTERIORHODOPSIN VARIANT D85T AND ITS MODULATION BY pH AND SALINITY
Rhinow, D.; Chizhik, I.; Baumann, R.-P.; Noll, F.; Hampp, N.
J. Phys. Chem. B, **2010**, *114*, 15424-15428.

C **BENDING OF PURPLE MEMBRANES IN DEPENDENCE ON THE pH ANALYZED BY AFM AND SINGLE MOLECULE FORCE SPECTROSCOPY**
Baumann, R.-P.; Schranz, M.; Hampp, N.
PCCP, **2010**, *12*, 4329-4335.

D pH-DEPENDENT BENDING IN AND OUT OF PURPLE MEMBRANES COMPRISING BR-D85T
Baumann, R.-P.; Eussner, J; Hampp, N.
submitted to PCCP

Bending of purple membranes in dependence on the pH analyzed by AFM and single molecule force spectroscopy†

R.-P. Baumann,*[a] M. Schranz[a] and N. Hampp[ab]

Received 22nd September 2009, Accepted 18th January 2010
First published as an Advance Article on the web 23rd February 2010
DOI: 10.1039/b919729j

The first AFM images of strongly bent purple membranes as well as the first single molecule force spectra of bacteriorhodopsins embedded therein are presented. AFM images of purple membranes to date always showed a flat membrane topology. Bacteriorhodopsin variants like BR-D85N and BR-D85T resemble an intermediate state of wild-type BR which is slightly 'wedge'-shaped. Due to the strong interaction within the 2-D crystalline lattice of the purple membrane, the geometrical anisotropy of the individual bacteriorhodopsins adds up to a macroscopic change in the geometry of the purple membranes. Instead of being flat they appear like domes at physiological conditions. Single molecule force spectroscopy was employed to determine the absolute sign of the membrane curvature. As the bacteriorhodopsins in the center of the dome-like purple membranes are not supported by any solid state substrate, the presented force spectra are the first of non-supported bacteriorhodopsin, resembling the natural occurrence in the halobacterial cell.

Introduction

Purple membranes (PM) consist of the membrane protein bacteriorhodopsin (BR) packed in a hexagonally 2D-crystalline lattice and lipids only.[1,2] The protein's secondary structure comprises seven transmembrane α-helical domains, interlinked by loop segments, which enclose a pocket where the retinylidene chromophore is located. Specifically, the chromophore is bound to Lys-216 *via* a Schiff-base linkage. Upon irradiation with *e.g.* green light BR passes through a well studied photocycle.[3–6] Each pass results in the transport of a proton from the cytoplasmic (CP) to the extracellular (EC) side of the membrane. The proton transport is intimately linked to a well-studied series of protonation changes of several key amino acids inside the extracellular and cytoplasmic half channels as well as the Schiff-base linkage.[7,8]

In 1987 Czege and Rheinisch studied PM through light scattering experiments and postulated a light-induced bending of the PM in solution.[9] The reason for this finding was unclear, however an asymmetric charge distribution due to the light-induced proton transport was assumed to be the cause of the bending. Several years ago Porschke used electro-optical techniques to reexamine this phenomenon[10] and concluded, considering high-resolution 3D-structures of BR[7] which had become available in the meantime, that conformational changes within the BR structure must be responsible for the bending of the PM as a whole. Recently we have proven the light- and pH-induced bending of PM making it visible by cryo-scanning electron microscopy.[11] Utilizing AFM techniques we are now able to directly observe bent purple membranes in solution at physiological conditions. For this purpose BR variants of the BR-D85X-type, in particular BR-D85T and BR-D85N were used. In order to differentiate between the two sides of purple membranes, the cytoplasmic and the extracellular side, we used force spectroscopy and were able to determine the bending direction experimentally, which had not been possible in the aforementioned studies. The BRs in the bent PMs are not in contact with any solid surface, but only in contact with buffer on both sides. This resembles the situation in the halobacterial cell. So we present here the first images and force spectra of non-supported BRs.

Bacteriorhodospin and its shape changes during proton transport

If BR is irradiated with light, the all-*trans* retinylidene group is isomerized to the twisted 13-*cis*, 14-s-*cis*, 15-*anti* conformation (Fig. 1).[8,12] This energy uptake leads, over several intermediates, to the deprotonation of the Schiff-base in the M_1-state of the

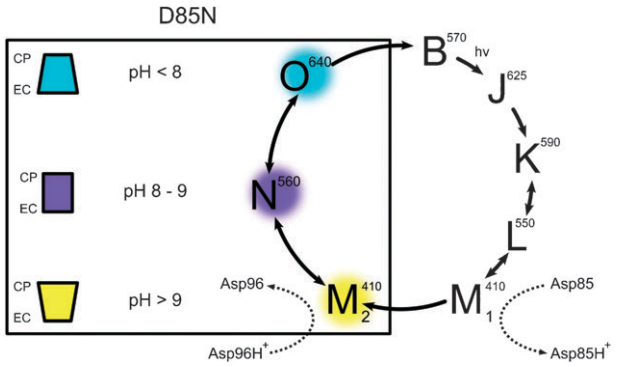

Fig. 1 Bacteriorhodopsin photocycle highlighting the three intermediates, which variant BR-D85N accumulates in, in dependence on the pH[13] and the postulated associated shape changes of the protein.[14]

[a] *Philipps-University of Marburg, Department of Chemistry, Hans-Meerwein-Str. Bldg. H, D-35032 Marburg, Germany. E-mail: hampp@staff.uni-marburg.de; Fax: +49-6421-2825798; Tel: +49-6421-2825775*
[b] *Material Sciences Center, D-35032 Marburg, Germany*

† Electronic supplementary information (ESI) available: Data of the analysis of the shape of dome-like purple membranes containing BR-D85N and BR-D85T on mica. See DOI: 10.1039/b919729j

photocycle. During the essentially irreversible transition from M_1 to M_2,[15] which is accompanied by a conformational change of the retinylidene residue from 13-*cis*, 14-s-*cis*, 15-*anti* to 13-*cis*, 14-s-*trans*, 15-*anti*, the cytoplasmic half-channel of BR is opened in order for the Schiff-base to be reprotonated in the N-state (Table 1). The opening of the CP half-channel alters the BR morphology to become wedge-shaped[7,16,17] (Fig. 2). Because of the strong coupling between the BR trimers in the two-dimensional crystalline lattice of the PMs, a sufficient super-numerary count of wedge-shaped proteins within the PM leads to a macroscopic bending at physiological conditions.

In order to observe such bending of PM-sheets, however, an accumulation of the M_2-state is a prerequisite. Membranes containing the BR variant BR-D96N, which has a prolonged lifetime of the M_2-state[18] and for this reason is a key variant for potential technical applications,[19–21] have thus been found to exhibit the proposed bending if irradiated with light.[11] However, as BR-D96N is not trapped in the M_2-state but still exhibits the entire photocycle, the accumulation occurs under non-equilibrium conditions resulting more in a macroscopic crumbling rather than a well defined bending of the membranes.[11]

Depending on the pH, the BR-D85N and BR-D85T variants exist in an equilibrium of three spectroscopically distinguishable species (see Fig. 1). A predominantly blue state at pH values lower than 8, a predominantly purple state in the range of pH 8–9 and a predominantly yellow state at higher pH-values.[13] These three different states of accumulation are assumed to be analogues to three distinct intermediates of the BR-WT photocycle, namely the O, the N and the M_2-intermediate, respectively.[13,22] A summary of the properties of the photocycle intermediates shown in Fig. 1 is given in Table 1. High resolution crystal structures of the variant BR-D85N at alkaline pH indeed revealed a tertiary structure which indicates an open cytoplasmic half-channel, as is expected for the M_2-state.[22,25] The freely suspended variant BR-D85T at alkaline pH has been imaged by cryo-SEM[11] exhibiting the postulated outward tilt of helix F and the resulting strong bending of the purple membrane (see Fig. 2). Because such alkaline-mediated deprotonation of the Schiff-base triggers the same conformational changes responsible for PM bending in the M_2-state the chosen BR-D85 variants BR-D85N and BR-D85T allow for the bending of purple membranes to be observed in thermal equilibrium. We thus investigated both BR-D85T and BR-D85N at alkaline pH using atomic force microscopy and single molecule force spectroscopy.

Table 1 Relation between the protonation state of key amino acids in bacteriorhodopsin and shape changes of the molecule.[3,4,12,22,23] From the cytoplasmic (CP) side to the extracellular (EC) side the moieties considered are aspartic acid 96 (D96), the Schiff-base linkage (SB), aspartic acid 85 (D85) and the proton release complex (PRC). Protonation is denoted by a '+', while deprotonation by a '−'. The related opening and closing of the cytoplasmic and extracellular half-channels are noted. The SB column also features the conformation of the retinylidene residue within the proton channel at the given intermediate

	CP	D96	SB		D85	PRC	EC
B	Closed	+	+	all-*trans*[a]	—	+	
J	Closed	+	+	13-*cis*[a] 14-s-*cis* 15-*anti* twisted[a]	—	+	
K	Closed	+	+	13-*cis*[a] 14-s-*cis*[a] 15-*anti* less twisted[a]	—	+	
L	Closed	+	+	13-*cis*[a] 14-s-*cis*[a] 15-*anti*[a]	—	+	
M_1	Closed	+	—	13-*cis* 14-s-*cis*[a] 15-*anti*[a]	+	+	
M_2	Open	+	—	13-*cis*[b] 14-s-*trans*[b] 15-*anti*[b]	+	+	
N	Open	—	+	13-*cis*[b] 14-s-*trans*[b] 15-*anti*[b]	+	—	Closed
O	Closed	+	+	all-*trans*[a]	+	—	Open

[a] Accessibility of the Schiff-base from the extracellular side. [b] Accessibility of the Schiff-base from the cytoplasmic side.

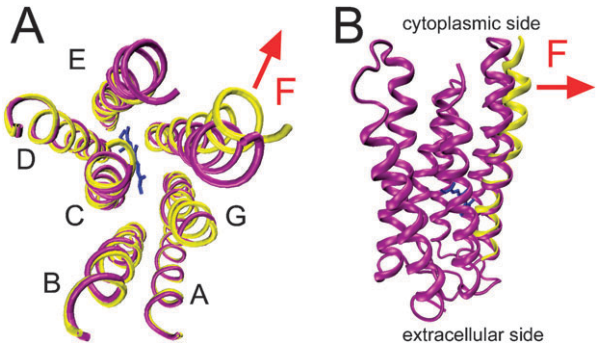

Fig. 2 Shape changes of bacteriorhodopsin. The outward tilt of helix F in the direction of the red arrow is linked to the opening of the cytoplasmic half-channel which alters the initial bacteriorhodopsin morphology (purple conformation) to become wedge shaped (yellow conformation). (A) View from the cytoplasmic side, looking down the proton path through the membrane. The retinylidene residue is shown in blue. Only the transmembrane helical domains are shown without the interlinking amino acid loops. (B) Side view looking from within the plane of the purple membrane highlighting the large-scale conformational change resulting in the wedge shape of BR in the M_2-state. Structural data[23] were obtained from PDB entries 1FBB and 1FBK. Structures were modeled using the program VMD.[24]

Materials and methods

Materials

Purple membranes from *Halobacterium salinarum* containing bacteriorhodopsin wild-type (BR-WT) and variants BR-D85N and BR-D85T were a gift from Dieter Oesterhelt's group at the Max-Planck Institute of Biochemistry, Martinsried, Germany. All purple membrane samples used were freshly prepared according to standard procedures[26] and finally purified by sucrose density gradient centrifugation.

Mica was purchased from Plano GmbH Wetzlar, Germany and freshly cleaved before sample preparation.

Sample preparation

Purple membrane stock solutions were diluted in a 150 mM KCl, 10 mM Tris-HCl, pH 8.2 buffer to a final absorbance

(OD) of 0.2 to 0.3 at 570 nm. 50 μL of imaging buffer (300 mM KCl, 10 mM Tris-HCl, pH 9.7 or 300 mM KCl, 10 mM HEPES, pH 7.0) was pipetted onto a 1 cm by 1 cm sized mica substrate and then 5 to 10 μL of the PM suspension was added. After 30 min of incubation, excess PM material was removed and the sample extensively rinsed with imaging buffer (10 times 20 μL). The samples were then mounted onto the microscope where they were allowed to stand for 30 min before imaging in order to reach thermal equilibrium.

Methods

Tapping-mode atomic force microscopy (TM-AFM) in liquid environment was chosen for imaging in order to minimize forces between AFM-tip and sample. Imaging was performed on a Nanoscope IV system (Veeco, Santa Barbara, CA). Pyramidal, oxide-sharpened Si_3N_4 tips attached to a V-shaped substrate (Olympus, Tokyo, Japan) were used for imaging. All images were measured using tapping-mode AFM with constant amplitude attenuation. The cantilever approach was performed with an initial drive amplitude of 250 mV (tip oscillation amplitude 1–2 V). Once the sample was approached both drive amplitude and setpoint were adjusted to minimal forces possible.

Single molecule force spectroscopy was utilized to differentiate between the cytoplasmic and the extracellular side of PMs by recording force spectra of the non-supported BRs. For this purpose the force spectroscopy experiments were done on the apex of convex membranes, where they are surrounded by buffer on both sides. The distance–force curves obtained depend on the unfolding pattern of the examined BRs and whether the pull-out of a single BR molecule is done from the cytoplasmic (=C-terminal) or the extracellular (=N-terminal) side. The respective α-helices of BR are unfolded pairwise as the protein is pulled out of the membrane[27] resulting in four main peaks. The respective number of amino acids between the peaks is different for pull-outs done from the cytoplasmic and the extracellular side. This allows for the determination from which side the BR was pulled out off the PM and thus a differentiation between both membrane sides. Peak positions and inter peak distances were determined according to the worm-like chain model (WLC).[28] All experiments were conducted at room temperature (21 °C).

Results and discussion

Aspartate in position 85 plays an important role in the photocycle of wildtype bacteriorhodopsin (BR-WT). During the transition from the L-state to the M_1-state, the Schiff base is deprotonated while D85 is protonated. In the essentially irreversible step from the M_1 to the M_2-state the orientation of the Schiff-base linkage is reversed from 13-*cis*, 14-s-*cis* to 13-*cis*, 14-s-*trans* and the cytoplasmic half-channel is opened to facilitate reprotonation of D96 from the cytoplasmic side. In BR-D85N and BR-D85T the pK_a-value of the Schiff base is reduced from >13 in non-illuminated BR-WT to 8–9 in BR-D85N/T variants.[29,30] At alkaline pH the Schiff base of the mutated BRs is thus deprotonated even in the non-illuminated state, resulting in the opening of the CP half-channel. Consequently, the BR-variant experiences the same changes with respect to its 3-D structure as BR-WT during its photocycle.[25] Helix F is tilted outward and the proteins become wedge-shaped. Due to the strong interaction within the PM crystalline lattice they cooperatively induce the macroscopic bending of the PMs.

AFM images of BR-D85T containing PMs taken at alkaline pH (Fig. 3A + B) show that many PMs appear to be bent at these physiological conditions. About 50% of the PMs on the mica appear as dome-like structures, the other 50% as flat structures. The height of typical bent PMs reaches up to a few hundred nanometres in alkaline medium. This shows that all PMs in the sample are curved. Those absorbed with the convex side up cause the dome-like structures, the other ones which absorb with their convex side down collapse, however, these will be discussed later. In comparison, at neutral pH almost all PMs are planar, as can be seen in Fig. 3C + D. Due to the aforementioned pH-dependent equilibrium of the three different states of accumulation very few bent purple membrane patches still remain at pH 7. These are only slightly bent and feature dome-like as well as collapsed structures.

Taking AFM images of freely suspended PMs in solution is not possible. AFM techniques always require a flat support on which the sample is more or less immobilized for investigation. The forces acting between the support (mica) and the membranes may influence the PMs morphology, however, the results reported here show that the interactions between mica and PM do not prevent membrane bending at the PM mica interface. This in turn means that the surface tension of the bent PMs is greater than the forces between the BR-D85X patches and the mica substrate.

As schematically shown in Fig. 4 the shape of the PMs changes in suspension from flat (Fig. 4A), *e.g.* at pH = 7, to that of a spherical segment (Fig. 4B). These segments come into contact with the mica substrate (Fig. 4C). Whereas the 'upwards' looking or concave membranes collapse the 'downward' looking, convex membranes interact only at their outer rim with the substrate. This causes the outer rim to appear somewhat flattened where attached to the substrate. In the middle, however, a dome-like part of the membrane remains (Fig. 4D). While arching over the mica surface the bent membrane parts are surrounded by buffer solution on both sides and are thus effectively 'freely suspended' just like in their truly native place, the *Halobacterium salinarum* cell.

Naturally, two ways of membrane adsorptions are observed. Whereas the 'downward' looking spheres change their shape only at the rim due to interaction with the substrate, the 'upward' looking spheres seem to collapse (Fig. 5) and only a small part of the rim rises above the substrate. Whereas 'downward' looking spheres are stabilized by the internal buffer, the 'upward' looking spheres come into contact with the substrate more or less at a single point. Beginning at this point and extending outward, the water between PM and the substrate is squeezed out as the membrane attaches to the surface until finally the entire membrane is flatly absorbed to the substrate. Only larger membranes and only at their outer rim, where the internal membrane tension is high enough, have a small part of their rim not in touch with the substrate (section 1 Fig. 5).

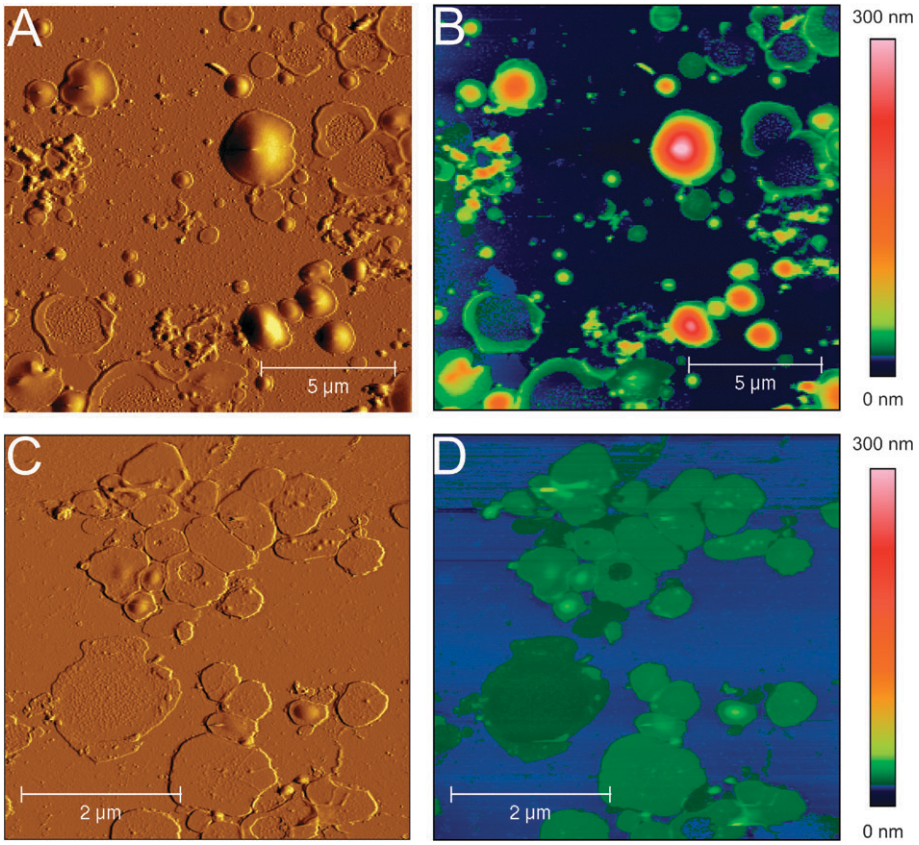

Fig. 3 Bending of purple membranes observed at physiological conditions. Tapping-mode AFM images of BR-D85T membranes (A + B) at alkaline pH (9.7) and (C + D) at neutral pH (7.0) on mica. A + C are amplitude, B + D the respective height images.

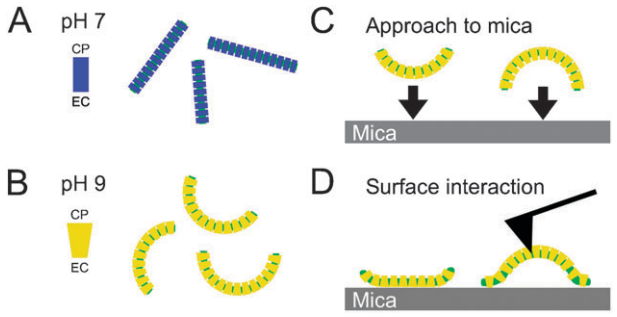

Fig. 4 Scheme of bending of purple membrane containing the variants BR-D85N or BR-D85T, respectively. (A) BR-D85N/T membranes in neutral suspension. (B) BR-D85N/T membranes in alkaline suspension. The cytoplasmic half-channel is open and the protein transforms to a wedged shape. (C) BR-D85N/T bent membranes adsorb on mica at alkaline pH. (D) In dependence on their orientation they either collapse (left) or form a dome-like structure (right). An AFM-tip is shown schematically to indicate that the force spectra are taken from BRs in a quasi-free suspended membrane where buffer is on both sides of the membrane. This resembles the situation in the halobacterial cell.

To determine experimentally whether the PMs do bend 'extracellular-side-out' or 'cytoplasmic-side-out' has not been achieved before. Attempts to reach molecular resolution in the middle of the dome-like PMs were not successful. The strong bending and even more the great flexibility of the effectively

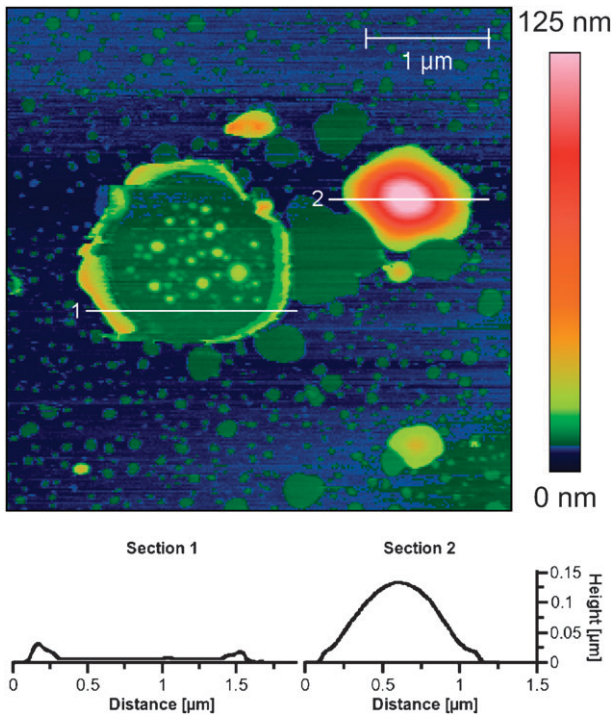

Fig. 5 Adsorption of bent purple membranes comprising BR-D85T at alkaline pH in dependence on their orientation. 'Upward' looking PM to the left with corresponding cross-section 1 and 'downward' looking PM with corresponding cross-section 2.

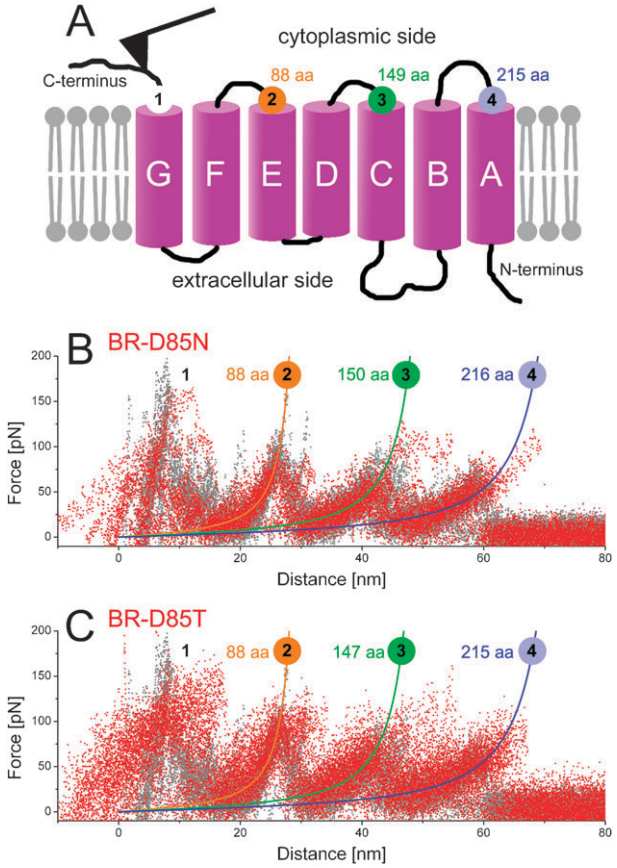

Fig. 6 Single molecule force spectroscopy of non-supported bacteriorhodopsins. The force spectra were taken from the center region of dome-like bent purple membranes where the bacteriorhodopsins are not in contact with the mica substrate. From the force spectra the orientation of the membranes was determined to show the cytoplasmic side up. (A) Schematic representation of the force spectroscopy experiments performed on BRs from the cytoplasmic side of PM. As the cantilever attached to the C-terminus is retracted the protein is pulled out of the membrane in four steps (numbered 1–4) unfolding pairwise the seven α-helices of BR. (B + C) Comparison of force curves taken from the cytoplasmic side of BR-WT (gray dots) and (B) the variant BR-D85N and (C) the variant BR-D85T (red dots), respectively, at alkaline pH.

free spanning convex membrane parts limits the achievable resolution of AFM techniques. Images of molecular resolution, to distinguish both sides, are only obtainable on totally flat and supported membranes and are thus inaccessible in this case. We took advantage of single molecule force spectroscopy to detect the orientation and direction of bending of the PMs investigated. The different types of distance–force curves obtained when analyzing an 'extracellular-side-out' or a 'cytoplasmic-side-out' bent PM reveal themselves to be a reliable tool for discrimination.

The peaks emerging in single molecule force spectroscopy of BR represent the pairwise unfolding of the α-helices of BR. In particular, this means the stretching of the C-terminus, the helices G&F, the helices E&D, and the helices C&B in case the AFM tip attached on the cytoplasmic side (see Fig. 6A). After the fourth peak the protein is pulled out of the membrane or detaches from the tip. If the extracellular side faces upward, the N-terminus could adhere to the tip. Again four main peaks occur. First, the N-terminus is stretched, then the helices A&B are unfolded and stretched, the third and the fourth peak represent the unfolding and stretching of the helices C&D and E&G, respectively. As the force curves measured on both sides of the PM are easily distinguishable by the difference in separation of the main peaks and by the difference in the relative forces of those peaks,[31] this technique is a reliable method to determine the orientation of the PM (Table 2). Since the exact position at which adhesion to the tip occurs is variable for both termini, all force curves are normalized on the second peak and only the remaining three peaks that do not represent the stretching of the termini are considered for side differentiation. Also, the AFM-tip does not specifically attach to either terminus but with low probability also to the interconnecting loops (numbers 2–4 in Fig. 6A). Thus the collected force spectra of BR-WT as well as the variants were screened and only force curves featuring four peaks and an overall length of more than 50 nm were selected for comparison purposes. Force curves with a length greater 50 nm only result from a pulling event from either terminus, but not a loop.

In Fig. 6B and C distance–force curves of BR-WT that we pulled from the cytoplasmic side are given in dark grey. The force curves we obtained from the dome-like shaped PMs at alkaline pH for BR-D85N (Fig. 6B) and BR-D85T (Fig. 6C) are shown in red. The three main peaks (numbered 2–4) associated with helix unfolding have the same separation for both variants relative to BR-WT (see Table 2). This leads to the conclusion that the force curves of both variants are taken from the cytoplasmic side of the membranes. Although the BR-D85T force curves have a higher variation than the BR-D85N curves, the peak distances of both variants match those of the cytoplasmic wildtype curves. Some side peaks and the maximum forces of the peaks seem to differ from BR-WT. This may be due in part to the effectively freely suspended nature of the convex membranes and due to the changed tertiary structure of the protein, which may result in altered intramolecular forces and thus altered unfolding pathways.

Due to their bent and freely suspended nature, convex membranes possess distinguishing features, such as their flexibility.

Table 2 Spacing of cytoplasmic and extracellular BR-WT and BR-D85N/T-peaks

	Peak 2	Peak 3	Peak 4	Number of curves	ΔPeak 3–2	ΔPeak 4–3
BR-WT cytoplasmic	88 (86) aa	149 (147) aa	215 (216) aa	22	61 aa	66 aa
BR-WT extracellular	(74) aa	(133) aa	(223) aa	12	59 aa	90 aa
BR-D85N Convex	88 aa	150 aa	216 aa	14	62 aa	66 aa
BR-D85T Convex	88 aa	147 aa	215 aa	17	59 aa	68 aa

aa = amino acid, for BR-WT literature values are given in parentheses.[31]

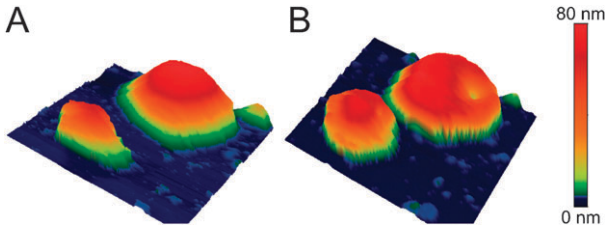

Fig. 7 Flexibility of bent purple membranes. Topography of BR-D85N membrane (A) prior to and (B) after force spectroscopy. Whereas the convex membrane in (A) is unaltered in (B) the irreversible damage and the resulting deformation of the membrane caused by the single molecule force spectroscopy process is evident. Both images are 1×1 μm in size.

If a force is applied to the surface of the membrane and BR protein moieties are extracted, the membrane is capable of giving in and by doing so compensate this force to a certain extent. This is, *e.g.*, evident on a percentage basis, as the number of successful events of pulling BR out of the PM is less for the variants than for the wildtype. As forces become too large, however, deformation or even damage to the membrane results. This is shown in Fig. 7 where a dome-like membrane was imaged prior to (Fig. 7A) and after (Fig. 7B) single molecule force spectroscopy. A small indentation marks the area where the membrane was destabilized during the force spectroscopy process.

The spherical shape of PM patches in solution changes when they come into contact with the mica substrate and at the rim a deformation is observed which arises from the interaction of BR and lipids with the mica substrate. The superposition of surface tension induced in the membrane from structural curvature and the interaction with the substrate leads to membrane shapes which may be described as Gaussian curves. In Fig. 8A and B cross-sections taken from different dome-like PMs of variant BR-D85T and BR-D85N have been approximated by a Gaussian fit, which fits nicely the obtained membrane topography (see ESI).† The 2nd derivative of the Gaussian profile, evaluated at the apex of the respective PM sections (f''_0), yields a characteristic curvature for both BR-D85 variants on mica. If plotted against the respective membrane size, represented by the area A underneath the membrane's cross-section, a characteristic cut-off size becomes evident, below which the PM and thus its curvature are significantly affected by surface interactions (Fig. 8C). Below this cut-off size surface interactions begin to dominate increasingly over the intramembrane tension and force the bent PM more and more into contact with the substrate surface. Beginning from the rim and extending toward the center of the PM, this increased surface interaction squeezes the dome-like freely suspended part together, resulting in an increased curvature as well as an enlarged rim area. This effect can be seen for smaller membranes, namely for the red, green and blue cross-sections, which are highlighted in the inserts of Fig. 8A and B. For BR-D85T the characteristic cut-off size is approximately 0.04 μm^2 or a diameter of about 1 μm. The mean curvature evaluated for membranes larger than these critical dimensions is -1.17 μm^{-1}. For BR-D85N, the respective values for cut-off size are approximately 0.06 μm^2 or a diameter of about

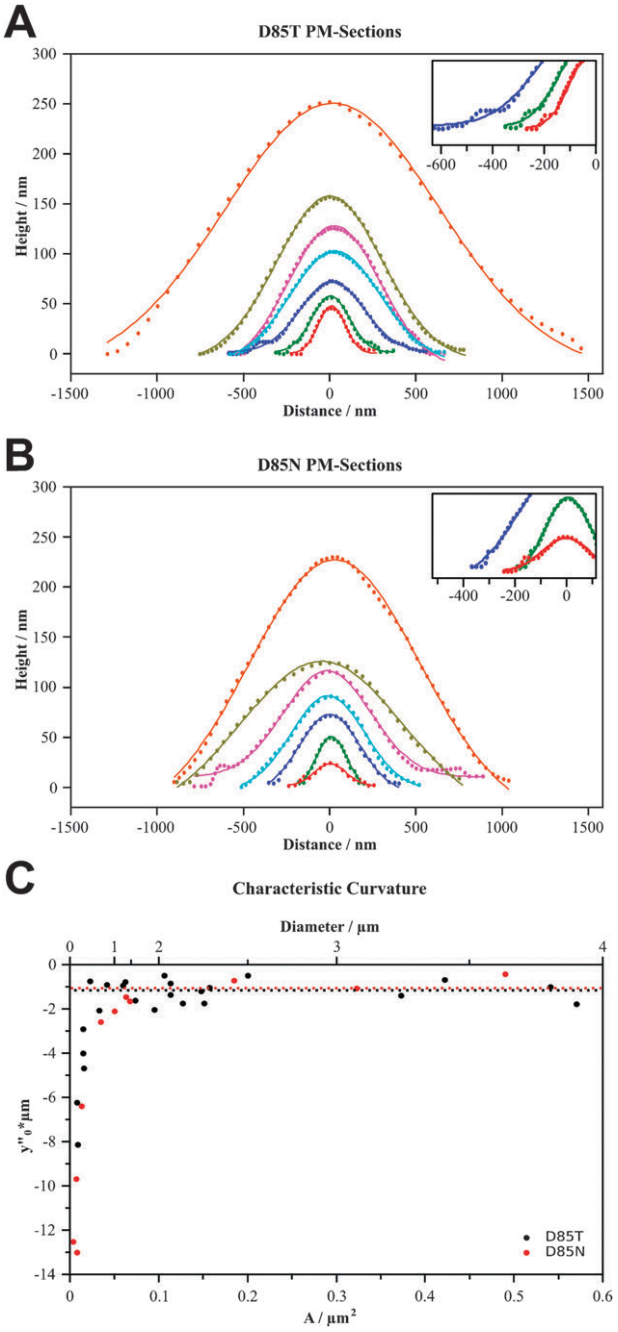

Fig. 8 Analysis of the shape of dome-like purple membranes containing BR-D85N and BR-D85T on mica. (A and B) Cross-sections of BR-D85T and BR-D85N membranes (dots) were approximated by a Gaussian profile (solid line), which fits nicely the experimental values (see ESI).† Several selected cross-sections and belonging fits with $R^2 > 0.99$ are shown. (C) Analysis of the curvature of purple membranes on mica. The membrane curvature (2nd derivative of the Gaussian profile evaluated at the apex of the respective PM sections) plotted against the size (area underneath the profile) of the respective dome-like membranes. BR-D85T exhibits a mean curvature $y''_{0,mean}$ of -1.17 μm^{-1} at PM sizes greater than 0.04 μm^2 or diameters greater than about 1 μm. Below these critical dimensions, membrane curvature is significantly affected by surface interactions. For BR-D85N the respective values are -1.06 μm^{-1} for the mean curvature of unaffected membranes and 0.06 μm^2 or a diameter of about 1.5 μm for the critical membrane dimensions.

1.5 μm. The mean curvature of uninfluenced membranes is $-1.06\ \mu m^{-1}$.

Conclusion

The bending of BR-D85N and BR-D85T membranes in alkaline buffer has been visualized by AFM for the first time. Analysis and differentiation of the bent sides was performed using single molecule force spectroscopy. The results confirm the model that M-state formation during the photocycle of BR causes an opening of the cytoplasmic half-channel which induces large scale bending of the membranes. From such dome-like formed PMs the first single molecule force spectra of BRs of non-supported PMs, *i.e.* where both sides of the PM are in contact with liquid, were obtained. The analysis of the macroscopic bending of the PMs revealed to be dominated by the characteristic curvature of PMs as long as they are larger in diameter than a certain cut-off size of about 1 μm. The topography of small membranes is fully controlled by their surface interaction, however, the shape of larger membranes in the inner part is primarily controlled by the characteristic shape of the individual BR molecules. The findings reported give rise to the hope that PMs might be used as chemo-mechanical transducers, which upon a pH-shift change their shape and thereby interact with their environment.

Acknowledgements

This work was financially supported through DFG grant HA 2906/4-3.

References

1 D. Oesterhelt and W. Stoeckenius, *Nat. New Biol.*, 1971, **233**, 149.
2 U. Haupts, J. Tittor and D. Oesterhelt, *Annu. Rev. Biophys. Biomol. Struct.*, 1999, **28**, 367.
3 J. K. Lanyi and G. Varo, *Israel. J. Chem.*, 1995, **35**, 365.
4 J. K. Lanyi, *Biochim. Biophys. Acta, Bioenerg.*, 2006, **1757**, 1012.
5 Y.-S. Lee and M. Krauss, *J. Am. Chem. Soc.*, 2004, **126**, 2225.
6 A.-N. Bondar, M. Elstner, S. Suhai, J. C. Smith and S. Fischer, *Structure*, 2004, **12**, 1281.
7 S. Subramaniam and R. Henderson, *Nature*, 2000, **406**, 653.
8 U. Haupts, J. Tittor, E. Bamberg and D. Oesterhelt, *Biochemistry*, 1997, **36**, 2.
9 J. Czege and L. Rheinisch, *Acta Biochim. Biophys. Hung.*, 1987, **22**, 463.
10 Porschke, *J. Mol. Biol.*, 2003, **331**, 667.
11 D. Rhinow and N. A. Hampp, *J. Phys. Chem. B*, 2008, **112**, 13116.
12 J. K. Lanyi, *Annu. Rev. Physiol.*, 2004, **66**, 665.
13 G. J. Turner, L. J. W. Miercke, T. E. Thorgeirsson, D. S. Kliger, M. C. Betlach and R. M. Stroud, *Biochemistry*, 1993, **32**, 1332.
14 H. Okumura, M. Murakami and T. Kouyama, *J. Mol. Biol.*, 2005, **351**, 481.
15 G. Varo and J. K. Lanyi, *Biochemistry*, 1991, **30**, 5008.
16 B. Schobert, L. S. Brown and J. K. Lanyi, *J. Mol. Biol.*, 2003, **330**, 553.
17 S. Subramaniam and R. Henderson, *Biochim. Biophys. Acta, Bioenerg.*, 2000, **1460**, 157.
18 A. Miller and D. Oesterhelt, *Biochim. Biophys. Acta, Bioenerg.*, 1990, **1020**, 57.
19 N. A. Hampp and D. Zeisel, *IEEE Eng. Med. Biol. Mag.*, 1994, **13**, 67.
20 A. Seitz and N. A. Hampp, *J. Phys. Chem. B*, 2000, **104**, 7183.
21 N. A. Hampp, *Chem. Rev.*, 2000, **100**, 1755.
22 S. Rouhani, J.-P. Cartailler, M. T. Facciotti, P. Walian, R. Needleman, J. K. Lanyi, R. M. Glaeser and H. Luecke, *J. Mol. Biol.*, 2001, **313**, 615.
23 S. Subramaniam, M. Lindahl, P. Bullough, A. R. Faruqi, J. Tittor, D. Oesterhelt, L. Brown, J. K. Lanyi and R. Henderson, *J. Mol. Biol.*, 1999, **287**, 145.
24 W. Humphrey, A. Dalke and K. Schulten, *J. Mol. Graphics*, 1996, **14**, 33.
25 L. S. Brown, H. Kamikubo, L. Zimanyi, M. Kataoka, F. Tokunaga, P. Verdegem, J. Lugtenburg and J. K. Lanyi, *Proc. Natl. Acad. Sci. U. S. A.*, 1997, **94**, 5040.
26 D. Oesterhelt and W. Stoeckenius, *Methods Enzymol.*, 1974, **31**, 667.
27 F. Oesterhelt, D. Oesterhelt, M. Pfeiffer, A. Engel, H. E. Gaub and D. J. Müller, *Science*, 2000, **288**, 143.
28 A. Janshoff, M. Neitzert, Y. Oberdörfer and H. Fuchs, *Angew. Chem.*, 2000, **112**, 3346.
29 J. Tittor, D. Oesterhelt and E. Bamberg, *Biophys. Chem.*, 1995, **56**, 153.
30 J. Tittor, U. Haupts, C. Haupts, D. Oesterhelt, A. Becker and E. Bamberg, *J. Mol. Biol.*, 1997, **271**, 405.
31 M. Kessler and E. H. Gaub, *Structure*, 2006, **14**, 521.

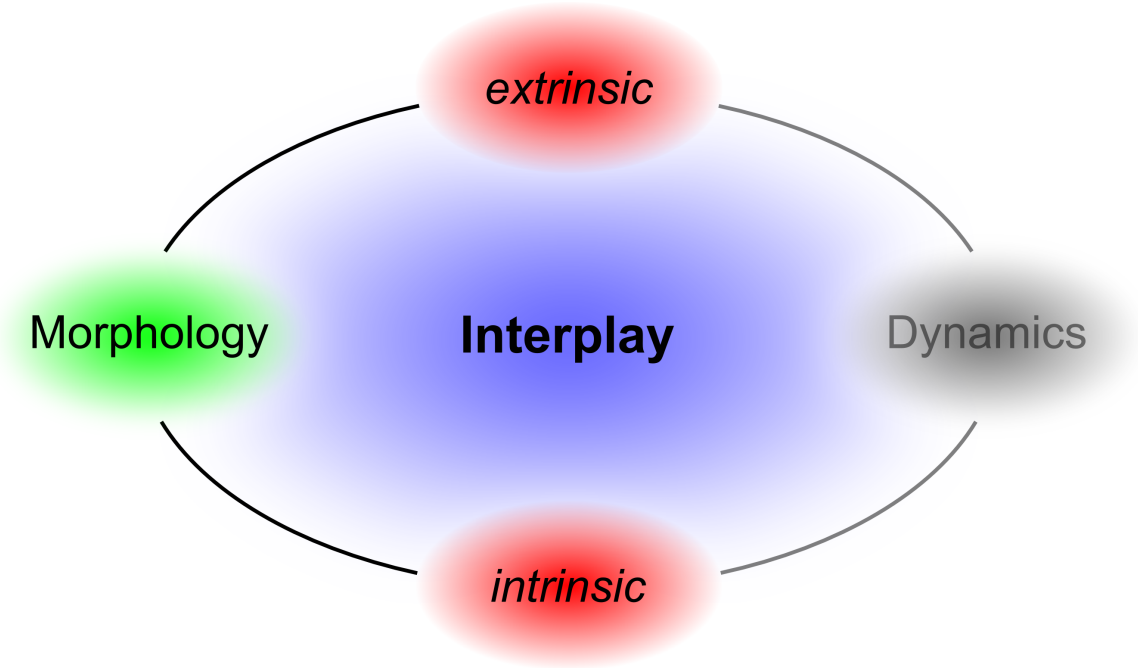

A DYNAMICS OF BACTERIORHODOPSIN IN SOLID-SUPPORTED PURPLE MEMBRANES STUDIED WITH TAPPING-MODE ATOMIC FORCE MICROSCOPY.
Schranz, M. and Baumann, R.-P.; Rhinow, D.; Hampp, N.
J. Phys. Chem. B, **2010**, *114*, 9047-9053.

B CRYSTALLINITY OF PURPLE MEMBRANES COMPRISING THE CHLORIDE-PUMPING BACTERIORHODOPSIN VARIANT D85T AND ITS MODULATION BY PH AND SALINITY
Rhinow, D.; Chizhik, I.; Baumann, R.-P.; Noll, F.; Hampp, N.
J. Phys. Chem. B, **2010**, *114*, 15424-15428.

C BENDING OF PURPLE MEMBRANES IN DEPENDENCE ON THE PH ANALYZED BY AFM AND SINGLE MOLECULE FORCE SPECTROSCOPY
Baumann, R.-P.; Schranz, M.; Hampp, N.
PCCP, **2010**, *12*, 4329-4335.

D PH-DEPENDENT BENDING IN AND OUT OF PURPLE MEMBRANES COMPRISING BR-D85T
Baumann, R.-P.; Eussner, J; Hampp, N.
submitted to PCCP

Journal Name

Dynamic Article Links ►

Cite this: DOI: 10.1039/c0xx00000x

www.rsc.org/xxxxxx

ARTICLE TYPE

pH-Dependent Bending In and Out of Purple Membranes Comprising BR-D85T

R.-P. Baumann,*[a] J. Eussner[a] and N. Hampp [ab]

Received (in XXX, XXX) Xth XXXXXXXXX 20XX, Accepted Xth XXXXXXXXX 20XX

DOI: 10.1039/b000000x

The light-driven proton pump bacteriorhodopsin (BR) embedded in purple membrane (PM) from *Halobacterium salinarum* undergoes a series of conformational changes while transporting a proton from the cytoplasmic to the extracellular side over the course of the so-called photocycle. Wild-type BR variant D85T, where aspartic acid 85 is replaced by threonine, allows for the study of structural intermediates of this photocycle, that are formed in a light-dependent manner in the wild-type and in thermal equilibrium by tuning the pH of the D85T purple membrane suspension. Especially the last and least studied O-photocycle intermediate of bacteriorhodopsin has caught recent attention. First AFM images of the O-photocycle intermediate at physiological conditions revealing strongly bent purple membranes are presented. Bacteriorhodopsins embedded therein were analyzed by single molecule force spectroscopy (SMFS) providing the first single molecule force spectra of BR in the O-intermediate. SMFS was further employed to determine the absolute sign of membrane curvature. Complementary electrostatic force microscopy (EFM) was performed to support PM side discrimination and determination of bending direction. Bending of PM-D85T was analyzed in more detail providing further insight into the structure-function relationship of the bacteriorhodopsin proton pump as well as PM behaviour at the solid-liquid junction. Findings reported here are of general interest to the field of chemomechanical transducers.

Introduction

Purple membrane (PM) from *Halobacterium salinarum* featuring the light-driven proton pump bacteriorhodopsin (BR) and lipids only[1-3] is expressed by the archaeon under anaerobic conditions to allow for the harvesting of energy via photosynthesis. Structurally, PMs are 2D crystalline patches comprising BR trimers arranged in a hexagonal lattice within the lipid bilayer. A prototype of seven transmembrane α-helical proteins, BR, allows for a light-driven proton transport from the cytoplasmic (CP) to the extracellular (EC) side of the cell membrane.[4-9] Retinal connected to lysine 216 and utilized as a chromophore by BR divides the ion-channel into two halves and provides for a vectorial transport mechanism.[10] Certain point mutations of bacteriorhodopsin, however, do allow a bidirectional transport and are not limited to protons but convey ions as well.[11,12] The basic underlying principle of function in either case is the same[13] and consists of a sequence of isomerisation states of the retinylidene residue intertwined with a well-studied series of protonation changes of key amino acids within both half channels and the Schiff-base (SB) linkage (ion transport).[10,14,15] Concomitantly, certain conformational changes within the structure of BR switch the Schiff-base accessibility to either cytoplasmic or extracellular.[10,16,17] This isomerization/switch/transfer (IST) model provides a general concept for ion translocation by halobacterial retinal proteins and formally describes the catalytic cycle of bacteriorhodopsin in terms of six such steps.[2,14] Photo-isomerization of retinal from all-*trans* to a 13-*cis* configuration is followed by a proton transfer from the Schiff-base the proton acceptor D85 in the extracellular half. An outward tilt in helix F causes the opening of the cytoplasmic channel, which coincides with a switch in Schiff-base accessibility from the extracellular to the cytoplasmic half to allow for a vectorial transport mechanism. While reprotonation of the Schiff-base from D96 in the cytoplasmic channel occurs, the proton release complex (PRC) on the extracellular half releases a proton to the bulk phase. Finally, retinal reisomerizes thermally, switching accessibility of the Schiff-base back to extracellular once D96 is reprotonated from the CP surface. This switch is accompanied by the closing of the CP and the opening of the EC half channel. Notably the IST model also accounts for transport modes of bacteriorhodopsin variants[12,18], halorhodopsin[19] and sensory rhodopsin.[20] Macroscopically speaking, these transient intermolecular and related morphological changes of BR result in a light- and pH-induced bending of PM over the course of this so called photocycle.[21,22]

The genetically modified BR variants of type BR-D85X, where X is a neutral residue, are of particular interest with respect to PM bending, because protonation of residue 85 is the critical step in the bacteriorhodopsin wild-type (BR-WT) transport cycle. Here we focus on BR-D85T, where the primary proton acceptor aspartic acid 85 is replaced by threonine which, as a result, not

only converts BR into a chloride pump[11, 12] but also allows for the pH-controlled accumulation of BR-D85T in any one of three spectroscopically distinct intermediates of the BR-WT photocycle: with increasing pH these are the O, the N and the M intermediate, which may be associated with different shape changes of the protein.[23,24] BR-D85T thus allows for various bent states of purple membranes to be observed in thermal equilibrium and under physiological conditions. The alkaline M state, which is the first of the aforementioned three to be encountered in the BR photocycle, has been the focus of recent investigations.[21,22] In the M_2-state the key amino acids D96, D85 and the proton release complex (PRC) are all protonated, while the cytoplasmic accessible Schiff-base in its 13-*cis*-14-s-*trans*-15-*anti* conformation is not. Helix F is tilted outward and the cytoplasmic half-channel is open, resulting in a strong bending of PM. Single molecule force spectroscopy revealed, that the convex side of bent PMs under alkaline conditions corresponds to the cytoplasmic, while the concave side corresponds to the extracellular side.[22] Over the course of the M_2 over N to O transition D96 transfers its proton to the Schiff-base and is itself reprotonated, while D85 remains unchanged and the PRC releases a proton to the extracellular medium. The cytoplasmic half-channel closes while the extracellular half opens, as the Schiff-base changes its shape to a twisted all-*trans* conformation and its accessibility back to the EC side. The now arrived O state should also feature bent purple membranes according to crystal structures which suggest that large scale conformational changes take place on the extracellular side of the protein[25] leading to a geometrical asymmetry accompanied by the formation of wedge-shaped BRs. The asymmetry should be amplified through the PM crystal by the high protein-to-lipid ratio resulting in a macroscopic bending of PM. Unlike the M state, however, where conformational changes are restricted to the cytoplasmic side, PM in the O state should now be bent in the opposite direction, that is the extracellular side should be convex and the cytoplasmic side concave. At acidic pH BR-D85T closely resembles the O intermediate of the BR-WT photocycle, which shares structural similarities with acid blue membrane. We thus investigated BR-D85T at acidic pH using atomic force microscopy and single molecule force spectroscopy.

Materials and methods

Purple Membranes from *Halobacterium salinarum* containing bacteriorhodopsin wild-type and variant BR-D85T were a gift from Dieter Oesterhelt's group at the Max-Planck Institute of Biochemistry, Martinsried, Germany. All purple membrane samples used were freshly prepared according to standard procedures[26] and finally purified by sucrose density gradient centrifugation.

Mica was purchased from Plano GmbH Wetzlar, Germany and freshly cleaved prior to sample and template stripped gold (TSG) preparation.

Sample preparation

Purple membrane stock solutions were diluted in a 150 mM KCl, 10 mM citrate, pH 3.5 buffer to a final absorbance (OD) of 0.2 to 0.3 at 570 nm. 50 µL of imaging buffer (300 mM KCl, 10 mM citrate, pH 3.5) was pipetted together with 5 to 10 µL of the PM suspension onto a 1 cm by 1 cm sized mica or TSG substrate. After 15-30 min of incubation, excess PM material was removed and the sample extensively rinsed with imaging buffer (10 times 20 µL). The samples were then mounted onto the microscope sample stage, where they were allowed to stand for another 30 min prior to imaging in order to reach thermal equilibrium.

Methods

Tapping-mode atomic force microscopy (TM-AFM) was chosen for imaging in order to minimize interaction forces, especially sheer, between tip and sample. Imaging was performed in liquid, to mimic physiological conditions, on a Nanoscope IV system (Veeco, Santa Barbara, CA). Pyramidal, oxide-sharpend Si_3N_4 tips attached to a V-shaped substrate (Olympus, k = 0.08 N/m, f_0 = 24-44 kHz, Tokyo, Japan) were used for imaging. All images were measured using TM-AFM with constant amplitude attenuation. The cantilever approach was performed with an initial drive amplitude of 250 mV (tip oscillation amplitude 1-2 V). Once the tip had engaged both drive amplitude and setpoint were adjusted to minimal forces possible.

Single molecule force spectroscopy on the apex of convex purple membranes was utilized to differentiate between the cytoplasmic and the extracellular side by recording force-distance curves of the non-supported BRs.[22] Force spectra of BR generally feature four main peaks, which, however, differ in distance of separation and relative force. These characteristics of the force spectra are specific and unique to a given PM side and thus allow for a reliable side discrimination and determination of orientation.[27] For analysis only force curves featuring all four main peaks and an overall length greater than 60 nm were selected. The spectra singled out for analysis were aligned on the second peak and only the last three main peaks were considered for side differentiation. Peak positions and inter peak distances were determined according to the worm-like chain model (WLC).[28]

EFM measurements were conducted in air using SCM-PIT tips (antimony (n) doped Si, k = 1-5 N/m, f_0 = 70-83 kHz, 0.01-0.025 Ω/cm, Veeco, Santa Barbara, CA, USA) utilizing the Nanoscope's LiftMode feature. This mode of surface potential detection is a two-pass procedure in which the surface topography is obtained by standard tapping mode in the first pass, and the surface potential is measured on the second pass. Just before the second pass, the tip is moved to a configurable lift height above the sample surface. On the second pass of each line, the tip is then moved at a constant height, tracing the topography that was recorded in the first pass. The two measurements are thus interleaved, that is, they are each measured one line at a time.

All AFM experiments were conducted at room temperature (21 °C).

Results and discussion

We analysed PM-D85T on mica in particular at acidic pH by tapping-mode atomic force microscopy. For comparison purposes complementary imaging was also performed at neutral and alkaline conditions. Fig. 1 shows strongly bent as well as flatly collapsed purple membranes in acidic environment (Fig. 1 A) confirming *in situ*, that PM-D85T past the N intermediate, which features a flat topography (Fig. 1 B), is indeed bent again in the

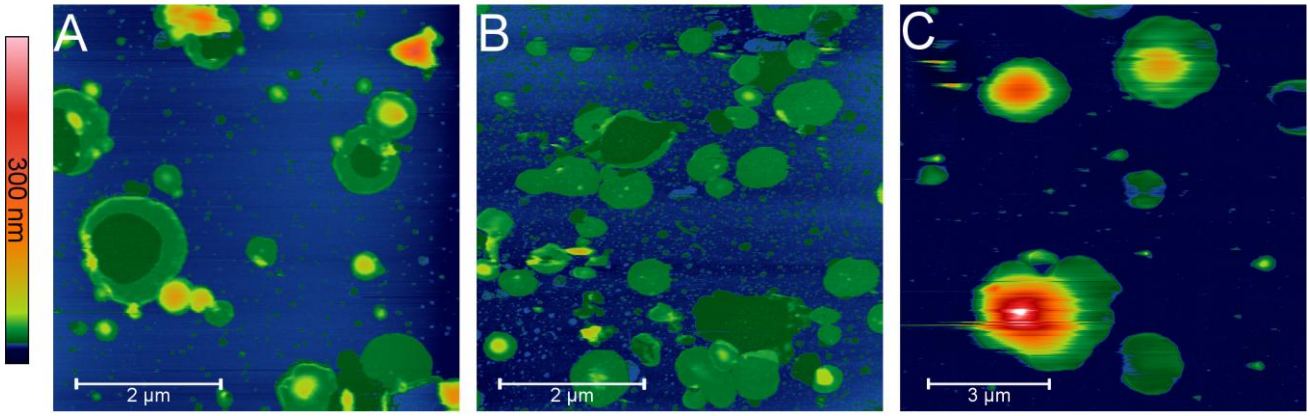

Fig. 1 pH-dependent bending of PM-D85T observed on mica via TM-AFM in liquid under A) acidic conditions (pH = 3.4), B) neutral conditions (pH = 7.0) and C) basic conditions (pH = 9.7). Wedge-shaped BRs causing strong macroscopic bending of PM lead to flatly collapsed as well as dome-like structures under both acidic and basic conditions. At neutral pH PM-D85T features a mostly flat, disk-like morphology.

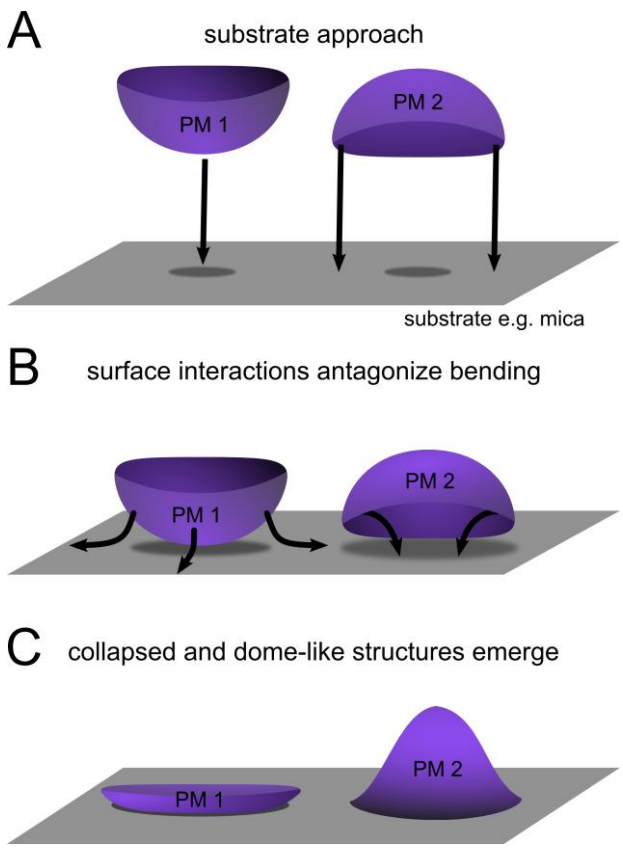

Fig. 2 Formation of collapsed and dome-like PM structures. A) Bent PM-D85T may approach the substrate surface either from the convex side apex first (left column: PM 1) or from the concave side rim first (right column: PM 2). B) In both cases strong surface interactions which antagonize the bending arise, pulling the membranes down onto the substrate surface (arrows). C) However, in the case of PM 1 membranes are pulled onto the substrate surface from the apex outward resulting in flat and collapsed structures. In case of PM 2 the rim flatly adsorbs to the substrate, but water trapped inside prevents further collapse causing dome-like structures.

O intermediate, sharing morphological similarities with the alkaline M state (Fig. 1C). The formation of collapsed and dome-like structures is illustrated based on Fig. 2. As the bent purple membranes approach the mica substrate they may do so with either the cytoplasmic or extracellular side, naturally two ways of membrane absorption are observed. In the first case, which corresponds to about half of the imaged PMs, the bent membranes approach the mica surface with their convex side facing down. As the membrane comes into contact attractive interactions arise, which antagonize the bending. Beginning from the point of first contact outward, buffer solution between PM and the substrate is expelled and the membrane almost fully collapses onto the mica substrate. A small but elevated rim is all that remains to hint at their bent nature (Fig. 2 left column). In the second case, which corresponds to the other half of PMs, the membranes are bent towards the surface and unlike the former case not the middle but the rim approaches the mica substrate first. Once again attractive interactions arise, but this time the water between PM and mica is trapped preventing a further approach and collapse resulting in a dome-like structure with a flat rim (Fig. 2 right column).

Fig. 1 A featuring the same height scale as C shows, that although the height of these typically bent and effectively freely suspended purple membranes in acidic environment reaches up to a few hundred nanometers, they generally fall short of heights measured on the same substrate under alkaline conditions for a given membrane size. This suggests that under acidic conditions PMs are bent less strongly than at alkaline conditions.

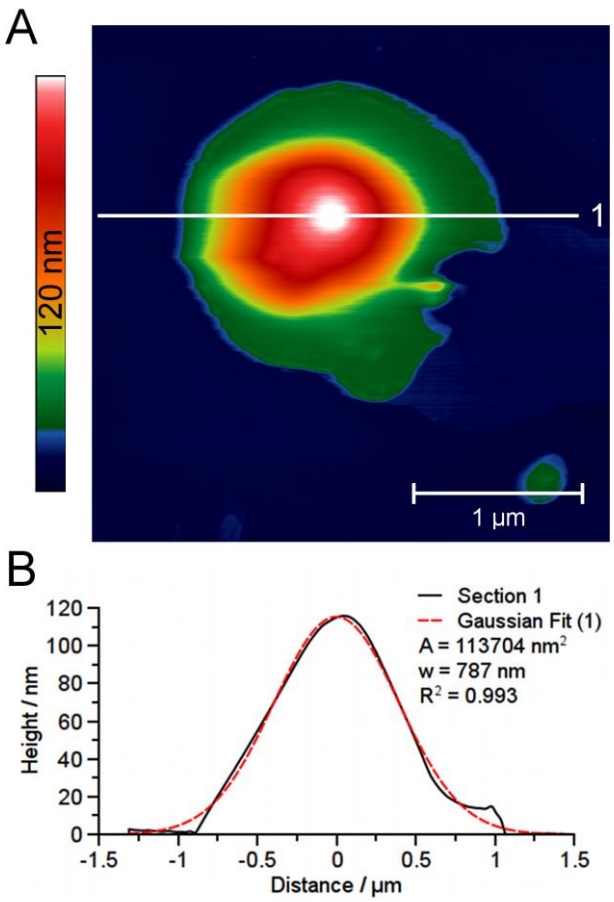

$$y = y_0 + \frac{A}{w \cdot \sqrt{\frac{\pi}{2}}} \cdot e^{\left(-2 \cdot \left(\frac{x - x_c}{w}\right)^2\right)} \quad (1)$$

$$y'' = -\frac{4A}{w^3 \cdot \sqrt{\frac{\pi}{2}}}, \quad x = x_c = 0 \quad (2)$$

Fig. 3 Analysis of membrane bending. A) TM-AFM image of PM-D85T acquired in liquid at acidic pH with cross-section through the apex of the strongly bent membrane. B) Approximating the extracted profiles by Gaussian fits according to (1) allows for the curvature of the respective membrane to be determined, by evaluating the second derivative (2) of the Gaussian at the apex.

Membrane bending may be analysed in more detail by approximating cross-sections through dome-like PMs by Gaussian fits (Fig. 3). A superposition of surface tension induced by BR curvature and substrate interactions is responsible for the transformation of spherical PM patches into dome-like structures upon substrate adsorption. According to Fig. 3 B these membrane shapes may be well described by Gaussian curves. At the apex of the dome-like structures purple membrane is not in contact with the substrate but surrounded by buffer on both sides just like in its native occurence, the *Halobacterium salinarum* cell. Further, due to geometric considerations any remaining substrate effects should cancel out at the apex and membrane topography and curvature should be controlled by the characteristic shape of the individual BR molecules. The 2nd derivative at the apex of the Gaussian profile obtained yields a curvature which is

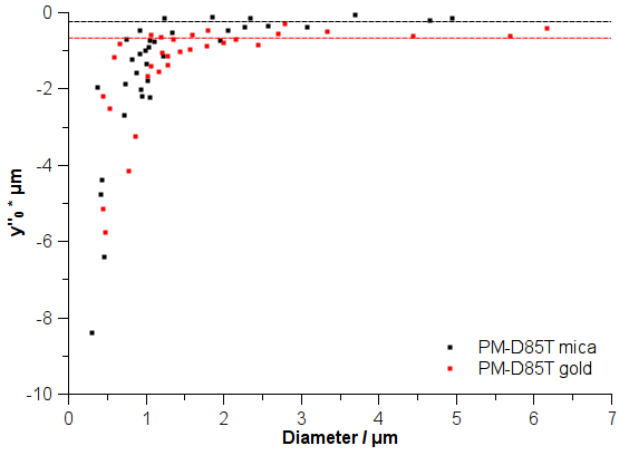

Fig. 4 Characteristic curvature of PM-D85T evaluated under acidic conditions on various substrates. Membranes with a mean diameter of less than about 1.5 µm are strongly affected by the substrate while larger membranes feature a characteristic curvature of $y''_{0,mean}$ = -0.25 µm^{-1} (mica), which is significantly less than observed under basic conditions ($y''_{0,mean}$ = -1.17 µm^{-1}). On gold, where surface interactions are decreased, PMs retain a more pronounced bending and characteristic curvature of $y''_{0,mean}$ = -0.68 µm^{-1}.

characteristic for the given purple membrane and the physicochemical conditions. If plotted against the membrane's size (Fig. 4), however, a cut-off diameter emerges, below which membranes are strongly affected by the surface and their morphology is governed by surface interactions. According to Fig. 4, this cut-off diameter is in the range of 1.0 to 1.5 µm. Above this cut-off PM-D85T at and around the apex of the dome is not directly affected by surface interactions but only controlled by the characteristic shape of the individual BR molecules and thus resembles the truly native state of BR-D85T and PM-D85T for the given conditions. The characteristic curvature of such membranes on mica is $y''_{0,mean}$ = -0.25 µm^{-1} with a standard deviation of 0.16 µm^{-1}, compared to $y''_{0,mean}$ = -1.17 µm^{-1} under basic conditions.[22] PM-D85T under acidic conditions is thus indeed less bent than in basic environment, which implies that the shape of individual BR molecules is different in both cases. For characteristic curvature determination the curvature of all membranes larger than the cut-off size was considered and the mean and standard deviation for the selected data were calculated. Interestingly a quite similar yet in its significant aspects slightly different picture develops for PM-D85T on a gold substrate under otherwise identical conditions. As shown in Fig. 4 data collected on both gold and mica substrates seems to complement each other at first. The characteristic curvature, however, reveals that purple membranes of variant D85T on gold are bent more strongly with a mean curvature of -0.68 µm^{-1} and a standard deviation of 0.21 µm^{-1}. Dome-like membranes are pulled downwards by attractive PM-surface interactions according to Fig. 2. In small PMs (smaller than the cut-off size) these forces outweigh antagonizing forces associated with membrane bending and as a result smaller PMs are thus squeezed together from the rim towards the center and appear strongly bent. In the case of larger PMs the squeezing along the rim becomes less significant for membrane topography. Surface interactions rather cause a

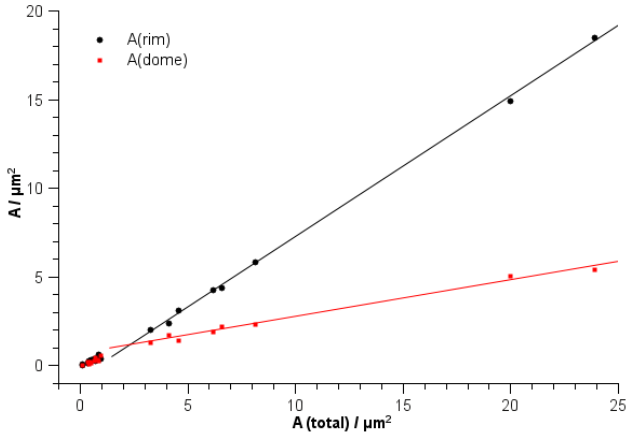

Fig. 5 Respective surface areas of the dome and rim part of bent PM-D85T plotted against the total PM area. Linear regression reveals a membrane size (2.35 µm2 or 1.73 µm diameter) above which rim and dome surface areas diverge as larger purple membranes exhibit a constant, characteristic curvature.

spreading out and seem to have a flattening effect on PMs, resulting in less and eventually characteristically bent dome-like structures, where a balance between extrinsic and intrinsic interaction forces is reached. As template stripped gold features a greater mean roughness and thus fewer contact points than mica, substrate-PM interactions are lessened allowing for stronger PM bending. As a result smaller membranes, still affected by the surface, become less squeezed than on mica while larger membranes are less spread out and flattened and retain a slightly larger characteristic bending. While providing a possible answer, this explanation does not conclusively resolve the issue, since membrane topography at the apex of large purple membranes should primarily be controlled by the characteristic shape of the individual BR molecules as the substrate surface and consequent interactions become irrelevant at this point. It is known from previous experiments that substrate induced dynamical processes within PM may influence membrane morphology on a large scale.[29] Disregarded thus far such dynamical processes might influence membrane bending as well and provide another possible explanation for the observed discrepancy, which however should not be overrated given the derived standard deviations. In light of this we feel the observed deviation is noteworthy, but needs further investigation on more substrates, which is part of ongoing research. In order to fully resolve this discrepancy between characteristic curvature on mica and gold theoretical modelling and computer simulations may be required. Nevertheless PM-D85T under acidic conditions is bent less strongly than under alkaline conditions irrespective of the substrate surface.

Interactions with the substrate give rise to a certain rim formation around the dome-like PM structures. Consequently, there exists a ratio between membrane area attributed to the rim and area attributed to the dome for every given membrane size. Since the curvature of the dome area changes with membrane size the relative areas of the rim and the dome of bent purple membranes should also change especially once the membrane reaches its constant characteristic curvature. As depicted in Fig. 5, this is evidently the case. By plotting the relative areas of rim and dome

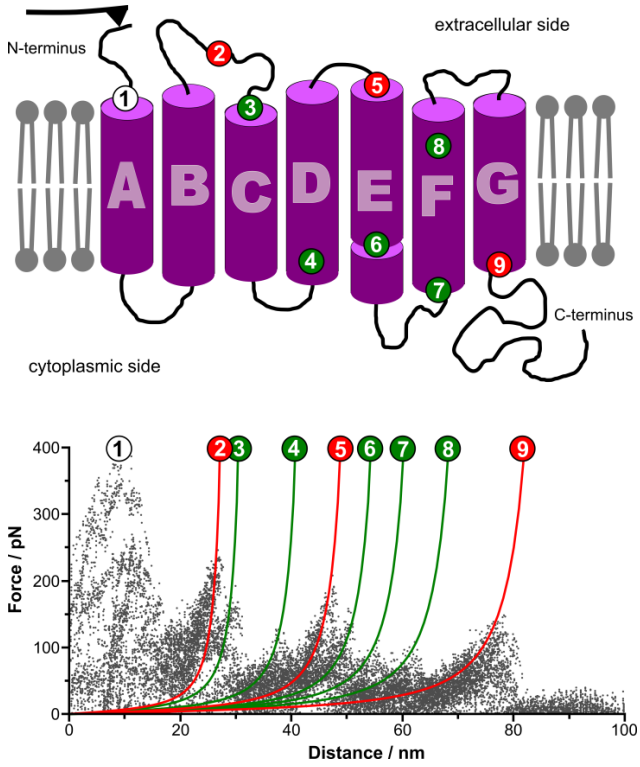

Fig. 6 Single Molecular Force Spectroscopy at the apex of dome-like bent purple membranes on mica reveals that PM-D85T is bent extracellular side out under acidic conditions. Maxima observed in collected force-distance curves nicely agree with the characteristic potential barriers encountered within BR pulled and unfolded from the N-terminus i.e. the extracellular side (see also Table 1). Main peaks indicating secondary structural motives are highlighted white and red, while sidepeaks hinting at characteristic features of the protein sequence and the present tertiary structure are marked green.

against the total area of PM it becomes clear, that the respective areas of rim and dome begin to diverge strongly once a certain membrane size is reached. This point, which happens to be the cut-off point, may be calculated as the point of intersection of the linear regression of both relative rim and dome area for larger membranes. An area of 2.35 µm^2 was calculated for PM on mica, which results in a cut-off membrane diameter of about 1.73 µm, which is slightly larger than determined from Fig. 4.

Despite being less bent PM-D85T still exhibits great flexibility under acidic conditions, rendering attempts to reach molecular resolution for side differentiation in the middle of dome-like PMs futile. Single molecular force spectroscopy, however, was successfully applied to discriminate both sides and determine the direction of bending. Fig. 6 shows force spectra taken from the center region of dome-like bent purple membranes, where bacteriorhodopsins are not in contact with the mica substrate and are said to reside in their native state. Beside the four main peaks a total of five side-peaks could be clearly identified. Specific characteristics of both variant and wild-type force spectra i.e. peak position and separation of the main peaks are given in Table 1 and are in exceptional agreement leading to the conclusion, that PM-D85T is bent extracellular side out. Therefore the extracellular side of bacteriorhodopsin monomers must assume an open form under acidic conditions leading to wedge-shaped

Table 1 Peak positions and separation between main peaks observed for force spectra of BR-D85T under acidic conditions in comparison to BR-WT literature values for single molecule force spectroscopy from the cytoplasmic and extracellular side. Peak positions are given in amino acids into the bacteriorhodopsin sequence. Not only the main but also the side peaks observed for BR-D85T are in excellent agreement with BR-WT analyzed from the extracellular side. PM-D85T is thus bent extracellular side out in acidic environment.

	BR-WT cytoplasmic[a]	BR-WT extracellular[a]	BR-D85T convex
Peak 2 (main)	**86**	**74**	**74**
Peak 3(side)	-	83	84
Peak 4 (side)	-	111	111
Peak 5 (main)	**147**	**133**	**133**
Peak 6 (side)	-	148	147
Peak 7 (side)	-	164	165
Peak 8 (side)	-	187	187
Peak 9 (main)	**216**	**223**	**224**
Δ Peak 5-2	**61**	**59**	**59**
Δ Peak 9-5	**66**	**90**	**91**

[a] literature values.[27]

Table 2 pH-dependent character and properties of PMs comprising BR-D85X

	acidic	neutral	alkaline
photocycle intermediate	O	N	M_2
BR morphology	bent	flat	bent
cytoplasmic side / extracellular side	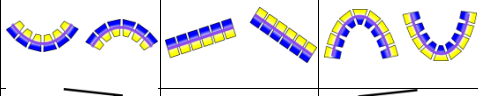		
appearance on substrate	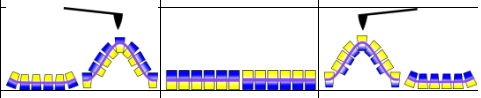		
characteristic curvature	-0.25 μm^{-1}	--	1.17 μm^{-1}
cut-off-size	1.73 µm	--	1.0 µm

BRs. Since characteristic curvature of purple membranes under acidic conditions is less than in basic environment single BRs are consequently less wedge-shaped implying that the extracellular half-channel is opened less widely in the O-state than the cytoplasmic half-channel is in the M_2-state providing further insights into the structure function relationship of the bacteriorhodopsin proton pump. The propagation of this wedge-shaped structural motive throughout the membrane results in a similar, yet less pronounced macroscopic bending of PM as already observed under basic conditions. This result is consistent with experimental as well as theoretical studies of the O-state of purple membrane. Table 2 briefly summarizes the results obtained from TM-AFM and single molecule force spectroscopy and compares and contrasts the O, N and M intermediate as represented by D85X. Interestingly force spectra of the variant show a number of prominent side peaks that are more frequently observed than in the wild-type reference spectra (data not shown). These occur at 84 amino acids (aa) (peak 3), 111 aa (peak 4), 147 aa (peak 6), 165 aa (peak 7) and 187 aa (peak 8) into the amino acid sequence of bacteriorhodopsin (Fig. 6). All but the first of these energy barriers are located in helices D, E, and F, which undergo significant conformational changes upon tilting into the O-state, as their extracellular terminal ends move outward from the center of the trimeric structure. Crystal structures of closely related acid blue PM revealed that the most prominent change in the cytoplasmic half of the protein with respect to these helices occurs at Glu166, which coincides with peak 7. Further Gly155 near the C-terminal end of helix E (close to peak 6) and Pro186 in helix F serve as swivel points for respective helix tilting. Proline 186, corresponding to barrier 8, also serves as hinge residue for the opening of the cytoplasmic side of the protein under alkaline conditions and thus serves an important double function within the protein. Peak 3, like peak 2, corresponds to a barrier located on the extracellular side in the B-C loop. Both barriers are also found in wild-type BR and could be indicative of a preserved β-sheet structure for the B-C loop in the O-state as has been suggested by theoretical modelling[30] and EPR measurements.[31] A significant difference between the spectra recorded for BR-D85T and BR-WT is the observed continuous decrease in force required to pull the various structural elements out of the membrane. For wild-type BR the rupture force of the last barrier (9) rises significantly again with respect to the other main peaks. A possible explanation for the adverse trend in BR-D85T might be the bent nature of PM. In the O-state helix G is moved significantly to the intermonomer location dramatically decreasing interactions with the remaining local environment especially once all other helices have been pulled out of the membrane. The observed potential barriers combined with the knowledge of the tertiary structure and morphology of PM illustrate the connection between mechanical stability and the characteristic features of a protein sequence as well as their implication on function in general.

We complemented single molecular force spectroscopy analysis with electrostatic force microscopy (EFM) as a means for PM side differentiation. According to their surface charge, both sides of PM may be attributed to either the less negatively charged cytoplasmic or the more negatively charged extracellular side, both differing in charge by about 20 mV on mica.[32] EFM is a two-pass interleaved line-by-line procedure where the topography of a sample is acquired by regular TM-AFM in the first pass, while the surface' potential is probed in the second. Although an absolute assessment of the electrostatic field distribution is not possible in the setup used due to the insulating nature of the mica substrate, relative estimations can still be performed with high accuracy. Fig. 7 shows such an EFM measurement of PM-D85T on mica in air incubated under both acidic and basic conditions. As a result of the drying process, purple membrane surface interactions seem to be weakened and internal membrane tension responsible for the strong bending prevails. A few small, flat and

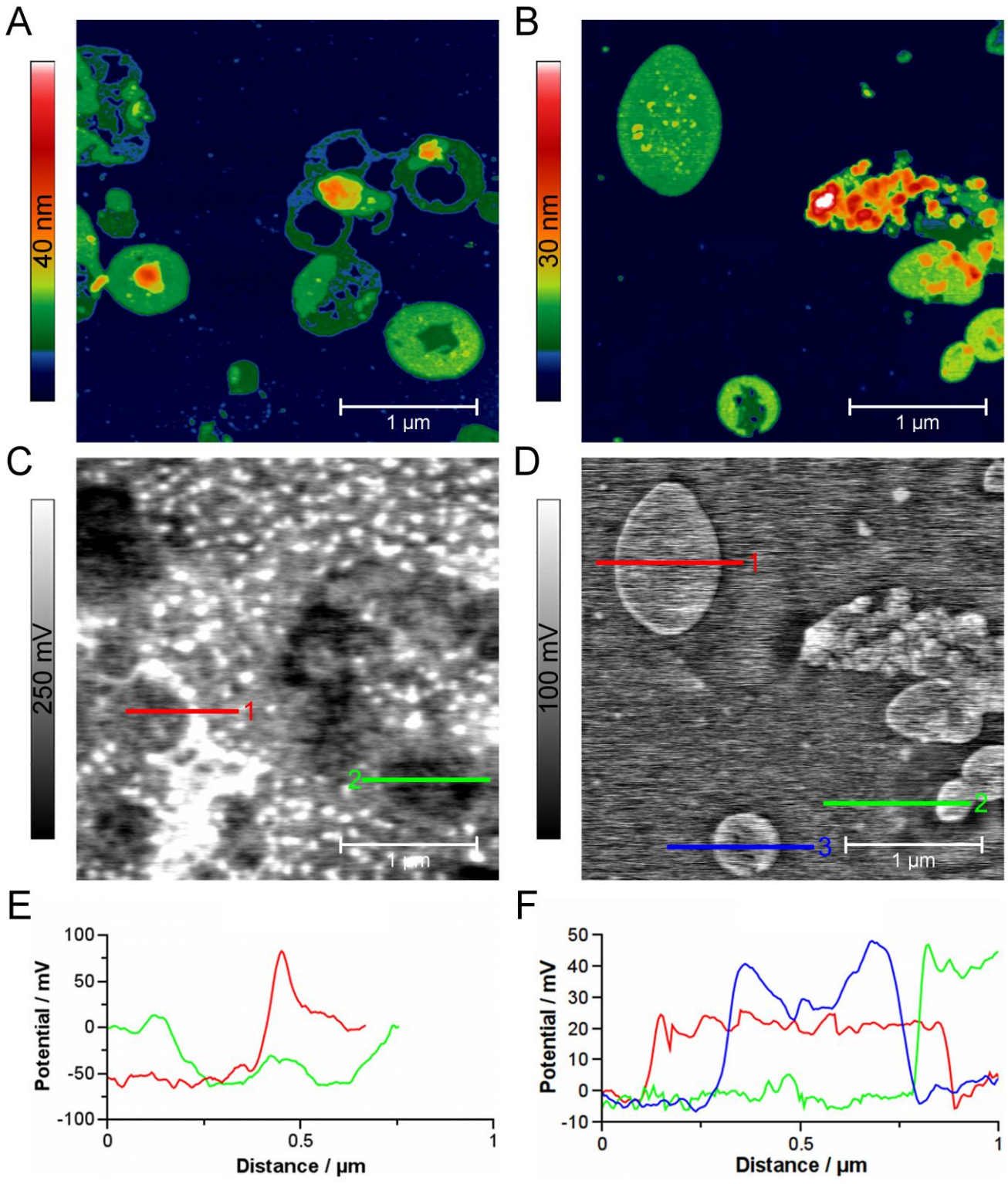

Fig. 7 Complementary EFM measurements for side discrimination of PM-D85T incubated under acidic (left: A, C, E) and basic conditions (right: B, D, F). Height images obtained in air (A,B) show flatly adsorbed, due to the drying process partially delaminated and a few remaining bent PM patches. Corresponding potential images (C, D) and sections (E, F) reveal the orientations and bending direction of respective membranes. Less negative membranes face CP side up, while more negative ones face EC side up. Apparently PMs are oppositely bent under acidic (EC out) and basic conditions (CP out). Notably, concave PMs (acidic: section 2, basic: section 3) feature both sides in EFM measurements due to their strongly bent nature.

collapsed membranes are thus able to partially detach from the surface again and roll up inwards to form inverted dome-like structures. In the bottom right corner of Fig 7A and in the bottom left and right corner of Fig. 7B such PM patches are shown. Larger membranes experiencing stronger surface interactions over a larger contact area are unable to detach and remain flatly absorbed on the mica substrate, some being delaminated in part, and others featuring fissures, both direct results of the drying process. It is also noteworthy that the vast majority of still adsorbed PMs are of the flat collapsed type and almost no regular dome-like structures remain after the drying process. This applies to both acidic and basic conditions and might be due to the fact, that they are only loosely attached to the mica substrate along their rim and otherwise completely surrounded by buffer solution on both sides. Since it is energetically unfavourable to expose one entire hydrophilic membrane side to the nascent air/water interface, especially if PM surface interactions are further weakened by the trapped water, they readily come off upon drying and are washed away by the receding buffer. The potential image (Fig. 7 C, D) reveals the surface potential of the respective membranes from the height image as well as their orientation. Interestingly the inverted dome-like PM-D85T just discussed feature two different potentials (see corresponding sections). In the alkaline case PMs exhibit a less negative potential along the upward bent rim attributed to the CP side and a more negative one inside its rolled-up structure corresponding to the EC side, while in the acidic case the rim is more negative (EC side) and the inside more positive (CP side). In either case both purple membrane sides differ by about 20 mV with respect to their surface potential. These findings underline the strongly bent nature of PM-D85T and are in unison with literature.

Conclusion

The O-state of wild-type bacteriorhodopsin represented by PM-D85T in acidic environment was visualized for the first time by means of TM-AFM. Similar to the M-state strongly bent purple membranes were observed. Single molecule force spectroscopy on the apex of dome-like PM structures was employed to discriminate between the cytoplasmic and extracellular side and confirm that in the O-state the extracellular half-channel is opened and consequently PM-D85T is bent extracellular side out. Further, the observed potential barriers combined with the knowledge of the tertiary structure and morphology of PM nicely illustrate the connection between mechanical stability and the characteristic features of a protein sequence as well as their implication on function in general. Side differentiation was successfully complemented by EFM measurements in air revealing concave membranes that detach from the surface and roll up. Further analysis of the macroscopic bending showed that PM-D85T is bent less strongly under acidic conditions featuring a less negative characteristic curvature. This implies that the opening of the extracellular half-channel is less pronounced than the opening of the cytoplasmic in the M-state and provides further insight into the structure function relationship of the bacteriorhodopsin proton pump.

Acknowledgements

We thank Nina Schromczyk for purification of PM-D85T. This work was financially supported through Deutsche Forschungsgemeinde (DFG) grant HA 2906/4-3

Notes and references

[a] *Philipps-University of Marburg, Department of Chemistry,Hans-Meerwein-Str. Bldg. H, D-35032 Marburg, Germany. Fax: +49 6421 2825798; Tel: +49 6421 2825775; E-mail: hampp@staff.uni-marburg.de*
[b] *Material Science Center, D-35032 Marburg, Germany*

1 D. Oesterhelt, W. Stoeckenius, *Nat. New Biol.* 1971, **233**, 149.
2 U. Haupts, J. Tittor, D. Oesterhelt, *Annu. Rev. Biophys. Biomol. Struct.* 1999, **28**, 367.
3 M. P. Krebs, T. A. Isenbarger, *Biochimica et Biophysica Acta* 2000, **1460**, 15.
4 N. Grigorieff, T. A. Ceska, J. K. H. Downing, M.Baldwin, R. Henderson, *J. Mol. Biol.* 1996, **259**, 393.
5 Y. Kimura, D. G. Vassylyev, A. Miyazawa, A. Kidera, M. Matsushima, K. Mitsuoka, K. Murata, T. Hirai, Y. Fujiyoshi, *Nature* 1997, **389** (6647), 206.
6 L.-O. Essen, R. Siegert, W. D. Lehmann, D. Oesterhelt, *Proc. Natl. Acad. Sci. USA* 1998, **95**, 11673.
7 H. Luecke, B. Schobert, H.-T. Richter, J.-P. Cartailler, J. K. Lanyi, *J. Mol. Biol.* 1999, **291**, 899.
8 H. J. Sass, G. Büldt, R. Gessenich, D. Hehn, D. Neff, R. Schlesinger, J. Berendzen, P. Ormos, *Nature* 2000, **406**, 649.
9 A.-N. Bondar, M. Elstner, S. Suhai, J. C. Smith, S. Fischer, *Structure* 2004, **12**, 1281.
10 S. Subramaniam, R. Henderson, *Nature* 2000, **406**, 653.
11 J. Sasaki, L. Brown, Y.-S. Chon, H. Kandori, A. Maede, R. Needleman, J. Lanyi, *Science* 1995, **269** (5220), 73.
12 J. Tittor, U. Haupts, C. Haupts, D. Oesterhelt, A. Becker, E. Bamberg, *J. Mol. Biol.* 1997, **271**, 405.
13 M. Kolbe, H. Besir, L.-O. Essen, D. Oesterhelt, *Science* 2000, **288** (5470), 1390.
14 U. Haupts, J. Tittor, E. Bamberg, D. Oesterhelt, *Biochemistry* 1997, **36**, 2.
15 J. K. Lanyi, *Annu. Rev. Physiol.* 2004, **66**, 665.
16 S. Subramaniam, R. Henderson, *Biochimica et Biophysica Acta* 2000, **1460**,157.
17 D. Porschke, *J. Mol. Biol.* 2003, **331**, 667.
18 J. Tittor, U. Schweiger, D. Oesterhelt, E. Bamberg, *Biophys. J.* 1994, **67**, 1682.
19 E. Bamberg, J. Tittor, D. Oesterhelt, *Proc. Nat. Acad. Sci. USA* 1993, **90**, 639-643.
20 R. Bogomolni, W. Stoeckenius, I. Szundi, E. Perozo, K. D. Olson, J. L.Spudich, *Proc. Nat. Acad. Sci. USA* 1994, **91**, 10188-10192.
21 D. Rhinow, N. A. Hampp, J. *Phys. Chem. B.* 2008, **112** (41), 13116.
22 R.-P. Baumann, M. Schranz, N. Hampp, *Physical Chemistry Chemical Physics* 2010, **12**, 4329.
23 G. J. Turner, L. J. W. Miercke, T. E. Thorgeirsson, D. S. Kliger, M. C. Betlach, R. M. Stroud, *Biochemistry* 1993, **32** (5), 1332.
24 H. Okumura, M. Murakami, T. Kouyama, *J. Mol. Biol.* 2005, **351**, 481.
25 S. Rouhani, J.-P. Cartailler, M. T. Facciotti, P. Walian, R. Needleman, J. K. Lanyi, R. M. Glaeser, H. Luecke, *J. Mol. Biol.* 2001, **313**, 615.
26 D. Oesterhelt, W. Stoeckenius, *Methods Enzym.* 1974, **31**, 667.
27 M. Kessler, E. H. Glaub, *Structure* 2006, **14**, 521.
28 A. Janshoff M. Neitzert, Y. Oberdörfer, H. Fuchs, *Angew. Chem.* 2000, **112**, 3346.
29 M. Schranz, R.-P. Baumann, D. Rhinow, N. Hampp, *J. Phys. Chem. B* 2010, **114**, 9047-9053.
30 H. C. Watanabe, T. Ishikura, T. Yamato, Structure, Function, *Bioinformatics* 2009, **75** (1), 53.
31 D. Chen, J. M. Wang, J. K. Lanyi, *J. Mol. Biol.* 2007, **366**, 790-805.
32 H. F. Knapp, P. Mesquida, A. Stemmer, *Surface and Interface Analysis* 2002, **33** (2), 108.

Addendum

PHOTOCHEMISTRY OF COUMARIN-FUNCTIONALIZED SiO_2 NANOPARTICLES.
KEHRLOESSER, D.; BAUMANN, R.-P.; KIM, H.-C.; HAMPP, N.
Langmuir, **2011**, *27*, 4149-4155.

Langmuir

ARTICLE

pubs.acs.org/Langmuir

Photochemistry of Coumarin-Functionalized SiO_2 Nanoparticles

Daniel Kehrloesser,[†] Roelf-Peter Baumann,[†] Hee-Cheol Kim,[†] and Norbert Hampp*[,†,‡]

[†]Faculty of Chemistry and [‡]Materials Sciences Center, University of Marburg, Hans-Meerwein-Strasse, Building H, D-35032 Marburg, Germany

ABSTRACT: We describe the synthesis and photochemistry of coumarin-functionalized silica nanoparticles, which were prepared utilizing 7-[3-(triethoxysilyl)propanyloxy]coumarin (TPC) to attach coumarin as a photoactive group to the silica nanoparticle surface. The nanoparticle size and morphology were investigated by scanning electron microscopy, atomic force microscopy, and dynamic light scattering. The diameter of the spherical nanoparticles was determined by all three methods to be about 40 nm. The surface functionalization was characterized in the bulk by ζ-potential measurements and on the single-nanoparticle level by electrostatic force microscopy, where the difference in surface potential between TPC-modified and unmodified silica nanoparticles is measured. The degree of surface functionalization was determined by thermogravimetric analysis (TGA), and a theoretical limit of about 23 000 coumarin entities per nanoparticle was calculated. The photochemistry, and its reversibility, of the nanoparticle-attached coumarin entities was found to be quite different from the coumarin photochemistry in solution or on flat surfaces. Photodimerization with light of 355 nm and photocleavage with light of 254, 266, and 280 nm were analyzed by absorption and fluorescence spectroscopy. Following several cycles of photodimerization and photocleavage showed that the absorption change at 320 nm decreases from cycle to cycle. The coumarin layer on the nanoparticles was proven to be unchanged by TGA. The apparent loss of absorption change is due to the formation of interlinked nanoparticles during the dimerization−cleavage cycles. Because the coumarin groups on the inside of the obtained nanoparticle clusters are inaccessible to light, the amount of "uncleavable" dicoumarins increases, thus lowering the obtainable absorption change from cycle to cycle.

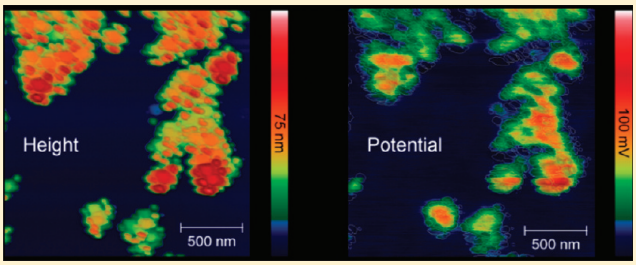

INTRODUCTION

The reversible photodimerization of two coumarin molecules under formation of a cyclobutane ring, resulting from a [2π+2π]-cycloaddition, was first disclosed by Ciamician and Silber[1] in 1902. Since then, an enormous number of studies concerning coumarin and its 7-alkoxy derivatives have been published due to the unique photochemistry of these molecules. In most cases solutions[2−5] have been studied, but there are also publications on the photochemical behavior in crystals,[6−8] polymer matrixes such as thin films,[9,10] and even self-assembled monolayers (SAMs).[11−13] Light having a wavelength longer than 300 nm causes photodimerization of coumarin and its derivatives, forming four possible stereoisomers: *syn* or *anti* head-to-head (hh) and *syn* or *anti* head-to-tail (ht) (Scheme 1). Photocleavage is observed upon irradiation with light of wavelengths shorter than 300 nm.

In 1968, Stoeber et al. described a simple method to synthesize highly monodispers silica nanoparticles of various diameters,[14] inducing a lot of researchers to further investigate the functionalization of the surface. The use of such nanoparticles in various fields was explored, e.g., biological applications[15−17] and catalysis and materials chemistry.[18−22] Due to the easy and flexible surface modification, their nonacute toxicity, and the fact that they can easily penetrate cell membranes, silica nanoparticles are promising candidates for drug and gene delivery.[23−25]

In 1998, Imai et al. reported the synthesis of an interpenetrating polymer network hybrid structure consisting of poly(2-methyl-2-oxazoline), having coumarin moieties as side groups, and tetramethoxysilane and investigated the resulting polymer properties, such as the glass transition point and solvent resistance of photochemically cross-linked polymer films.[26] Two years later, Graf et al. described the functionalization of silica nanoparticles with coumarin 343 and investigated the formation of particle clusters due to photochemical dimerization.[27] In 2003, Mal et al. combined the photochemical properties of coumarin with silicon-based nanotechnology by modifying the mesoporous silica cavity MCM-41 with coumarin. They showed that it is possible to control the uptake, storage, and release of organic molecules in MCM-41 by photocontrolled dimerization and cleavage of coumarin groups.[28] In the same year, Fujiwara et al. published the synthesis of pentacyclo[9.5.1.1^{3,9}.1^{5,15}1^{7,13}]octasiloxane bearing eight coumarin groups. They investigated the formation of polymeric organic−inorganic hybrid materials by photodimerization of concentrated solutions of the octasiloxane and compared this to the intramolecular dimerization of coumarin groups in diluted solutions.[29] Three years later, Zhao et al. synthesized photodeformable spherical hybrid nanoparticles consisting of coumarin dimers. These particles "melted away" when irradiated with hard UV light.[30] Just recently, Ha et al. came up with biocompatible fluorescent silica nanoparticles utilizing the fluorescence of coumarin derivatives.[31]

Received: January 19, 2011
Revised: February 18, 2011
Published: March 14, 2011

Scheme 1. Isomers of Dimers of 3-(Triethoxysilyl)propanyloxy-Derivatized 7-Hydroxycoumarin

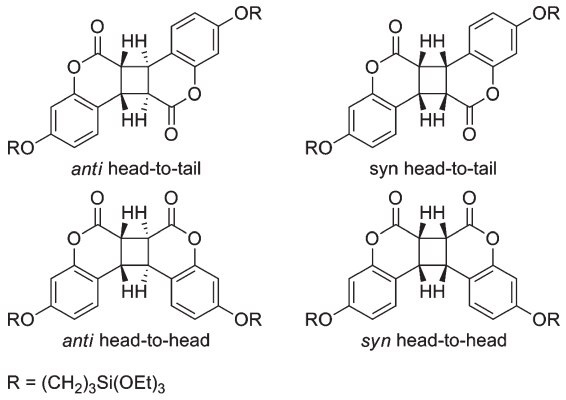

In this paper we report on the photochemistry of coumarin-functionalized silica nanoparticles. The SiO_2 nanoparticles (NPs) were functionalized with 7-[[3-(triethoxysilyl)propyl]oxy]coumarin (TPC) as shown in Scheme 2. We studied the surface morphology, size distribution, and surface potential of the TPC-functionalized nanoparticles by scanning electron microscopy (SEM), atomic force microscopy (AFM), and electrostatic force microscopy (EFM). We show that it is possible to differentiate between nonfunctionalized and functionalized particles on the single-nanoparticle level by measuring their surface potential with EFM. This work describes in detail the photochemistry of coumarin anchored on the surface of a solid silica core. In contrast to the work of Zhao et al., where prior to particle formation coumarin was dimerized to form particles that consist completely of coumarin dimer moieties, which can only be cleaved upon irradiation with UV light but not be redimerized, we investigated the reversible photodimerization and photocleavage of coumarin groups on the particle surface. We found that the photochemistry of the coumarin groups anchored to the convex surface of the nanoparticles differs significantly from the photochemistry of identical groups in solution or attached to a flat silicon surface.[13] Whereas the quantum yield of the photocleavage of the coumarin dimers is identical on both surfaces within the experimental limits, the reversibility of the process is quite different. Photochemical dimerization occurs mainly between coumarin groups located on the same particle shell and is reversible, in contrast to the work of Graf et al., who found a significant size dependency on the irradiation time in particular for high particle concentrations. In our experiments this effect needs to be considered only after several cycles of photodimerization and photocleavage.

EXPERIMENTAL SECTION

Materials and Sample Preparation. Ethanol (absolute) and acetonitrile (HPLC grade) were purchased from Carl Roth GmbH, and methanol (HPLC grade) was purchased from Fisher Scientific. Ammonium hydroxide solution (25 wt %) and tetraethyl orthosilicate (TEOS) were purchased from Sigma-Aldrich and used as received. TPC was synthesized from 7-hydroxycoumarin following literature procedures.[28,32]

Synthesis of 7-[3-(Triethoxysilyl)propanyloxy]coumarin-Functionalized Silica Nanoparticles (TPC-NPs). The synthesis follows mainly the modified Stoeber synthesis for organosilica spheres reported by van Blaaderen et al.[14,33] In the first step 3.64 mL of ammonium hydroxide solution was added to a solution of 3.58 mL of TEOS in 93 mL of ethanol and the resulting solution stirred for 20 h. Then 700 mg of TPC was added to 25 mL of this solution and the resulting solution again stirred for 20 h. Afterward the surface-functionalized particles were sedimented using screwed 50 mL FEP Oak Ridge tubes in a Sorvall Super T21 (Thermo Fisher Scientific) equipped with an SL50T rotor running at 18 000 rpm (38 724 rcf) at 4 °C. The supernatant was discarded, and the particles were dispersed in methanol. For further purification this process was repeated 10 times until the supernatant was coumarin free. After evaporation of the solvent the nanoparticles were dried in vacuum.

Characterization of Silica Nanoparticles. UV−vis spectra were measured with a Lambda 35 spectrometer (Perkin-Elmer) between 190 and 600 nm with 480 nm·min^{-1} in steps of 1.0 nm. Fluorescence spectroscopy was performed on a Shimadzu RF-1502 spectrometer. Thermogravimetric analysis (TGA) was performed on a TGA/SDTA 851^e system (Mettler Toledo) in an open corundum crucible between 25 and 1000 °C in a nitrogen atmosphere with a heating rate of 10 K·min^{-1}. Dynamic light scattering (DLS) measurements were accomplished with a Zetasizer Nano ZS (Malvern). The ζ potential was measured with a Delsa Nano C (Beckmann Coulter). Particles were measured in the reaction solution diluted 1:5 with ethanol in a standard flow cell. Field-emission SEM imaging was performed on a JSM-7500F (Jeol) with a YAG-BSE detector (Autrata). A 20 μL portion of a 0.01 mg·mL^{-1} dispersion of the particles was evaporated at room temperature and normal pressure on isolating silicon wafers as substrates. Samples were sputtered with platinum and transferred via an ALTO-2500 liquid nitrogen (LN_2) cryotransfer system (Gatan) and measured in high vacuum. Surface structure imaging was realized using an atomic force microscope, Nanoscope IV (Veeco Metrology). All measurements were carried out in tapping mode with pyramidal, oxide-sharpened Si_3N_4 tips in air at ambient conditions.

Photochemistry. As a light source for triggering the photochemical dimerization of coumarin groups, an AVIA 355-7 laser (Coherent) was used. The laser system is a diode-pumped, Q-switched, frequency-tripled Nd:YAG laser operating at a wavelength of 355 nm having a pulse length of 25 ns. Irradiation was accomplished with a repetition rate of 10 kHz and a pulse energy of 260 μJ/pulse. The beam profile was widened to a diameter of 1.2 cm. Photocleavage was induced with a Shimadzu RF-1502 spectrometer using excitation wavelengths of 280, 266, and 254 nm. The light energy was determined by using azobenzene as an actinometer following Gauglitz and Hubig.[34]

RESULTS AND DISCUSSION

Studies on Morphology and Functionalization of TPC-NPs. SEM images of SiO_2 NPs were used to characterize the morphology of the nanoparticles. Figure 1 a shows the nonfunctionalized nanoparticles. They are slightly agglomerated spherical particles with a diameter of about 40 nm. This agrees well with the results from DLS where an average diameter of 39.3 ± 9.6 nm with a polydispersity index of 0.036 was derived. In Figure 1 b−d the TPC-functionalized SiO_2 NPs are shown at different magnifications. The TPC functionalization slightly enhances their tendency to agglomerate (b), but they still have a spherical shape. Their diameter is now about 45 nm, which DLS measurements of the TPC-functionalized SiO_2 NPs confirm. An average diameter of 45.6 ± 15.0 nm with a polydispersity of 0.181 is derived. The length of one fully extended TPC molecule is 1.35 nm. This should result in an increase in diameter of 2.7 nm, i.e., from 39.3 to 42 nm. However, both SEM and DLS measurements indicate an increase in diameter of about twice as much, which could possibly be explained by the formation of some type of a "bilayer" of TPC on the nanoparticle surface. Parts c and d of

Scheme 2. Synthesis and Photochemistry of TPC-NPs

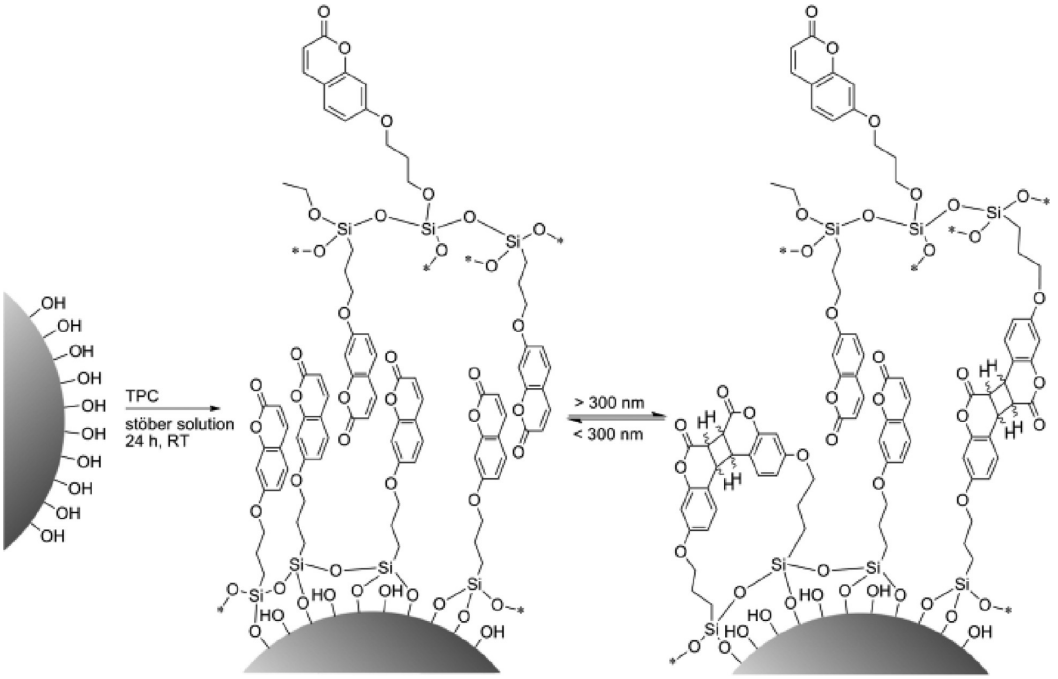

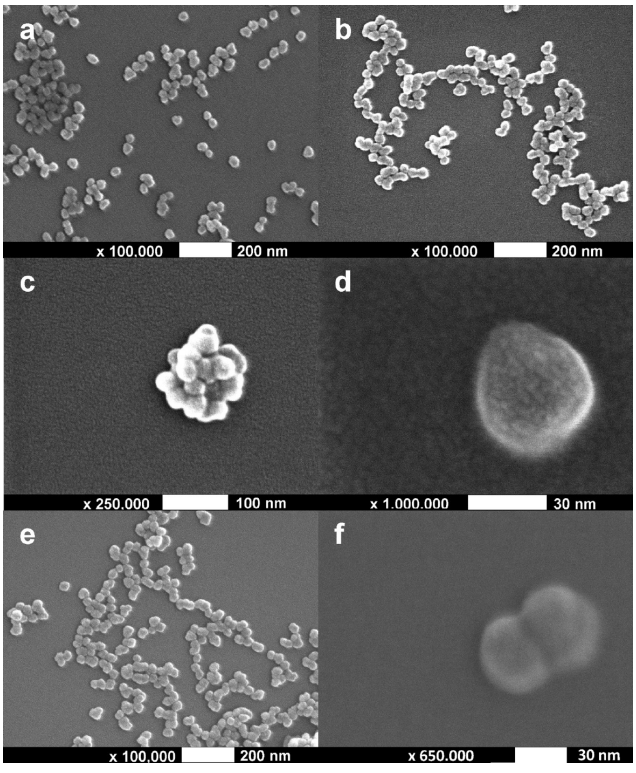

Figure 1. SEM images of SiO_2 nanoparticles on a silicon wafer: (a) nonfunctionalized SiO_2 nanoparticles; (b–d) TPC-functionalized nanoparticles at different magnifications; (e, f) photochemically dimerized TPC-NPs.

Figure 1 show a TPC-modified nanoparticle cluster as well as a single NP. Figure 1 e shows TPC-functionalized SiO_2 NPs that have been irradiated with light of 355 nm, which causes dimerization of the coumarins to dicoumarin. No changes in shape and no striking changes in size compared to the nonirradiated particles are observed. This is in accordance with the expectations, as dimerization of two coumarin groups both anchored adjacently on the same nanoparticle surface is much more probable than a dimerization between coumarin groups on two different nanoparticles. Figure 1 f shows such a nanoparticle dimer. After a single light exposure the statistic contribution of such nanoparticle clusters is not sufficient enough to change the average diameter of the nanoparticles significantly. The average diameter determined by DLS measurement remains about 45 nm with a polydispersity index similar to the previous one.

Figure 2a shows the height image of a mixture of nonfunctionalized SiO_2 nanoparticles and TPC-NPs on a freshly oxidized silicon wafer surface. Particle dispersions were mixed, and the substrate, freshly oxidized silicon, was immersed into the mixed dispersion. The particles seem to be more agglomerated than in the SEM pictures, which probably is due to the higher surface potential of the oxidized Si wafers compared to the untreated Si wafers used for SEM imaging. The size and shape of the nanoparticles fully correspond to the values determined by SEM and DLS. The change of approximately 5% in diameter related to the TPC functionalization is not enough to be reliably resolved in the AFM images.

Melin et al. reported in 2004 on charge injection experiments performed on silica nanoparticles and their analysis by EFM.[35] In 2009, Pacifica et al. described EFM imaging of different silica-coated metal nanoparticles.[36] We report for the first time on EFM as a tool to determine differences in surface potential between functionalized and nonfunctionalized silica nanoparticles on the single-nanoparticle level. Figure 2b shows the same sample as Figure 2a, but as an EFM image reflecting the surface potential. For this measurement Veeco's lift mode without any bias to tip or

dx.doi.org/10.1021/la200238y |*Langmuir* 2011, 27, 4149–4155

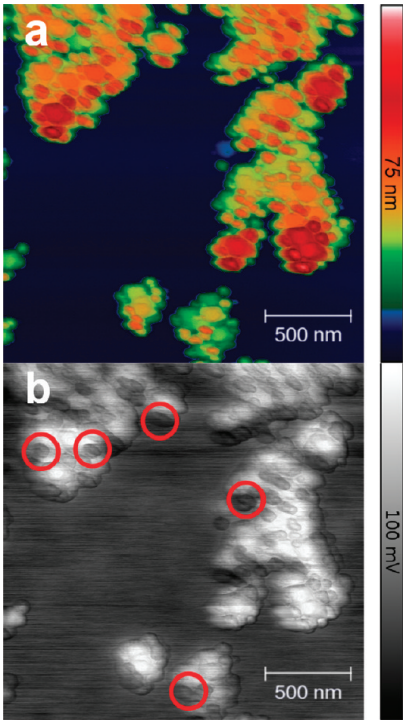

Figure 2. (a) AFM height profile of a mixture of nonfunctionalized and TPC-functionalized nanoparticles on a freshly oxidized silicon wafer surface. (b) Potential image (EFM) of (a).

surface was employed. Now two different species emerge, one charged like the surface (selected examples highlighted in red) corresponding to the nonfunctionalized SiO_2 nanoparticles and the other species with an approximately 75 mV different charge corresponding to the TPC-NPs. Areas with intermediate charge are due to stacking of the two different species. Due to the fact that the Si wafer is an insulator, no absolute values concerning the sign of the charge could be determined. However, it is clearly shown on the single-nanoparticle level that functionalization leads to a significant change in the surface potential of the nanoparticles. This could be confirmed by ζ potential measurements of bulk material. The ζ potential of the nonfunctionalized SiO_2 nanoparticles was -69.64 mV; the value for the TPC-functionalized nanoparticles was -49.64 mV.

To determine the degree of functionalization, TGA was performed. A weight loss of 11.8% between 100 and 850 °C was observed. Taking the molar mass of 7-(propanyloxy)coumarin groups, and assuming 4.5 silanol groups per square nanometer[37] on the nanoparticle surface, which corresponds to 22 620 silanol groups per 40 nm nanoparticle, the calculation results in a concentration of 0.57 μmol·mg^{-1} corresponding to 23 002 TPC molecules per nanoparticle. Assuming that statistically only 1.5 out of 3 ethoxy groups bind to the nanoparticle surface while the others react with other TPC molecules, the formation of a TPC "shell" (see Scheme 2) is likely to happen. This assumption is well supported by the correlating SEM and DLS measurements, which indicate the immobilization of a "bilayer" of TPC molecules. Assuming a load of 0.57 μmol·mg^{-1} TPC on the nanoparticle surface, a molar extinction coefficient for TPC-modified nanoparticles dispersed in acetonitrile of $\varepsilon_{320nm} = 8802 \pm 126$ L·mol^{-1}·cm^{-1} is derived. Compared to the molar extinction coefficient of TPC of $\varepsilon_{320nm} = 16\,047 \pm 142$ L·mol^{-1}·cm^{-1}, TPC bound to the silica nanoparticle seems to have only half the extinction coefficient. This finding is not surprising, as in a nanoparticle dispersion always half of the surface-bound molecules are in the "shadow" of the nanoparticle and thus not measurable for the spectrometer, which results in an apparent lower absorption and the derived decrease of the apparent molar extinction coefficient.

UV−Vis and Fluorescence Spectroscopic Studies of TPC-NPs. Coumarin and its derivatives show two characteristic absorption bands in their UV−vis spectra. Between 310 and 340 nm, an n $\rightarrow \pi^*$ like transition is observed related to the carbonyl function. At higher energies there is a $\pi \rightarrow \pi^*$ transition between 250 and 300 nm which corresponds to the conjugated π system. Irradiation with 355 nm light mainly results in a decrease of the absorption between 310 and 340 nm because the length of the conjugated π system is reduced. Figure 3a shows the absorption spectra as well as the fluorescence spectra of TPC-NPs in acetonitrile (0.1 mg·mL^{-1}). The disappearance of the absorption band at 320 nm is correlated with a decrease of the fluorescence emission band at 390 nm, indicating the photodimerization of coumarin groups. Irradiation with light of 280 nm wavelength triggers the photocleavage of dicoumarins and results in an increase of the absorption band at 320 nm and of the emission band at 390 nm due to the restoration of the extended conjugated π system (Figure 3b).

The efficiency of the photocleavage is quantified by the single-photon quantum yield ϕ_{cleave}:

$$\varphi_{cleave} = \frac{n_{dimer}}{n_{photon}} = \frac{n_{dimer}}{E_{abs}} \times \frac{E_{abs}}{n_{photon}} \quad (1)$$

n_{dimer} represents the number of cleaved coumarin dimers, n_{photon} the number of photons absorbed by coumarin dimers, and E_{abs} the absorbed energy. The quantum yield for the single-photon cleavage reaction is limited due to deactivating processes such as fluorescence or dissipation. Due to the low concentration of coumarin in the nanoparticle dispersion, not all irradiated energy is absorbed. The actual energy absorbed ($P_{abs,280nm}$) was calculated to be 2.01×10^{-4} W·cm^{-2} by

$$P_{abs,280nm} = P_{280nm}(1 - 10^{-A_{0,280nm}}) \quad (2)$$

with P_{280nm} being the energy irradiated and $A_{0,280nm}$ being the absorption at the beginning of the irradiation. The number of cleaved coumarin dimers per absorbed energy can be calculated by

$$\frac{n_{dimer}}{E_{abs}} = \frac{c_{dimer}}{E_{abs}} \times VN_A \quad (3)$$

with c_{dimer} being the concentration of cleaved dimers, V the volume of the probe (2 mL), and N_A the Avogadro constant. Plotting the concentration of cleaved dimers versus the actual energy absorbed results in a linear increase with $c_{dimer} \times E_{abs}^{-1}$ as the slope of the linear fitting of the data points (Figure 4b).

With (3) $n_{dimer} \times E_{abs}^{-1}$ is calculated to be 2.48×10^{17} J^{-1}·cm^2. The number of photons per energy unit results in 9.07×10^{17} J^{-1}·cm^2 according to

$$\frac{n_{photon}}{E_{abs}} = \frac{\lambda}{chA} \quad (4)$$

λ represents the wavelength, c the speed of light, h the Planck constant, and A the irradiated area. Using (1), the quantum yield of the dimer cleavage is determined to be 0.27, which is an

dx.doi.org/10.1021/la200238y |Langmuir 2011, 27, 4149–4155

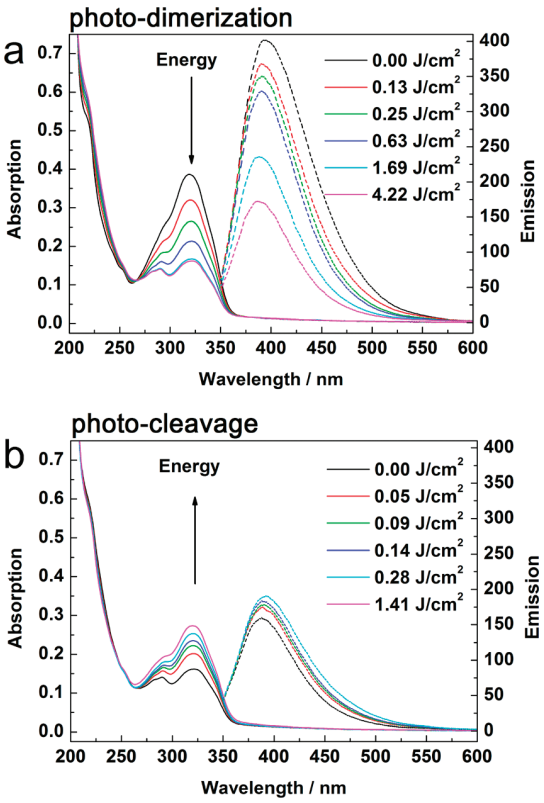

Figure 3. Absorption and fluorescence spectra of TPC-NPs dispersed in acetonitrile: (a) photodimerization after consecutive irradiations with 355 nm light with the total energies given; (b) photocleavage after consecutive light exposures to 280 nm with the total energies given.

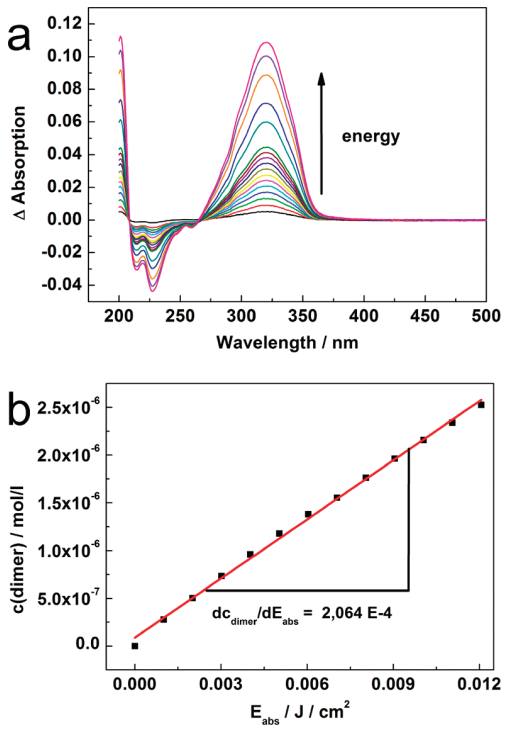

Figure 4. Photocleavage of coumarin dimers on SiO_2 nanoparticles: (a) difference spectra of dimerized TPC-NPs dispersed in acetonitrile during photocleavage with light of 280 nm; (b) determination of the quantum efficiency from the change in concentration versus the absorbed energy.

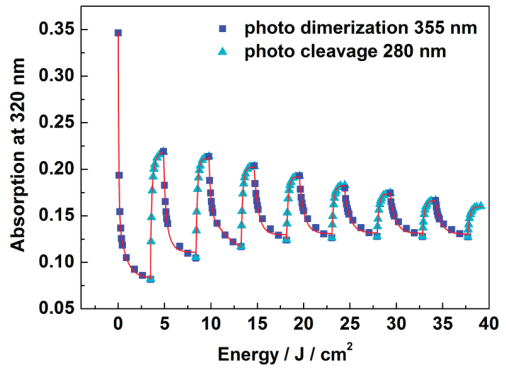

Figure 5. Reversibility of the photodimerization/photocleavage process given the absorption at 320 nm versus the irradiated energy at 355 nm (dimerization, squares) and 280 nm (cleavage, triangles). Solid red lines show second-order numerical fits.

average value compared to quantum yields of similar coumarin derivatives measured in solution.[38,39]

Figure 5 shows the absorption at 320 nm versus the irradiated energy at 355 and 280 nm over eight cycles of irradiation for a solution of 0.1 mg·mL^{-1} TPC-NPs in acetonitrile. Surprisingly, the photoreaction is not completely reversible as observed for SAMs with coumarin head groups on silicon oxide surfaces.[13] After dimerization of 81% of the coumarins attached to the particle, cleavage with 280 nm results only in a reoccurrence of 55% of the starting absorption of the coumarin groups. To ensure no loss of coumarin groups due to the high-energy laser pulses, dimerized TPC-NPs were centrifuged, dried, and analyzed by TGA, but neither an increase nor any decrease in weight loss was measured; we therefore conclude that all coumarin groups are still attached to the nanoparticles.

Comparing the wavelength dependency of the photocleavage reaction of TPC in solution and immobilized on the nanoparticle surface (see Figure 6), a quite different behavior emerges. Whereas TPC molecules dimerized in solution are completely cleaved under UV irradiation without a sign of any wavelength dependency, the TPC molecules on the nanoparticle surface show lower and differing equilibrium levels which are additionally dependent on the wavelength.

Figure 6a shows the photocleavage of TPC-NPs indicated by the absorption at 320 nm as a function of energy at different wavelengths. The initial absorption before dimerization was 0.48, resulting in 55% cleavage for 280 nm, 64% for 266 nm, and 72% for 254 nm. This wavelength dependency of photocleavage is observed neither in diluted solution (Figure 6b) nor on the flat surface of a SAM, where dimerization has an aligning effect on the absorbed coumarin groups, resulting in an even higher absorption at 320 nm after photocleavage. The explanation for this finding is that on the nanoparticles an equilibrium between photodimerization and photocleavage occurs. In solution the re-formation of dimers during photocleavage with UV light is very unlikely to happen due to the short lifetime of the exited state; i.e., the photodimerization is kinetically hindered. Attached to the nanoparticles, coumarins are in closer proximity, and therefore, re-formation of dimers occurs effectively and the wavelength-

dx.doi.org/10.1021/la200238y |*Langmuir* 2011, 27, 4149–4155

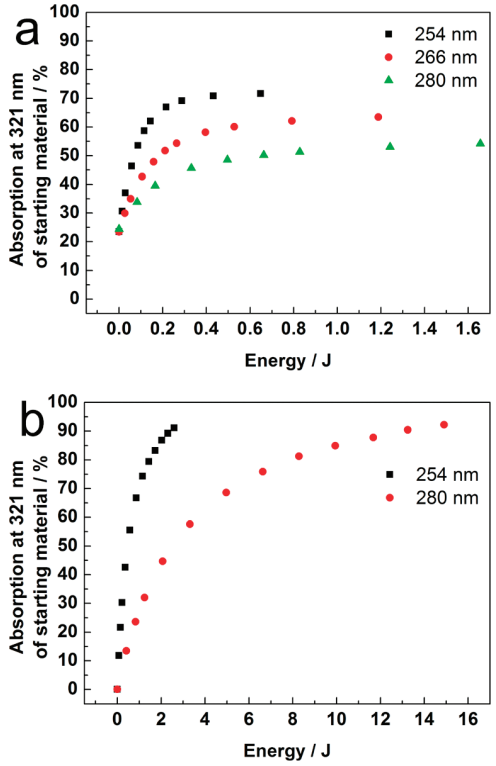

Figure 6. Wavelength dependency of photocleavage of (a) TPC-NPs and (b) a solution of an isomeric mixture of nonfunctionalized dicoumarin.

dependent equilibrium state is observed. The order of magnitude for the forward and the backward reaction rates become the same. Figure 7 shows the absorption change at 321 nm during photodimerzation and photocleavage versus the applied energy. Both sets of data points accurately match a second-order exponential fit. Although this is not readily expected for the photocleavage reaction, which is known as a classical first-order reaction, the higher quality of a second-order over a first-order fit is a clear indication for a change in reaction order. This finding is explained by the observed wavelength-dependent equilibrium caused by the superposition of photodimerization and photocleavage, because both reaction rates, that of the forward reaction and that of the backward reaction, are of the same order of magnitude.

Irradiation of the same sample with the same amount of energy over seven additional cycles (Figure 5) leads to a further loss of absorption after photocleavage as well as a higher remaining absorption after photodimerization, related to an apparent loss of monomeric coumarin groups. The explanation for the decreasing photocleavage efficiency is most likely due to photoinduced cluster formation (compare Figure 1c). Irradiation of these clusters with 280 nm is increasingly ineffective because the coumarin cross-links are shielded from irradiation when positioned between nanoparticles as described in the literature.[27] In the literature also the contribution of irreversible side reactions due to decarboxylation reactions was considered.[40] This explanation may not be excluded as a further contribution to the observed loss in reversibility, because the loss of CO_2 in such little amounts is beyond the detection limit of TGA measurements. The formation of cluster aggregates is substantiated by DLS measurements which derive an average size of 65 nm after eight cycles of photodimerization and photocleavage, about 20 nm or 50% more than after preparation.

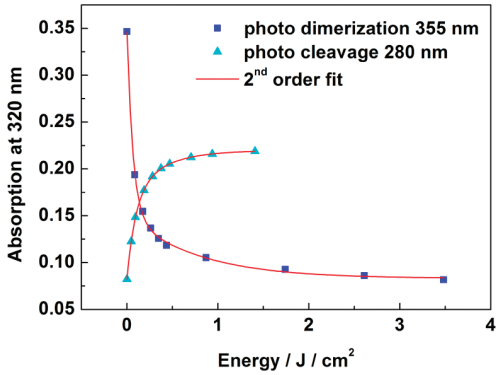

Figure 7. Numerical analysis of the photodimerization and the photocleavage. The data points are best fitted with two second-order fits.

SUMMARY AND CONCLUSION

TPC-NPs have been successfully synthesized, and their photoactivity can be characterized by absorption spectroscopy and fluorescence spectroscopy. The photochemical dimerization and the photochemical cleavage of the formed cyclobutane rings of molecules attached to the nanoparticle surface were demonstrated and followed for up to eight cycles. The quantum yield for UV-light-induced cycloreversion was determined to be 0.27, which is an average value compared to that in the literature. Surprisingly, a considerable wavelength dependency of the photocleavage was observed, and the photocleavage process itself seems to be incomplete. SEM, AFM, and EFM imaging were employed characterizing the morphology and size distribution as well as the surface potential of the coumarin-functionalized silica nanoparticles. It was found that, in comparison to coumarin groups attached to a flat substrate in a monolayer, the absorption change—indicating the amount of coumarin dimers in the sample—decreases from cycle to cycle. Two reasons for this observation were discovered. First, there is a significant overlapping of photocleavage and photodimerization with the UV wavelengths used. This causes a wavelength-dependent equilibrium between the monomeric and dimeric coumarins. This does not occur in solution in which the dimerization is kinetically hindered. The second reason identified is that the nanoparticles form photoinduced clusters by cross-linking between the nanoparticles. Within the nanoparticle clusters, the coumarin dimers are inaccessible for UV-light-induced photocleavage. An increase of the apparent average size of the nanoparticles in dynamic light scattering by about 50% supports our findings as well.

AUTHOR INFORMATION

Corresponding Author

*Phone: +49-6421-282-5775. Fax: +49-6421-282-5798. E-mail: hampp@staff.uni-marburg.de.

ACKNOWLEDGMENT

This work was supported by the German Federal Ministry of Education and Research in the framework of the ActIOL project (Grant FKZ 13N8978). We are grateful to Michael Hellwig and Hendrik Reinhardt for their help with the SEM measurements and Tobias Lepardt for his help with the DLS measurements.

REFERENCES

(1) Ciamician, G.; Silber, P. *Ber. Dtsch. Chem. Ges.* **1902**, *35*, 4128.
(2) Wolff, T.; Görner, H. *Phys. Chem. Chem. Phys.* **2004**, *6*, 368.
(3) Hammond, G. S.; Stout, C. A.; Lamola, A. A. *J. Am. Chem. Soc.* **1964**, *86*, 3103.
(4) D'Auria, M.; Racioppi, R. *J. Photochem. Photobiol., A* **2004**, *163*, 557.
(5) Yonezawa, N.; Kubo, M.; Saigo, K.; Hasegawa, M. *Bull. Chem. Soc. Jpn.* **1988**, *61*, 1005.
(6) Bhadbhade, M. M.; Murthy, G. S.; Venkatesan, K.; Ramamurthy, V. *Chem. Phys. Lett.* **1984**, *109*, 259.
(7) Moorthy, J. N.; Venkatesan, K.; Weiss, R. G. *J. Org. Chem.* **1992**, *57*, 3292.
(8) Stitchell, S. G.; Harris, K. D. M.; Aliev, A. E. *Struct. Chem.* **1994**, *5*, 327.
(9) Chen, Y.; Chou, C. F. *J. Polym. Sci., Part A: Polym. Chem.* **1995**, *33*, 2705.
(10) Chen, Y.; Hong, R.-T. *J. Polym. Sci., Part A: Polym. Chem.* **1997**, *35*, 2999.
(11) Li, W.; Lynch, V.; Thompson, H.; Fox, M. A. *J. Am. Chem. Soc.* **1997**, *119*, 7211.
(12) Fang, J.; Whitaker, C.; Weslowski, B.; Chen, M.-S.; Naciri, J.; Shashidhar, R. *J. Mater. Chem.* **2001**, *11*, 2992.
(13) Kehrloesser, D.; Traeger, J.; Kim, H.-C.; Hampp, N. *Langmuir* **2009**, *26*, 3878.
(14) Stöber, W.; Fink, A.; Bohn, E. *J. Colloid Interface Sci.* **1968**, *26*, 62.
(15) Dwivedi, N.; Arunagirinathan; Sharma, S.; Bellare, J. *Langmuir* **2009**, *26*, 357.
(16) Wang, H.; Yang, R.; Yang, L.; Tan, W. *ACS Nano* **2009**, *3*, 2451.
(17) Steinmetz, N. F.; Shah, S. N.; Barclay, E. J.; Rallapalli, G.; Lomonossoff, G. P.; Evans, D. J. *Small* **2009**, *5*, 813.
(18) Jacinto, M. J.; Landers, R.; Rossi, L. M. *Catal. Commun.* **2009**, *10*, 1971.
(19) Junming, S.; Xinhe, B. *Chem.—Eur. J.* **2008**, *14*, 7478.
(20) Zhang, Y.; Wang, A.; Zhang, T. *Chem. Commun.* **2010**, *46*, 862.
(21) Zhao, Y.; Qi, W.; Li, W.; Wu, L. *Langmuir* **2009**, *26*, 4437.
(22) Breiner, B.; Nitschke, J. R. *Nat. Chem.* **2010**, *2*, 6.
(23) Coti, K. K.; Belowich, M. E.; Liong, M.; Ambrogio, M. W.; Lau, Y. A.; Khatib, H. A.; Zink, J. I.; Khashab, N. M.; Stoddart, J. F. *Nanoscale* **2009**, *1*, 16.
(24) Slowing, I. I.; Vivero-Escoto, J. L.; Wu, C.-W.; Lin, V. S. Y. *Adv. Drug Delivery Rev.* **2008**, *60*, 1278.
(25) Liong, M.; Lu, J.; Kovochich, M.; Xia, T.; Ruehm, S. G.; Nel, A. E.; Tamanoi, F.; Zink, J. I. *ACS Nano* **2008**, *2*, 889.
(26) Imai, Y.; Naka, K.; Chujo, Y. *Polym. J. (Tokyo, Jpn.)* **1998**, *30*, 990.
(27) Graf, C.; Schärtl, W.; Hugenberg, N. *Adv. Mater. (Weinheim, Ger.)* **2000**, *12*, 1353.
(28) Mal, N. K.; Fujiwara, M.; Tanaka, Y. *Nature* **2003**, *421*, 350.
(29) Fujiwara, M.; Shiokawa, K.; Kawasaki, N.; Tanaka, Y. *Adv. Funct. Mater.* **2003**, *13*, 371.
(30) Zhao, L.; Loy, D. A.; Shea, K. J. *J. Am. Chem. Soc.* **2006**, *128*, 14250.
(31) Ha, S.-W.; Camalier, C. E.; Beck, G. R., Jr.; Lee, J.-K. *Chem. Commun.* **2009**, 2881.
(32) Clarke, D. J.; Robinson, R. S. *Tetrahedron* **2002**, *58*, 2831.
(33) van Blaaderen, A.; Vrij, A. *J. Colloid Interface Sci.* **1993**, *156*, 1.
(34) Gauglitz, G.; Hubig, S. *J. Photochem.* **1981**, *15*, 255.
(35) Melin, T.; Diesinger, H.; Barbet, S.; Deresmes, D.; Baron, T.; Stievenard, D. *Mater. Res. Soc. Symp. Proc.* **2004**, *832*, 179.
(36) Pacifico, J.; van Leeuwen, Y. M.; Spuch-Calvar, M.; Sánchez-Iglesias, A.; Rodríguez-Lorenzo, L.; Pérez-Juste, J.; Pastoria-Santos, I.; Liz-Marzán, L. M. *Nanotechnology* **2009**, *20*, 095708.
(37) Iler, R. K. *The Chemistry of Silica: Solubility, Polymerization, Colloid and Surface Properties, and Biochemistry*; Wiley: New York, 1979.
(38) Kim, H.-C.; Kreiling, S.; Greiner, A.; Hampp, N. *Chem. Phys. Lett.* **2003**, *372*, 899.
(39) Härtner, S.; Kim, H.-C.; Hampp, N. *J. Photochem. Photobiol., A* **2007**, *187*, 242.
(40) Wolff, T.; Görner, H. *J. Photochem. Photobiol., A* **2010**, *209*, 219.

Lebenslauf

Roelf-Peter Baumann

Ausbildung

12/08 – heute	Promotion in Biophysikalischer Chemie am Institut für Physikalische Chemie, Kernchemie und Makromolekulare Chemie der Philipps-Universität Marburg in der Arbeitsgruppe von Herrn Prof. Dr. N. Hampp mit dem Thema "On the Morphology and Dynamics of Purple Membranes at the Solid-Liquid Junction"
Oktober 2008	Chemie-Diplomhauptprüfung (Diplomarbeit)
01/08 – 10/08	Anfertigung der Diplomarbeit am Institut für Physikalische Chemie, Kernchemie und Makromolekulare Chemie der Philipps-Universität Marburg in der Arbeitsgruppe von Herrn Prof. Dr. N. Hampp mit dem Titel "Morphologie von Purpurmembranen an Grenzflächen"
Oktober 2007	Chemie-Diplomhauptprüfung (mündlich)
Oktober 2005	Chemie-Diplomvorprüfung
Oktober 2003	Beginn des Chemie-Studiums an der Philipps-Universität Marburg
Juli 2003	Allgemeine Hochschulreife
Juni 2003	International Baccalaureate Diploma
Mai 2003	Amerikanischer High School Abschluss